Evapotranspiration in water limited environments: up-scaling from the crown canopy to the eddy flux footprint.

Rwasoka Donald Tendayi

February, 2010

Evapotranspiration in water limited environments: Up-scaling from the crown canopy to the eddy flux footprint.

by

Rwasoka Donald Tendayi

Thesis submitted to the International Institute for Geo-information Science and Earth Observation in partial fulfilment of the requirements for the degree of Master of Science in Geo-information Science and Earth Observation, Specialisation: Integrated Watershed Management and Modelling – Surface Hydrology

Thesis Assessment Board

Dr. Ir. M. W. Lubczynski	(Chairman)	WRS Dept, UTwente - ITC
Dr. Ir. C.M.J. Jacobs	(External Examiner)	Wageningen University
Dr. Ir. C van der Tol	(1st Supervisor)	WRS Dept, UTwente – ITC
Prof Dr Ir Z (Bob). Su	(2nd Supervisor)	WRS Dept, UTwente – ITC
MSc Leonardo Reyes	(Advisor)	WRS Dept, UTwente – ITC

INTERNATIONAL INSTITUTE FOR GEO-INFORMATION SCIENCE AND EARTH OBSERVATION
ENSCHEDE, THE NETHERLANDS

Disclaimer

This document describes work undertaken as part of a programme of study at the International Institute for Geo-information Science and Earth Observation. All views and opinions expressed therein remain the sole responsibility of the author, and do not necessarily represent those of the institute.

Abstract

Evapotranspiration in Water Limited Environments (WLE) plays a central role in explaining ecohydrological dynamics and the mass-energy interactions between the land surface and the atmosphere. However, evapotranspiration is a lumped flux of evaporation and transpiration. In WLE, role of tree transpiration is a subject of current scientific and water resources management interest.

This work thus, implements for the first time, an integrated eddy covariance, sap flow, eddy flux footprint and remote-sensing based up-scaling approach to investigate tree transpiration dynamics in a WLE. The research focuses on the following thematic aspects (1) the role of transpiration fluxes in dry areas (2) the surface energy balance and (3) the application of eddy flux footprints in tree transpiration up-scaling and mapping using remote sensing.

Field measurements were done in the Sardon catchment close to Salamanca, Spain (DOY 249 -269, 2009), where the tree species *Quercus Ilex* and *Quercus Pyrenaica* are the dominant vegetation and thus are the focus of this study. Sap-flow was measured and up-scaled using species-specific biometric up-scaling functions combined with Quick-Bird imagery. Post-processing eddy covariance data was done to determine evapotranspiration from latent heat flux. Furthermore, 2-D eddy flux footprints were determined using 30-min energy flux data, and discretized over the land surface. Finally, the transpiration contribution to evapotranspiration was determined by up-scaling sap-flow from the tree canopies inside the eddy footprint.

The mean measured sap flow for *Quercus ilex* was ~2.8 litres per hour compared to ~0.4 litres per hour *Quercus pyrenaica*. Applying eddy covariance it was found that the average evapotranspiration was ~0.21 mm/day. The contribution of tree transpiration was assessed on the basis of two eddy flux footprints, which showed tree transpiration contributions of ~ 40 and ~13%. The differences in the percentages reveal the influence of species heterogeneity. The higher percentage was found from a footprint with a higher density of *Quercus ilex*. The trees enclosed in one of the studied footprints covered ~11% of the footprint surface area, and contributed ~40% of the evapotranspiration measured by eddy covariance, thereby highlighting the contribution of tree transpiration to the total evapotranspiration .

Soil heat flux was found to play a major role in energy flux partitioning as it reaches up to 40-50% of net radiation. A high energy balance closure of 86% was achieved without considering other energy storage terms such as biomass storage. An analysis of the lack of closure revealed the influence of friction velocity, thermal stratification and the proper determination of soil heat flux as key factors. The soil heat flux measurement that did not consider heat storage underestimated the soil heat flux by ~21%.

It is concluded that the integrated approach proposed and implemented in this research is a pragmatic and universally applicable approach for combining eddy covariance, sap flow and remote-sensing based tree transpiration up-scaling.

Acknowledgements

My humble thanks go to God Almighty for His loving kindness and grace for taking me thus far.

To Erasmus Mundus Lot 10, I thank you for granting me the scholarship to study at ITC, in the Netherlands.

Beyond words, I am highly indebted to my first supervisor, Dr Ir. C van der Tol for his guidance, advice and listening to my ideas on how to go about the research. The knowledge transfer on eddy covariance, I have no words to say thank you, “dank u well meneer”.

My deepest gratitude goes to my second supervisor, Prof. Dr. Ir. Z (Bob) Su for his critical ideas on the execution of research and his famous saying “... oh… this is very easy” even if… Having you as my supervisor made me to critically re-evaluate my work and thoughts.

To Leonardo Reyes, my advisor, “gracias amigos” for the guidance during fieldwork, your critical reviews of my work and sharing the knowledge you have on sap flow. The same goes also for Alain Frances for responding to my questions and the data

I would also like to thank the following ITC staff members: Remco Dost, Gabriel Parodi, Ben Maathuis, Wim Timmermans, Rogier van der Velde, Prof Wouter Verhoef and the ITC library staff. And to all my class mates, you are the best guys.

Special mention also goes to Cheng Hsieh and Matteo Detto for responding to my e-mails on eddy flux footprint implementation and its extension to 2-D and also to Bert Heusinkveld, Rick Synder, Jan Elbers and Alterra for the use of Alteddy and Anne Verhoef.

I would like to also thank the sap flow family, Benjamin and Andrea and the roommates at Campo-Charro in Spain during fieldwork

Last but not least, I would like to acknowledge the Zimbabwean community at ITC for their support, as well as Sava Chinamaringa, Rosy, Timothy Gotora and Brighton Kukasira and family. A big thank you goes to M. Mvura for the encouragement and support. Most importantly, to my family, a big thank you for the support and encouragement.

Table of contents

List of figures

List of tables

Abbreviations and Symbols

ABL	Atmospheric boundary layer
A_c	Crown canopy area
A_x	Xylem area
A_l	Xylem length (cored)
B_l	Bark length (cored)
BUF	Biometric up-scaling function
C	Scalar
C_s	Volumetric heat capacity
DBH	Diameter-at-breast height
E	Evaporation
ET	Evapotranspiration
EBR	Energy balance ratio.
G_0	Soil heat flux
H	Sensible heat
J_v	Sap flux density
λE	Latent heat
LW↓	Long wave incoming radiation
LW↑	Long wave outgoing radiation
Q_s	Sap flow
R_n	Net radiation
RH	Relative humidity
SW↓	Shortwave incoming radiation
SW↑	Shortwave outgoing radiation
T_a	Air temperature
TDP	Thermal dissipation probe
T_s	Sonic temperature
T_G	Ground temperature
U_*	Friction velocity
ρ_s	Scalar density,
u	Stream wise wind velocity
v	Lateral wind velocity
w	Vertical velocity
WLE	Water limited environment

1. INTRODUCTION

1.1. RESEARCH MOTIVATION

Evapotranspiration constitutes approximately 95% of the water budget in Water Limited Environments (WLE). Evapotranspiration is therefore a major component of the water budget (Newman et al., 2006; Wilcox et al., 2003). The precipitation to evapotranspiration ratio in WLE ranges from 0.03 to 0.75 and annual potential evapotranspiration is greater than annual precipitation (Abrahams and Parsons, 1994). Evapotranspiration thus plays a central role the water and energy interactions in the soil-vegetation-atmosphere continuum. It is therefore vital in explaining ecological and hydrological dynamics in WLE. Enhancing knowledge on evapotranspiration processes, dynamics and its components is thus important for scientific and water resource management purposes (Simmers, 2003).

With WLE constituting over 50% of the earth's land surface, research on evapotranspiration in WLE has both global and local scale relevance. From a hydrological perspective, the benefits of evapotranspiration research include: improved water resources planning and modelling especially in catchments that are groundwater dependent. In such catchments, phreatophyte vegetation species are believed to transpire groundwater resources in the saturated zone or capillary fringe (Lubczynski, 2009; Lubczynski and Gurwin, 2005; Obakeng, 2007). Recently, Paço et al. (2009) studied Mediterranean evergreen oaks and observed that tree transpiration constituted about 50 % of total evapotranspiration. Such evidence has raised questions about the quantitative hydrological role of tree transpiration in evapotranspiration processes and the water budgets of WLE (Baldocchi et al., 2004; Detto et al., 2006; Lubczynski, 2009). Newman et al. (2006) thus emphasized the need to partition evapotranspiration into evaporation and transpiration so as to gain more ecohydrological knowledge. They however acknowledge that there is lack of experimental and modelling research evidence to arrive at valid conclusions and generalizations. Oishi et al. (2008) further argues that understanding of such processes is limited by the failure to scale component flux measurements (of evaporation and transpiration separately) to the footprint. Hence, there is need to upscale from the tree crown canopy to the footprint level.

In response to the issues highlighted by Oishi et al. (2008) and Newman et al (2006) different approaches on transpiration quantification and its scaling have been developed. The approaches have resulted in an increased use of sap flow measurements (Chavarro-Rincon, 2009; Granier, 1985; Miller, 2009; Oishi et al., 2008; Ontiveros Enriquez, 2009; Rana and Katerji, 2000; Williams et al., 2004). The work of Kimani (2005), Kimani et al (2007) and Chavarro-Rincon (2009) outline a remote sensing based approach to up-scale sap flux density measurements to stand transpiration. The approach uses field measured up-scaling scalars that are then related to features that can be retrieved from a remote sensing image, i.e. tree canopies. Such an approach makes the estimation of tree transpiration at different spatial and temporal scales possible. Moreover, this technique is more appropriate than the

alternative of using Leaf Area Index (Oishi et al., 2008), because in WLE the dynamics of Leaf Area Index change are not well correlated with the transpiration flux dynamics (Lubczynski, 2009).

Although the remote sensing based up-scaling approach is highly relevant for WLE, the up-scaled transpiration flux has not been combined and compared with eddy covariance measurements. A key challenge is the lack of a clear methodological approach that takes the spatial and temporal issues of both approaches into account. Remote sensing based up-scaling produces a spatially distributed transpiration flux and yet eddy covariance, albeit being measured at a single point, measures a spatially averaged over a fetch area. Fetch to height ratios of 1:100 have thus been established as a rule of thumb for estimating the fetch area. However, the fetch to height ratio is not universally attainable. Thus the definition of the fetch area in coordinate space based on fetch to height ratios remains fuzzy. This poses a fundamental challenge of how to compare the up-scaled transpiration and eddy covariance evapotranspiration. The need to compare up-scaled transpiration with eddy covariance evapotranspiration is founded on the realisation that eddy covariance is the most direct evapotranspiration quantification method available (Brutsaert, 2005; Gash and Shuttleworth, 2007; Rana and Katerji, 2000) and probably the most accurate method.

Most WLE environments, including the Mediterranean area where this study was carried out, are heterogeneous with sparse vegetation (Baldocchi et al., 2004; Detto et al., 2006; Santana, 2008). In these areas there are concerns about the representativeness of eddy covariance flux measurements and consequently the interpretation of the results (Matson and Goldstein, 2000; Schmid, 1997). These concerns arise from some of the requirements for accurate application of the eddy covariance method. Some of these requirements include: stationarity, zero mean vertical wind speed, fully developed turbulence, and the lack of advection (Foken, 2008b; Garratt, 1994; Göckede et al., 2004; Stull, 1998). Foken and Wichura (1996), Göckede et al (2004) and Mauder and Foken (2004) presented some tools to assess whether these requirements are met. The tools include the stationarity and the integral turbulence characteristics tests. Göckede et al.,(2004) successfully combined these tools with footprint analysis for assessing complex FLUXNET sites. These tools and the success of Göckede et al. (2004) supports the application of eddy covariance over heterogeneous areas.

Furthermore, a better interpretation of the measured fluxes over different land surfaces can be achieved by applying a recent scientific development of eddy flux footprint determination (Vesala et al., 2008). An eddy flux footprint in simple terms is the source area of the flux measured by eddy covariance instruments. A few studies have used eddy flux footprints in practical experimental research on evapotranspiration (Detto et al., 2006; Oishi et al., 2008). The determination of an eddy flux footprint takes on two main approaches notably, that is analytical solutions (Hsieh et al., 2000; Kormann and Meixner, 2001; Schmid, 1994; Schuepp et al., 1990) and lagrangian stochastic dispersion solutions (Kljun et al., 2002; Rannik et al., 2003; Raupach, 1989; Thomson, 1987). Analytical solutions are more pragmatic and have broader applicability (Marcolla and Cescatti, 2005) hence an analytical solution is applied in this study.

The analysis of evapotranspiration fluxes using eddy covariance has to be complemented by an energy balance analysis. In line with the principle of energy conservation, the balance of measured radiation, conductive and turbulent heat fluxes provides understanding about the quality of flux measurements

(Foken, 2008a). Unfortunately, full energy balance closure is rarely achieved. Thus closure of the energy balance is widely acknowledged as an outstanding problem in energy balance measurements (Foken, 2008a). The lack of closure has been anticipated to be between 10 – 30% (Foken, 2008a; Heusinkveld et al., 2004; Twine et al., 2000). Published energy balance closure percentages are as low as 53% (Herbst et al., 2002) or as high as 94% (Baldocchi et al., 2004) and 97% (Mauder et al., 2007). Whilst different researchers have worked on this problem there has been little attention on the role of soil heat flux. In most sites, soil heat flux constitutes a low percentage of the energy balance, e.g. 10% over low vegetation. In drier areas soil heat flux should be much higher. The study by Heusinkveld et al. (2004) showed the central role of soil heat flux in the partitioning of fluxes in semi-arid and/or water limited environments and its impacts on energy balance closure.

This research is thus motivated to explore, for the first time, the combination of eddy flux footprints and remote sensing up-scaled transpiration. The integration of eddy flux footprints makes a comparison of the total evapotranspiration (from eddy covariance) and up-scaled transpiration possible. Thus the eddy flux footprint is proposed as the spatial domain for up-scaling sap flow. This allows for the understanding of water exchange processes at comparable spatial and temporal scales (Williams et al., 2004). Consequently the role of tree transpiration in WLE is highlighted.

1.2. GENERAL OBJECTIVE

The general objective of this research is to study evapotranspiration and energy balance dynamics in a water limited environment by quantifying eddy covariance evapotranspiration fluxes and then compare them with remote sensing up-scaled sap flow at the footprint level.

1.3. SPECIFIC OBJECTIVES

The specific objectives of this research are:

1. To quantify the evapotranspiration using eddy covariance and surface energy balance fluxes;
2. To up-scale sap flow using biometric up-scaling functions and remote sensing;
3. To determine the eddy flux footprints and integrate them with remote sensing imagery;
4. To compare the evaporative fluxes and discuss the significance of the research results with regards to understanding evapotranspiration processes in Water Limited Environments.

1.4. RESEARCH QUESTIONS

The research questions are divided into three sub-themes as follows:

Surface Energy Balance (Objective 1)

What are the diurnal dynamics of surface energy balance fluxes?

What is the quality of the turbulent heat fluxes?

What is the degree of energy balance closure and what could have caused the lack of complete closure?

Evapotranspiration Fluxes (Objective 1 and 2)

What are the evapotranspiration and transpiration flux quantities?

Integration of data and comparison (Objective 3 and 4)

How does the transpiration and evapotranspiration fluxes compare in the footprint?

What is the significance of the research results with regards to understanding evapotranspiration processes and the role of tree transpiration in WLE?

1.5. SCIENTIFIC PLACEMENT OF THIS RESEARCH

At the time of the research, there exists no known published research work that attempted to use the remote sensing tree transpiration up-scaling approach combined with eddy covariance at footprint level.

With regards to sap-flow up-scaling using biometric up-scaling functions and remote sensing, this research builds on and extends further the work of Kimani et al.,(2006), Kimani et al.,(2007), Ontiveros Enriquez (2009), Chavarro-Rincon, (2009) and Lubczynski (2009). In comparison to the study by Ontiveros Enriquez (2009) carried out in the same area, this study goes beyond sap flow up-scaling by introducing eddy covariance, eddy flux footprint determination and the comparison of evapotranspiration and up-scaled transpiration.

Closer to the concept behind this research is the work by Williams et al. (2004), who applied flux footprints using the solution by Horst and Weil (1992; 1994) in combination with sap flow, eddy covariance and isotopic data. Their work provides insightful results on the dynamics of soil evaporation and tree transpiration. However, their work differs from this study in that they do not apply remote-sensing based up-scaling, but rather demonstrate the 'Keeling plot' approach to up-scaling.

Oishi et al. (2008) also carried out a footprint based approach for up-scaling. Granier Thermal Dissipation Probe (TDP) sap flow data was scaled to the footprint level based on allometric relations they derived. The scaling to the footprint level was accomplished by using a species-specific Leaf Area Index (LAI) and plot data. However, compared to this research, differences arise from fact that retrieved crown canopies are used and that this study is done over a naturally heterogeneous environment, whilst the work by Oishi et al. (2008) is over a forest.

Schaeffer et al. (2000) apply a sap flow up-scaling approach based on allometric relations of sapwood area, projected canopy area and the diameter at breast height. Their up-scaling is partly based on established power relations between sapwood area and the diameter-at-breast-height (DBH). Their work is done over heterogeneous patches of cotton and willow forest, and aerial photographs are used to assess the projected canopy area. They however did not use eddy covariance measurements for comparison.

Paço et al (2009) attempted to also respond to the research gap that this thesis is geared to address by studying evapotranspiration from a *Quercus ilex* (holm oak) - herbaceous and tree species. Sap flow measurements and eddy covariance are used to arrive at conclusions that transpiration from trees was 50%. Paço et al.(2009) refer to Pereira et al. (2007) for their methodology, but still the use matching of spatial scales is not clear.

Baldocchi et al. (2004) applied a Lagrangian footprint model and in their work they combined it with IKONOS imagery and eddy covariance. However, their work is not directly focussed on sap flow or its up-scaling, though a footprint model is used to compute fetch requirements.

Foken (Foken, 2008a) presented a comprehensive assessment of the energy balance closure problem. Previous studies and causes of the lack of closure are discussed in detail. Baldocchi et al.(2004) also report a high energy balance closure of 94%. In their work they use 24-hour averages. In this way, uncertainties in soil heat flux (which is prone to errors) are eliminated, as the 24-hour average of soil heat flux is relatively small.

Previous studies in Sardon catchment have focused on the spatio-temporal aspects of tree transpiration (Ontiveros Enríquez; 2009), numerical groundwater flow and solute transport modelling (Ruwan Rajapakse; 2009) and groundwater modelling using GIS and remote sensing (Shakya; 2001).

2. STUDY AREA

An extensive description of the study area can be found in the work of Lubczynski and Gurwin (2005), Ontiveros Enriquez (2009), and Ruwan Rajapakse (2009). Here a general description is provided**.**

2.1. LOCATION: SARDON

Administratively, Sardon is located in Salamanca province, which occupies the central part of Spain. It is between $41^0$09', $41^0$02 N and 6^0 06', 6^0 14'. The Sardon area is part of the Rio Tomes catchment whose major tributary is Sardon River. Sardon river catchment covers an area of approximately 80 km^2. This research focuses on the area around Trabadillo, that is located approximately 41^0 07' 30.99" N and 6^0 09' 01.39"W. This is shown as TRB in Figure 2-1:

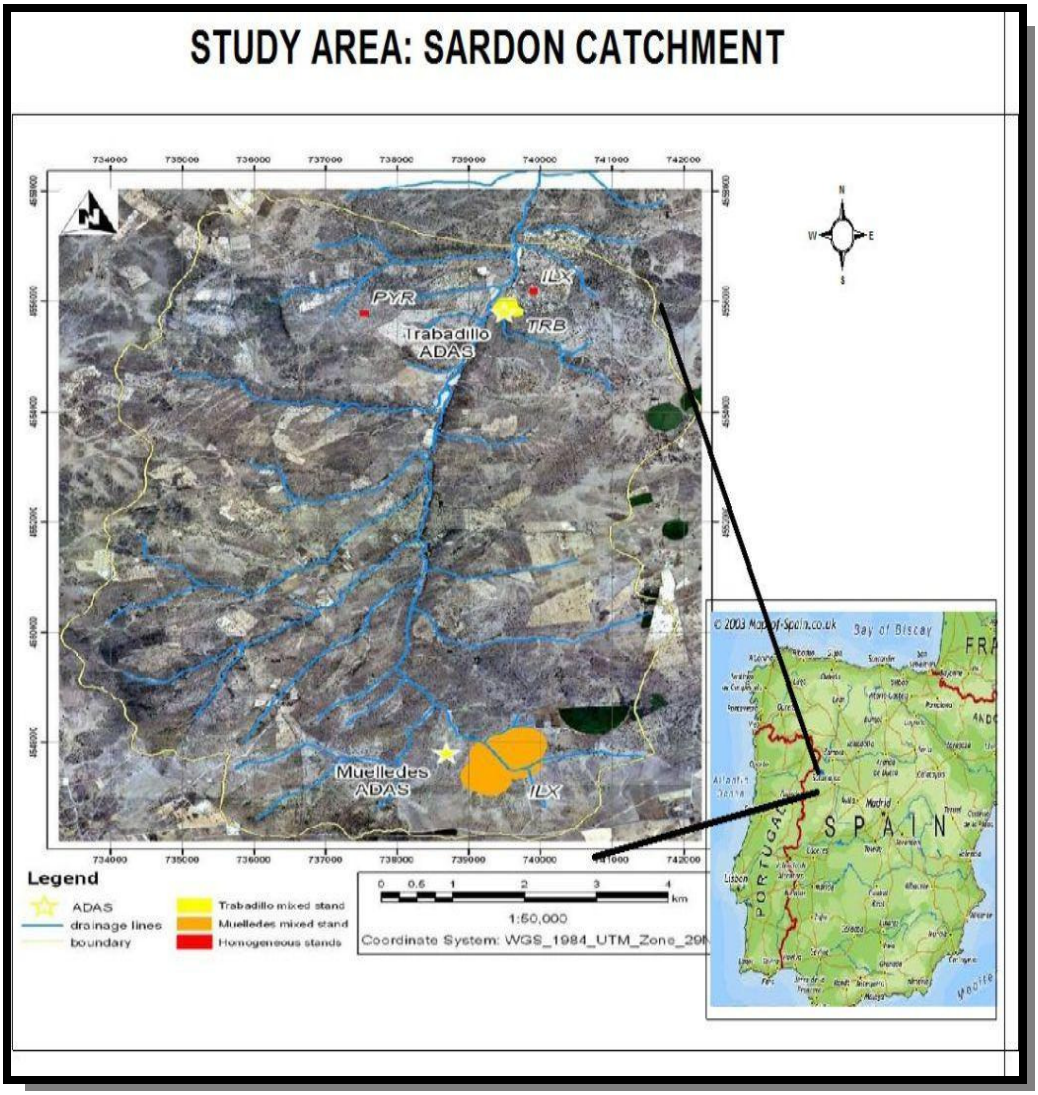

Figure 2-1: Map of the study area - after (Ontiveros Enriquez, 2009)

2.2. CLIMATE

A 23 year rainfall analysis showed that the mean rainfall is approximately 500 mm yr^{-1}. Average potential evapotranspiration of the area is ~5 mm/day during the driest and warmest months (Lubczynski and Gurwin, 2005). July and August are the warmest and the driest months, with an average temperature of ~22 °C. Rainfall patterns are variable with the wetter months being November and December with an average total rainfall greater than 100 mm/month. Sardon is a typical semi-arid and/or water limited environment (WLE).

2.3. HYDROLOGY AND HYDROGEOLOGY

The flow regimes in Sardon catchment are marked by periods of dry river channels from June to October. The drainage network is dense and is influenced by Sardon river that flows into the perennial Tormes River. The flow pattern is also influenced by a local fault zone. The hydrological response of the catchment to rainfall events is marked by rapid and direct run-off. In instances of heavy rainfall, temporary flooding occurs in land surface depressions as well as temporary saturation in the zone of non-permanent saturation. This is due to the presence of a highly permeable but thin upper unconsolidated layer that has a low water retention capacity (Lubczynski and Gurwin, 2005; Ruwan Rajapakse, 2009).

Groundwater flow is of moderate velocity and less susceptible to seasonal influences (Lubczynski and Gurwin, 2005). Improvements to a Sardon groundwater model initially developed by Lubczynski and Gurwin (2005) and continued by Ruwan Rajapakse (2009) estimated recharge at 0.38 mm/d and groundwater outflow at 0.24 mm/d. Groundwater in Sardon catchment flows towards the central and regional drainage line influenced by the Sardon fault. The Sardon fault transmits water towards the northern outlet.

2.4. TREE SPECIES

The *Quercus* (oak) tree genus is the dominant in the study area. *Quercus* is the name used to defined oaks. Oaks take the form of either a tree or a shrub. In Sardon catchment, two *Quercus* tree species can be found. The two available species are the evergreen *Quercus ilex (Q. ilex)* and the deciduous *Quercus pyrenaica (Q. pyrenaica)*, locally named “encina” and “roble” respectively. The two tree species are sparsely distributed in catchment and the pictures of the leaf structures are in appendix 1

2.4.1. Quercus ilex

The evergreen *Quercus ilex (Q. ilex)* is native to the Mediterranean area. The tree generally grows to heights of about 20 – 27 metres although in the study area average tree heights are about 6 m. Its leaves exhibit an evergreen leathery form. Old leaves fall off, 1 -2 years after new ones have emerged. The *Q. ilex* is considered a water efficient plant because it has small leaves that have an efficient internal structure that restricts evaporative losses. They exhibit abilities to harvest atmospheric, shallow and deep subsurface moisture. *Q.ilex* have been observed in times of acute water stress or shortage to be able to lift up groundwater through their roots, release it into the upper soil layer due to a water potential gradient. The water released in upper soil layers in then reabsorbed by shallow roots and

transpired. This mechanism is termed hydraulic lift (David et al., 2007). These groundwater uptake abilities allow for the classification of *Q.ilex* in Mediterranean weather as being a phreatophyte.

2.4.2. Quercus Pyrenaica

The *Quercus pyrenaica (Q. pyrenaica)* is also native to the Iberian Peninsula. *Q. pyrenaica* trees can grow up to a height of 25 m and the leaves are grey-green with an average length range of 8 -20 cm. The *Q. pyrenaica* grows in clusters. By spring time the tree does not completely shed off its leaves. Some old leaves will still be on the tree when new leaves grow. The *Q. pyrenaica* leaves are distinctively different from *Q. ilex* leaves in that they are irregular, lobed and a have short fur.

Aranda et al., (2004) asserts that *Q. pyrenaica* has an osmotic adjustment capacity in response to drought or extreme water stress. This is a typical strategy of Mediterranean and Sub-Mediterranean oaks in the face of drought and water stress. Also the *Quercus pyrenaica* tree has a good rooting system. It has a deep tap root which develops several horizontal roots, mainly in the shallow subsurface. This allows for the growth and development of peripheral vegetation around the tree. Common vegetative species that surround the *Q. pyrenaica* is the Cytisus scoparius. However, it has not been proven that *Q. pyrenaica* can tap water from groundwater (phreatophyte behaviour).

3. THEORETICAL BACKGROUND

3.1. EVAPOTRANSPIRATION

Evapotranspiration is a physical process through which water or moisture is transferred from the land surface to the atmosphere. This transfer of water into the atmosphere plays a critical role in the hydrological cycle. By definition evapotranspiration is a lumped flux (volume per unit time) consisting of two components, evaporation and transpiration. Transpiration represents the loss of water from plants species. Evaporation occurs on surfaces such as: open water, land surface and interception evaporation. The components of evapotranspiration can be expressed as;

$$ET = E_{bs} + E_{ow} + E_i + T \qquad \text{(Equation 1)}$$

Where ET is the total evapotranspiration, E_{bs} is the bare soil evaporation, E_{ow} is the evaporation from open water surfaces, E_i is interception evaporation and T is transpiration. An improvement of this simple conceptual framework is possible. Lubczynski, (2009) for example, provides a conceptual framework that includes sub-surface or unsaturated zone evapotranspiration (ET_u) and groundwater evapotranspiration(ET_g). Groundwater evapotranspiration is defined as loss from the saturated zone and the capillary fringe. The conceptual definition, which is also valid for WLE (Lubczynski, 2009; Lubczynski and Gurwin, 2005) is thus expressed as:

$$ET_{ss} = E_u + T_u + E_g + T_g \qquad \text{(Equation 2)}$$

Where ET_{ss} is the subsurface evapotranspiration, E is evaporation and T is transpiration. Subscripts $_u$ refers to the unsaturated zone and $_g$ to groundwater.

The evapotranspiration rate that occurs when there are no limiting factors is referred to as potential evapotranspiration. Actual evapotranspiration refers to the actual loss flux that occurs. Evapotranspiration is influenced by the following factors;

- Solar radiation
- Temperature
- Vapour pressure deficit
- Humidity
- Plant physiological features (for transpiration).

The need to understand evapotranspiration is demonstrated by the large number of methods that have been developed to estimate it. These methods can be classified as direct and indirect methods of measuring, and modelling. Gash and Shuttleworth (2007) in a review compilation on benchmark papers on evapotranspiration review two benchmark approaches that are applied in this work. These are the eddy covariance approach (Swinbank, 1951) and the Granier sap flow method (1985; 1987). Eddy covariance is the one of the most direct approaches available for measuring evapotranspiration (Brutsaert, 2005) though its technically demanding. The Granier Thermal Dissipation Probe (TDP)

offers the opportunity to quantify the plant transpiration flux. It is suitable for transpiration measurements, up-scaling and mapping.

3.2. EDDY COVARIANCE

In the lower part of the atmosphere, defined as the atmospheric boundary layer (ABL), the dominant transport mechanism is turbulence. Some of the characteristics of turbulence are:

1 Three dimensional and rotationality: that is, the velocity field is three-dimensional and highly variable in space and time.
2 Dissipative: though turbulent motion is supported by a constant supply of energy, its kinematic energy is also constantly being transformed into internal energy or heat (dissipation).
3 Diffusivity: i.e. turbulent motion has the ability to mix properties. This is vital for the formulation of the eddy covariance theory and evapotranspiration in particular. Diffusivity allows turbulence to efficiently diffuse momentum, heat and mass (for example: carbon dioxide and water vapour).
4 Irregular or random. (Arya, 1988; Garratt, 1994; Holton, 2004)

Turbulence can be classified according to its driving source. Thermal turbulence is a result of the heating of air which forces thermal 'bubbles' to be formed and rise up. Mechanical turbulence results from wind shear that stems from frictional drag. Frictional drag occurs when ground air flow is impeded by a variety of obstacles. Inertial turbulence occurs at the edges of larger eddies that will be losing their energy which the smaller eddies gain. Turbulence is thus inherently chaotic and hence its treatment is largely statistical. To aid conceptual understanding, Figure 3-1 shows an example two eddies with vertical velocity, w' and potential temperature, θ.

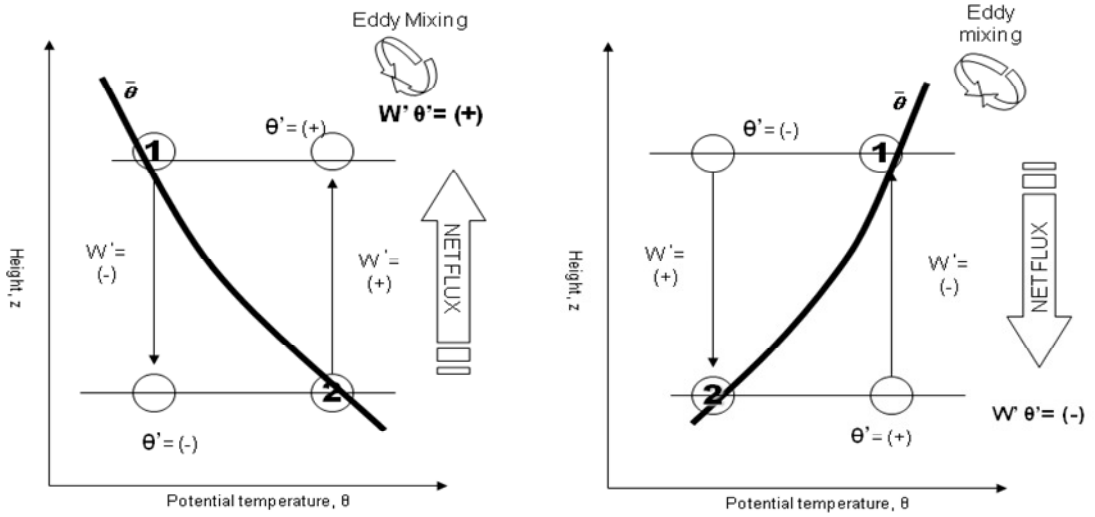

Figure 3-1: Simplified eddy schematic adapted from Stull (1998).

The graph on the left of Figure 3-1 shows a typical hot summer afternoon characterised by rising warm air, w' (2) and convective cooling of sinking particles (1).

The warmer air has a positive *w*' (upward direction) and the cooler air has a negative *w*' (downward direction). The instantaneous product w'θ' is thus positive (warm air up, θ'= + and vertical velocity, w'= + thus w'θ' up = + and cool air down, θ'= - and vertical velocity, w'= - thus w'θ' down = +). The net flux is thus positive in that instance. This is the principle of eddy covariance measurements. Even though the net transport of air mass is zero ($\overline{w} = 0$), the net transport of flux, $\overline{w'\theta'} \neq 0$ (Stull, 1998; Stull, 2000).

The graph on the right of Figure 3-1, shows a typical atmospherically stable time e.g. at night whereby the parcel of air moving up ends cooler than its surrounding hence w' is positive but θ' is negative thus the product w'θ' is thus negative. The instantaneous product w'θ' of the parcel that is moving down will also be negative. In terms of the flux $\overline{w'\theta'}$ this implies downward heat transport (Stull, 1998).

The determination of turbulent and mean fluxes depends on two fundamental concepts. The first concept is Taylor's hypothesis of "frozen turbulence". Being turbulent, the distribution of eddies is irregular. Measuring the size and distribution of eddies would thus be almost impossible as there would be need for a lot of instruments per unit area. Taylor thus postulated that the rate of change of eddies is small in comparison to the mean flow velocity. Therefore turbulence can be considered "frozen" as it passes a sensor over short timescales. A single high frequency instrument can thus be used to get a spatially averaged flux (Foken, 2008b; Stull, 1998).

Secondly, the treatment of turbulence makes use of the Reynolds decomposition. The underlying idea of Reynolds decomposition is that any field variable can be decomposed into its mean (indicated by overbars) and the fluctuating (turbulent) component (indicated by prime) for example a scalar such as water vapour, C is decomposed as:

$$C = \overline{C} + C' \qquad \text{(Equation 3)}$$

By the definition of turbulence, the mean components vanish as well as the product of a fluctuating component and the mean also vanishes when time averaged (Holton, 2004).

$$\overline{w'\overline{\theta}} = \overline{w'}\overline{\theta} = 0 \qquad \text{(Equation 4)}$$

The real-world physical system is however governed by a set of rather complex transport equations. Solving them in the ABL involves a number of assumptions that are critical to the development of eddy covariance theory and the interpretation of the results. These are highlighted in section 3.2.1.

3.2.1. Transport Equations in a Turbulent Atmosphere

To attain closure of the equations, seven equations can be derived. Only two of the equations are shown here, in order to demonstrate the assumptions needed to apply Reynolds decomposition. The equations that will be shown are the: scalar and mass conservation equations. The latter eventually becomes the continuity equation. For a complete derivation of all the equations one is referred to the work of; Stull (1998), Lee (1998) Finnigan (1995) and (Paw U et al., 2000).

The mass conservation equation in a compressible flow field can be derived as:

$$\frac{D\rho}{Dt} + \rho\left(\frac{\partial u}{\partial x} + \frac{\partial v}{\partial y} + \frac{\partial w}{\partial z}\right) = 0 \quad \text{(Equation 5)}$$

which can also be written as:

$$\frac{\partial \rho}{\partial t} + \nabla \cdot (\rho \mathbf{v}) = 0 \quad \text{(Equation 6)}$$

The term $\nabla \cdot \mathbf{v}$ is known as the divergence of the velocity vector. This latter form describes the conservation of mass at any point (x, y, z) when $(\rho \mathbf{v})$ is allowed the represent a specific mass flux. Mass flux is the flux of mass per unit cross sectional area and per unit of time (Brutsaert, 2005). In a turbulent boundary layer, it is then assumed that the density of an air parcel does not change and hence the total derivative on the left of (Equation 5) and (Equation 6) is ignored. This assumption is formally known as the assumption that air in the atmospheric boundary layer is incompressible. Hence the mass conservation equation transforms to the continuity equation as below;

$$\nabla \cdot \mathbf{v} = 0 \quad \text{(Equation 7)}$$

Or

$$\frac{\partial u}{\partial x} + \frac{\partial v}{\partial y} + \frac{\partial w}{\partial z} = 0 \quad \text{(Equation 8)}$$

This form allows for the simplification of micrometeorological equations

A scalar is a non-vectorial field variable (like water vapour). When it is passive, it means that the scalar has no independent inertia, thus its transportation is dependant on turbulence, i.e. turbulent fluxes. The measurement of a scalar flux at some point above the ground demands that there be a constant flux layer (Moncrieff et al., 2000). The assumptions and conditions required to determine a scalar flux are shown by examining the conservation equation for a scalar presented below:

$$\frac{\partial \rho_s}{\partial t} + u\frac{\partial \rho_s}{\partial x} + v\frac{\partial \rho_s}{\partial y} + w\frac{\partial \rho_s}{\partial x} = S + D \quad \text{(Equation 9)}$$

Where ρ_s is the scalar density [kg m^{-3}], u, v and w are the wind velocity components in the direction of the mean wind (x), lateral (y) and normal to the surface (z) [m s^{-1}] respectively. S is the source or sink term and D is molecular diffusion (Aubinet et al., 2000).

Applying Reynolds decomposition, averaging, integrating along z and assuming no horizontal flux divergence, the scalar conservation equation translates to:

$$\int_0^{h_m} S\,dz = \overline{w'\rho_s} + \int_0^{h_m} \frac{\partial \overline{\rho_s}}{\partial t} dz + \int_0^{h_m} \overline{u}\frac{\partial \overline{\rho_s}}{\partial t} dz + \int_0^{h_m} \overline{w}\frac{\partial \overline{\rho_s}}{\partial t} dz \quad \text{(Equation 10)}$$

I *II* *III* *IV* *V*

When the scalar is water vapour then Term I, represents evapotranspiration. Term II is equivalent to the eddy flux at height, h_m. Under the ideal conditions of stationarity ($\partial \rho_s / \partial t = 0$) and horizontal homogeneity terms III, IV and V vanish. The term I and II represents the kinematic eddy fluxes + (Aubinet et al., 2000; Moncrieff et al., 2000).

However when these conditions are not met, term III which represents storage of the scalar below the imaginary measuring plane. For water vapour this term is small at night. Term IV is horizontal advection. Term V is vertical advection. Term IV is considerable when scalar gradients exist especially due heterogeneous terrain (Aubinet et al., 2000)

3.2.2. Kinematic Eddy Flux Equations.

In view of the assumptions and requirements, eddy fluxes are determined by the following statistical covariance equations. The general covariance framework is:

$$\overline{w'x'} = \frac{1}{N-1}\sum_{k=0}^{N-1}\left[\left(w_k - \overline{w_k}\right)\left(x_k - \overline{x_k}\right)\right] \quad \text{(Equation 11)}$$

Where w is the vertical velocity and x a scalar or any of the two horizontal wind components (Foken, 2008b). Sensible heat flux (H) in W m^{-2} is determined by:

$$H = \rho_a \cdot C_p \cdot \overline{w'T'} \quad \text{(Equation 12)}$$

Where ρ_a density of air, w' is the turbulent vertical wind velocity, T' is the deviation in temperature and C_p being the specific heat capacity. The specific heat capacity translates the product into energy units.

Latent Heat flux is generically determined by the following formula:

$$LE = \lambda \cdot \frac{M_a / M_w}{P} \cdot \rho_a \cdot \overline{w'e'} \quad \text{(Equation 13)}$$

Consequently, evapotranspiration is thus computed as the covariance of vertical wind speed (w') and humidity (q'). The formula for directly computing evapotranspiration outlined by Brutsaert (2005) is:

$$\mathrm{E} = \rho_a \cdot \overline{\mathrm{w'q'}} \quad \text{(Equation 14)}$$

Where ρ_a is density of air (Kg m^2), w' is vertical wind speed m s^{-1}, q is humidity and E is evaporation (mm s^{-1})

3.3. EDDY COVARIANCE CORRECETIONS

3.3.1. Schotanus Correction

Temperature measurements from a sonic anemometer are based on the time it takes for sound pulses to go from one transducer to another over a known path length and angle geometry. This is termed sonic temperature. However, the time taken is influenced by atmospheric moisture and density effects. These effects need to be corrected. Schotanus et al (1983) significantly brought understanding and a solution to this problem. Schotanus et al (1983) provided formulations to address this issue but they are not presented here because the work of Liu et al (2001) enhances the equations to take into account that nowadays the transducers of anemometers have 3 orthogonal elements e.g. CSAT 3. However, as Liu et al (2001) notes, the equations by Schotanus et al (1983) are valid, only that they deal with one transducer. The extension of formulations by Schotanus et al (1983) to cater for cross wind effects on 3

path averaging results in temperature variance and flux equations that are largely similar to those by Schotanus et al (1983) but with extra terms at the end. The sensible heat flux correction is thus formulated as:

$$\overline{w'T_c'} = \overline{w'T_s'} - 0.51\overline{w'q'}\overline{T} + \frac{2\overline{T}}{c^2}(\overline{w'u'}\overline{u}A + \overline{w'v'}\overline{v}B) \qquad \text{(Equation 15)}$$

Where c^2 is the speed of sound, A and B are sensor specific factors (Foken, 2008b; Liu et al., 2001), T_c is the corrected temperature, T_s is sonic temperature. The prime and over bars follow the Reynolds decomposition convention.

3.3.2. Coordinate Rotation (Tilt Correction)

Coordinate rotation tries to resolve the misalignment of eddy covariance instruments in relation to the slope or gradient of the land surface. Such misalignment results in flux errors and generally, the non-closure of eddy covariance theory through violation of the assumptions on which the theory is built on. Considering that most land surfaces are not 'ideally' flat and the anemometer cannot be aligned correctly this correction is thus essential. This correction seeks to: 1) make the mean vertical velocity zero ($\overline{w} = 0$) , 2) force the cross wind velocity to zero ($\overline{v} = 0$) and 3) force also the covariance of u and v to zero, $\overline{(u'v')} = 0$ (Foken, 2008b; Lee et al., 2004; Wilczak et al., 2001). The Double rotation method is reviewed as it is applied in this research.

The double rotation method after Kaimal and Finnigan (1994) transforms the sonic anemometer coordinate system into that of the streamlines. A streamline is defined as coordinate lines that arise from averaging flow data over a particular time period. In this correction, the coordinate rotation is first done around the z axis into the mean wind direction and secondly around the new y-axis until the mean vertical wind is zero. These rotations are shown graphically in Figure 3-2 with subscript m denoting the measured velocity. Subscript 1 and 2 denotes the 1st or 2nd rotation. The equations are stated below.

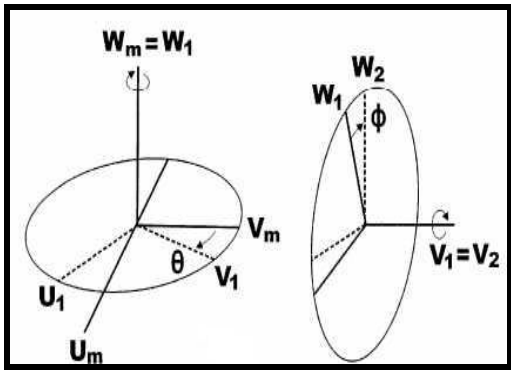

Figure 3-2: Double Rotation, after Foken (2008b)

The first rotation is achieved by the following formulation:

$$u_1 = u_m \cos\theta + v_m \sin\theta \quad v_1 = -u_m \sin\theta + v_m \cos\theta \quad w_1 = w_m \qquad \text{(Equation 16)}$$

Where: $\theta = \tan^{-1}\left(\frac{\overline{v_m}}{\overline{u_m}}\right)$

The second rotation is done in following manner:

$$u_2 = u_1 \cos\phi + w_1 \sin\phi \quad v_2 = v_1 \quad w_2 = -u_1 \sin\phi + w_1 \cos\phi \qquad \text{(Equation 17)}$$

Where: $\phi = \tan^{-1}\left(\frac{\overline{w_1}}{\overline{u_1}}\right)$

It is evident that double rotation aligns the x-axis with the mean wind vector, but the y and z-axes are given room to freely rotate about x (Wilczak et al., 2001).

3.3.3. Burba Correction

Burba et al (2008) recently explored a new challenge with regards to eddy covariance measurement instrumentation that could be central in improving flux estimates accuracy especially when open-path gas analyzers are used. Concerns of Burba et al (2008) centre on the effect of instrument's surface temperature on the turbulent fluxes. Burba et al (2008) discovered that the temperature of the gas analyzer was ~ 6^0C higher during daytime due the instruments electronics and radiation loading and even at nighttime the instrument's temperature was slightly higher. Burba et al (2008) also noted that there was a correlation between the temperature and vertical velocity hence sensible heat flux can be contaminated.

3.3.4. WPL Correction

Webb et al (1980) presented a 'plausible' argument on the effect of density fluctuations. Webb et al (1980) argued that when there is a positive heat flux then the rising air parcels are warmer and therefore less dense than those that going down (colder air parcels) – on the principle of mass balance. Therefore to maintain a balance, the vertical velocity of rising air has to be higher than that of the colder and denser descending air (Fuehrer and Friehe, 2002; Liebethal and Foken, 2003; Webb et al., 1980). Thus the conceptual simplification of flux calculation of by $F_c = \overline{w'\rho_c'}$ does not hold. The mean components have to be included and the flux calculation equation takes the form:

$$F_c = \overline{w'\rho_c'} + \overline{w} \cdot \overline{\rho_c} \qquad \text{(Equation 18)}$$

To get the mean wind velocity Webb et al (1980) introduce an assumption that the mean vertical dry air flux is equal to zero ($\overline{w\rho_a} = 0$) and therefore mean velocity is:

$$\overline{w} = -\frac{\overline{w'\rho_a}}{\rho_a} \qquad \text{(Equation 19)}$$

Using the above formulation into an equation that they has derived for density fluctuations (Webb et al., 1980), the approximate equation for calculating the vertical velocity was given as:

$$\overline{w} = \mu\frac{\overline{w'\rho_v}}{\overline{\rho_a}} + (1+\mu\sigma)\frac{\overline{w'T'}}{\overline{T}} \qquad \text{where } \mu = \frac{m_a}{m_v} \text{ and } \sigma = \frac{\overline{\rho_v}}{\overline{\rho_a}} \qquad \text{(Equation 20)}$$

Where the subscripts 'a' and 'v' indicate dry air and water vapour respectively, T is air temperature and m is the molecular mass of the respective air constituent (Liebethal and Foken, 2003; Webb et al., 1980). The flux of water vapour is eventually given as:

$$E = (1 + \mu\sigma)\left(\overline{w'\rho_v'} + \frac{\overline{\rho_v}}{\overline{T}} \overline{w'T'} \right)$$ (Equation 21)

This gives a corrected evapotranspiration flux, taking into account corrections that stem from water vapour and heat (Webb et al., 1980).

The focus on the WPL or Webb correction after Webb et al (1980) here is not blind to recent debate over the formulation of the Webb correction. It is noted that there are current concerns over a number of aspects of the Webb correction by Webb et al (1980) such as the assumption $\overline{w\rho_a} = 0$, the fact that Webb et al (1980) ignore the pressure covariance term which should be critical during windy turbulent conditions (Fuehrer and Friehe, 2002; Massman and Lee, 2002), and that contrary to Webb et al (1980), Paw U et al (2000) noted that the vertical velocity is sufficient enough to be measured. Whilst Liu (2005) tried offer an alternative conceptualisation of the Webb term by proposing the use of volume fluctuations but this is not proper as volume fluctuations cannot be expected in a control volume, only density fluctuations are plausible (Leuning, 2007). Liu's (2005) alternative ideas have also been rejected also by Kowalski (2006), Massman and Tuovinen (2006), Leuning(2005; 2007). Leuning (2005; 2007) showed that the original formulation by Webb et al (1980) is still valid and works for both steady and unsteady homogenous flows. It is evident from the published work that the essence of the Webb correction after Webb et al (1980) is correct although there seems to be problems with the formulation of vertical velocity, which is still being debated.

3.3.5. Averaging, Detrending and Filtering

Eddy covariance operations are done in either time or frequency domain. The latter is used in spectral analysis and time averaging forms the basis of theoretical formulations, as demonstrated by Reynold's decomposition. Time averaging is done when an average is defined over a certain time span. The data or signal is digitally sampled and thus time averaging and mean removal are done in discrete form over the n_s samples (Moncrieff et al., 2005). Linear detrending establishes the mean by finding the line of best fit over a time period i.e. a linear trend and that is subtracted (Moncrieff et al., 2005). Filtering is the convolution of the signal e.g. w(t) with a window function (Moncrieff et al., 2005).

3.3.6. Frequency Response Correction

Eddy covariance employs an array of equipment in its measurements. A sonic anemometer measures wind speed and sonic temperature, whilst scalar density fluctuations are measured by a different instrument. These sensors have different response characteristics with scalar sensors generally exhibiting a slow response. Furthermore there is some spatial separation of the instruments and also averaging effects, which result in high frequency attenuation. Low frequency attenuation is associated with block averaging, by high-pass digital filtering or linear detrending of raw data (Massman, 2000). Also central is the ability of the instruments to measure at a fast rate – high sampling frequency – and logging speeds. Slow logging is not good for fast evolving eddies, which might end up folding around the nyquist frequency of the instrument or logger. When folding occurs, some of the data appears as low frequency eddies which will not be true. It is thus essential that there be frequency response corrections

Moore (1986) presented a key paper on this subject with correction equations based on the convolution of frequency dependant response functions. As the equations are diverse they are thus not presented in this review. Massman (2000) presents analytical formula dealing with flux loss due to attenuation by making use a formula developed by Horst (1997) to estimate the attenuation of a scalar flux. The formulae attempt to resolve the problem associated with resolution of very small and very large eddies.

3.4. SAP FLOW AND UP-SCALING

The movement of sap or water in a tree stem is the conceptual basis of sap flow approach. Sap moves up the tree in response to the water potential difference that exists between the soil and the atmosphere. The rate at which sap flows is then used to estimate tree transpiration (Granier, 1985; 1987; Lubczynski, 2008). However there seemingly exists confusion over the proper definition of some terms, such as sap flow and sap flux density. Sap flux density is the volume of sap flow per unit time per unit area. The symbols for sap flux density are either J_v or J_p [L^3 L^2 T] (Lemeur et al., 2009).

On the other hand, sap flow (Q_s) is a defined as sap flux density that is integrated over a certain surface area and can therefore be defined as:

$$Q_s = \iint_{Ax} J_v \cdot da \qquad \text{(Equation 22)}$$

Where J_v is the sap flux density [L^3 L^{-2} T] and A_x is the xylem or sapwood area [L^2]. The output Q_s has the units [L^3 T^{-1}] (Lemeur et al., 2009).

The study of sap flow has taken different approaches and therefore different methods to measure sap flow have emerged. Some of the methods include: heat deformation (HFD), thermal dissipation (TD), heat pulse velocity (HPV) and trunk heat balance (THB) (Čermák et al., 2004; Cermak and Nadezhdina, 1998; Wullschleger et al., 1998). Thermal dissipation approaches have received widespread applicability in research studies because of their simplicity and yet reasonable results (Čermák et al., 2004; Lu et al., 2004). A thermal dissipation based approach that has been widely used is the Granier thermal dissipation probe (TDP) method (Granier, 1985; 1987). The Granier thermal dissipation probe (TDP) method is thus applied in this thesis.

The method by Granier (1985; 1987) is premised on the determination of sap velocity from the temperature difference between two probes inserted into the stem of a plant. A temperature difference arises because one of the probes is constantly heated and the other one is not heated. The velocity of sap is then inferred from the dissipation of heat. As water moves in the xylem, heat dissipation occurs. As such it can be concluded that as the sap velocity increases, the temperature difference between the probes will decrease. Granier formulated the eventual equation(s) by relating sap flow and temperature differences. The coefficients were determined by non-linear regression (Granier, 1985; 1987) . For the equations see (Equation 45) to (Equation 47)

From a hydrological perspective, there is need to determine fluxes in a given area and therefore the up-scaling of individual tree sap flow to area estimates of sap flow or transpiration flux is essential.

Different up-scaling approaches have been applied and some include; the 'keeling' plot approach (Williams et al., 2004), the use of models, the use of biometric parameters or variables (Čermák et al., 2004; Lubczynski, 2009) and the use of remote sensing (Chavarro-Rincon, 2009; Chen et al., 2006; Lubczynski, 2009). Čermák et al.(2004) provides a comprehensive treatment of sap flow up-scaling, for which a complete review is beyond the scope of this research.

Up-scaling of sap flux density requires parameters (scalars) to use in the up-scaling. The up-scaling parameters relate a certain measurable component of a tree to the sap flux density. The relation between such a component and sap flux density is then used to estimate the sap flow of trees that were not measured. The up-scaling parameters that have been used vary from study to study. Some parameters used include, the diameter at breast height (DBH), the projected canopy area (A_c), the xylem or sapwood area (A_x), the distance between stems, and in some instances Leaf Area Index (LAI) has been used (Cermak and Nadezhdina, 1998; Chavarro-Rincon, 2009; Lubczynski, 2009; Wullschleger et al., 1998). The diameter at breast height (DBH) and sapwood area are often used. This can be explained the work of Meinzer et al (2001) that demonstrated the existence of an allometric scaling relationship between DBH and sap flow or sap flux density.

When up-scaling in WLE, over large areas, the application of remote sensing is the most efficient approach. While Leaf Area Index (LAI) has been used in remote sensing based up-scaling, Lubczynski (2009) argues that this might not be feasible in WLE because leaf turnover is fairly slow and yet transpiration responds swiftly to changing forcing factors. The use of species-specific biometric up-scaling functions is thus more appropriate (Lubczynski, 2009). It follows therefore that the accuracy of up-scaled flux depends on how good the biometric up-scaling function (BUF) is. This is dependant on the representativeness of the samples that would have been taken. Applying some Monte-Carlo simulations, Kumagai et al (2005) showed potential errors in transpiration were low and nearly stable with a sample of > 20 per specie.

3.5. EDDY FLUX FOOTPRINT

In a general sense, the terms footprint and source area are used loosely for the same thing (Schmid, 1997; Vesala et al., 2008). The same will be done in this research. A footprint is the area (mostly upwind) that contributes to or influences a measured flux at a particular location (Schmid, 1997; Schuepp et al., 1990; Vesala et al., 2008). However, by strict definition a source area is a portion of land surface that has the sources and sinks that contribute to a measured flux. The term footprint (Schuepp et al., 1990) or source weight function (Schmid, 1997) represents the relative contribution of each part or element of the upwind source area. The footprint function can thus be understood as a 'mean probability' that a 'flux particle released' from a certain elemental land surface will reach the measurement point (Kljun et al., 2002). In this research, as in most published research work, the terms footprint and source weight function are used loosely.

The underlying concepts of the different footprint determination methods (analytical, Lagrangian, one-and-half turbulence closure) are presented in the work of: Rannik et al. (2003), Schuepp et al. (1990), Schmid (1994), Schmid (1997), Sogachev et al. (2004), Kljun et al. (2002), Finnigan (2004) and Gryning et al. (1987). The conceptual development presented herein follows after the work of Schmid

(1994; 1997). The formal description of the concept of footprint estimation starts with the integral equation of diffusion that accounts for the distribution of a diffusing quantity into the atmosphere, as stated by Pasquill and Smith (1983) in (Schmid, 1994):

$$F(r) = \int_R Q_\eta(r') \cdot f(r - r') - dr' \qquad \text{(Equation 23)}$$

$F(r)$ is a scalar concentration or vertical turbulent flux measured at point r, with its origins in an area with source strength Q_η at r', f is a probability transfer function between points r and r' and integration is over the domain R. When the strength of the source area is restricted to ground surface $z = z_0$, the diffusion parallel to the mean wind direction - along the x-axis, can be ignored when measuring from point z_m such that the coordinates $x, y, z = 0, 0, z_m$. The integral diffusion equation can thus be written as:

$$F(0,0,z_m) = \int_{-\infty}^{\infty}\int_{-\infty}^{x} Q_\eta(x, y, z = z_0) \cdot f(-x,-y,-z_m - z_0) \cdot dx \cdot dy \qquad \text{(Equation 24)}$$

The term $f(-x,-y,-z_m - z_0)$ relates the observed flux F at (0, 0, z_m) to the source distribution on the land surface. Conceptually this is the source weight function (Schmid, 1994). Evidently, there is also dependence on the distance from the observation point. The source weight function can thus be understood to increase up to a certain maximum (f_{max}) and then it will recede as the separation distance with the observation point increases. Figure 3-3 diagrammatically presents this concept. It can be noted that f_{max} occurs at a certain upwind distance. The spatial extent covered by the normal projection of the isopleths (f_p) on the x-y plane is the level P source area (Ω_P). It should be noted that mean wind direction is counter the x-axis direction but parallel and turbulence is assumed to be horizontally homogenous (Schmid, 1994; 1997)

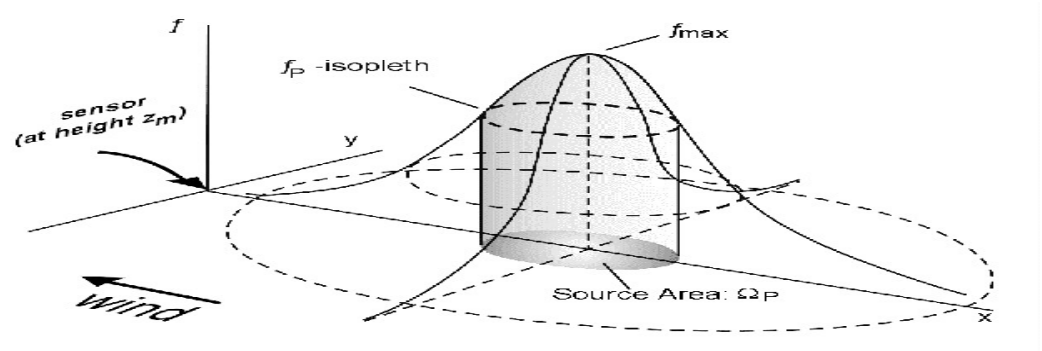

Figure 3-3: Source Area and the Source Weight Function after Schmid (1997).

Figure 3-4 shows the typical dimensions of the source area; a is the near-observation point limit and e is the far end limit. The distance can be computed by a footprint determination method. Most 1D footprint models estimate the far field limit. X_m is where the peak (f_{max}) should occur and d is maximum half-lateral spread distance.

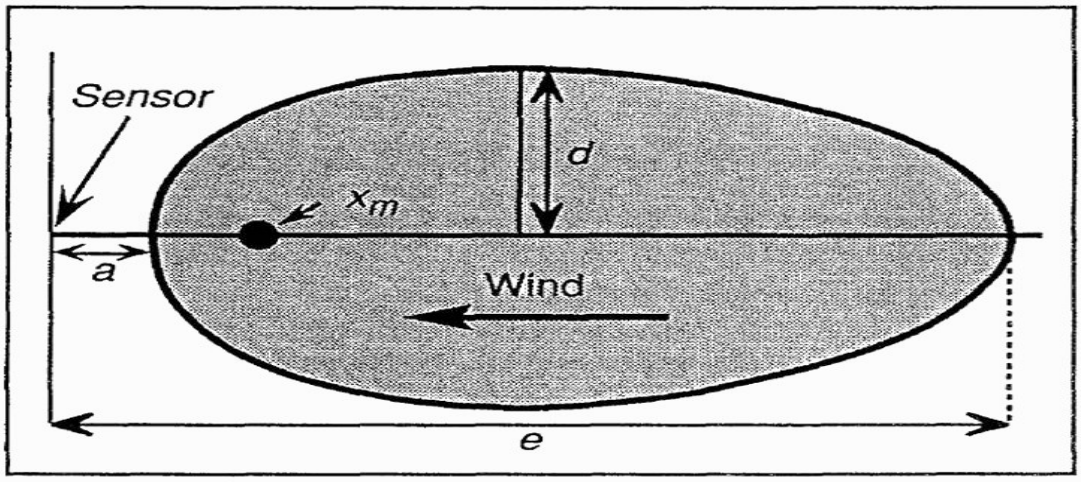

Figure 3-4: Typical Source Area Dimensions (Schmid, 1994)

3.5.1. TYPES OF FOOTPRINT ESTIMATION METHODS.

The determination of flux footprints follows typically two meteorology or fluid mechanics frameworks i.e. the Eulerian and Lagrangain frameworks. The generic classification of footprint determination methods is:

1. Analytical flux footprint models e.g Schuepp et al (1990), Hsieh et al (2000)
2. Lagrangian footprint models e.g. Kljun et al. (2002), Rannik et al. (2003)
3. One-and-A-Half Order Closure Model e.g. Sogachev et al (2004)
4. Large eddy simulation

Large eddy simulation represents one of the best solutions available buts its computationally intensive, hence its not reviewed in this thesis together with the One-and-half order closure models.

ANALYTICAL FLUX FOOTPRINT METHODS

Analytical footprint estimation models are based on analytical solutions of the advection dispersion equation (Kim et al., 2006) or second order turbulence schemes together with scaled large eddy simulation results or Lagrangian stochastic models (Hsieh et al., 2000; Kljun et al., 2002). The major advantage of analytical models is that they are pragmatic and provide reasonable results (Marcolla and Cescatti, 2005). This allows for common use and replication of approaches.

A commonly applied analytical model is that of Horst and Weil (1994). The model like some analytical models, assumes horizontal flow homogeneity and negligible stream wise eddy diffusion The Horst and Weil (1994) model also accounts for atmospheric stability and the logarithmic wind profile above the canopy (Lecleck, 2003). Another solution that has been used frequently is the approximate analytical solution by Hsieh et al (2000). The approximate solution by Hsieh et al (2000) combines the outputs from Lagrangian stochastic dispersion models and a length scale that is a function of the measuring height (z_m) and the z_0. The solution by Hsieh et al (2000) is presented in the following chapters as it is the basis of this research.

LAGRANGIAN STOCHASTIC DISPERSION MODELS.

Lagrangian stochastic dispersion models (LSDM) account for the evolution of particle position and velocity by means of a (near) Markov process. Thus LSDM attempt to describe the evolution of passive scalars in turbulent flow by tracking their trajectories (Hsieh et al., 2000; Gockede, 2004; Mortarini and Ferrero 2005; (Wilson and Sawford, 1996). LSDM are far much more flexible tools, in the sense that they can be used for in-canopy and over the canopy footprint considerations. However, there are not easily implementable compared to analytical models.

Conceptually, the governing LSDM equations as outlined by Hsieh et al. (2000) are outlined below. The progression of particle position in the *x*–direction is given by:

$$x^{n+1} = x^n + U^n \Delta t \qquad \text{(Equation 25)}$$

And the progression in the *z* direction is given by;

$$z^{n+1} = z^n + w^n \Delta t \qquad \text{(Equation 26)}$$

The superscript *n* symbolizes the n^{th} time-step, *w* is the instantaneous particle velocity in the *z*-direction and Δt is the time increment. Based on the Markov assumption, the evolution of *w* can be expressed by:

$$dw = a(z,w,t)dt + b(z,w,t)d\lambda \qquad \text{(Equation 27)}$$

a is known as the drift co-efficient, *b* is the random acceleration co-efficient and $d\lambda$ is a Gaussian random variable with zero mean and variance *dt*. A brute treatment of the concept and the formulation for the *a* and *b* coefficients can be found in Hsieh et al. (2000) and other work by Rannik et al (2003), Wilson and Sawford (1996) and Kurbanmuradov and Sabelfeld (2000). The Gaussian random variable, $d\lambda$, is sometimes defined as the Wiener process.

4. METHODOLOGY

4.1. METHODOLOGY FLOW CHART.

Figure 4-1 presents the methodology flow chart of this research based on the major concepts. The calculations related to these concepts are outlined in later sections.

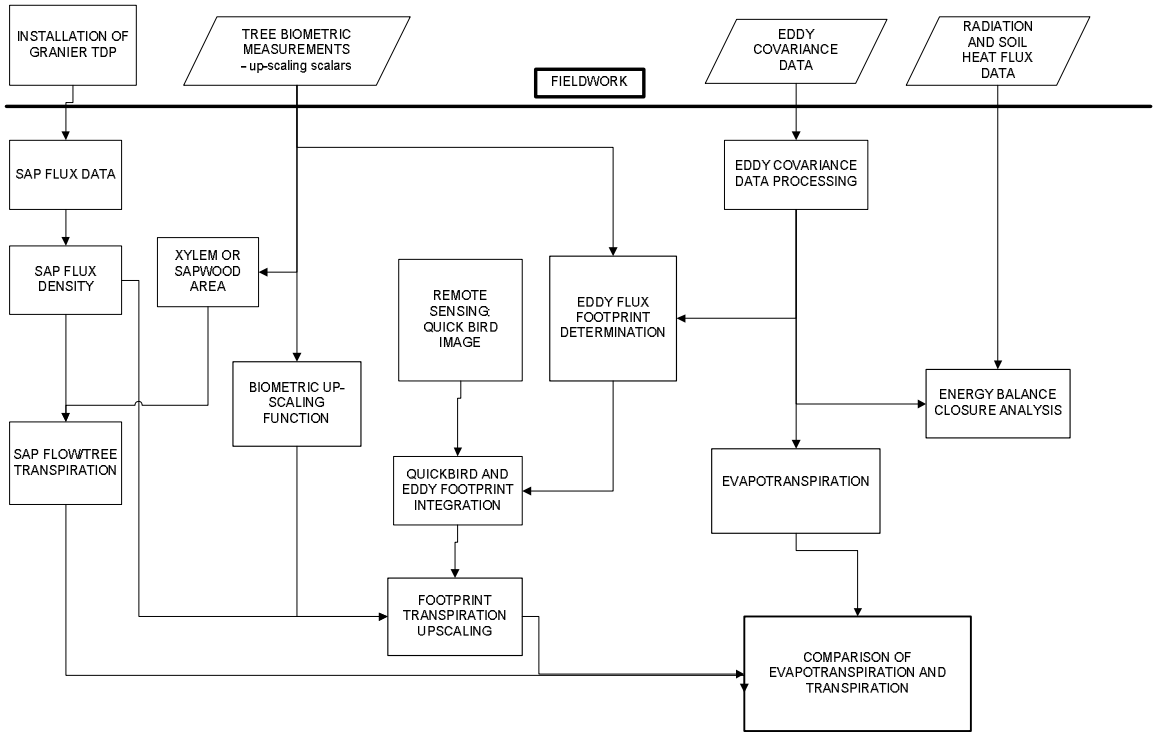

Figure 4-1: Research methodology flow chart - the major concepts

4.2. FIELD EDDY COVARIANCE AND RADIATION INSTRUMENTATION.

The instruments used in this study to measure turbulent heat fluxes, net radiation and meteorological variables were mounted on a ten (10) metre high aluminium tower (the "eddy tower"). The eddy tower was erected in Trabadillo, Spain by Leonardo Reyes, Alain Frances and Dr C van der Tol in July 2009. A brief description of the instruments mounted on the tower is provided here below.

Turbulence measurements were made using a CSAT-3 (Campbell scientific, USA) 3-D sonic anemometer. The CSAT-3 measures sonic temperature (T_s) and the stream wise, cross-wind and vertical wind speeds, u_x, v_y, and w_z respectively. The measurements are made using pairs of 3 non-orthogonally oriented transducers over a path that is vertically 10 cm long and horizontally 5.8 cm wide.

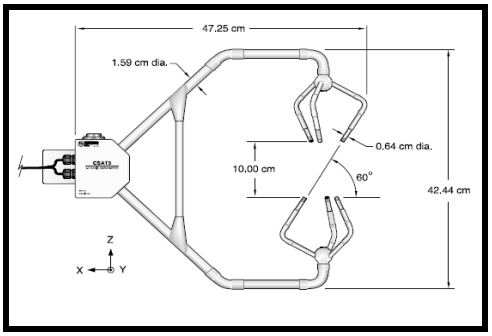

Figure 4-2: CSAT-3 (Campbell Scientific, 1996)

Figure 4-2 gives a pictorial description of the 3-D sonic anemometer used in this research and its dimensions (Campbell Scientific, 1996)

The net radiation budget components were measured using a CNR 1 Net Radiometer (Kipp & Zonen, Delft, Netherlands) - Figure 4-3. The CNR 1 Net Radiometer measures: shortwave incoming (SW↓), shortwave outgoing (SW↑), long wave incoming (LW↓) and long wave outgoing (LW↑) radiation separately through upward and downward facing pyranometers and pyrgeometers. The total spectral range measured is from 0.3 to 42 micrometers (μm). The pyranometers measure solar radiation (0.3 – 3 μm) and the pyrgeometers measure far-infrared irradiances (4.5 - 42 μm) ranges (Kipp & Zonen, 2002).

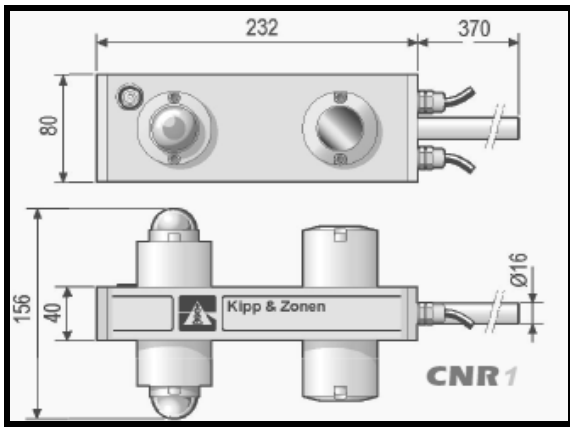

Figure 4-3: CNR 1 Net Radiometer (Kipp & Zonen)

Scalar concentrations of water vapour (H_2O) were measured by the LICOR LI 7500 (Licor Inc, USA) open-path CO_2/H_2O infrared gas analyzer. The measuring principle is based on the absorption of a scalar at two wavelengths. At one of the wavelengths the scalar is absorbed and at the other wavelength the scalar is not absorbed. The concentration is then inferred from the difference of the two wavelengths.

Soil heat flux was measured using Hukseflux soil heat flux plates. Two of the plates were buried at a depth of 1 cm and the other one at 10 cm depth. The deeper one was used in a different soil heat flux calculation that included two TCAV-L Averaging Soil Thermocouple Probes (Campbell Scientific, USA) at 3 and 7 cm depth. Each TCAV-L sensor consists of three smaller sensors, from which the average temperature is recorded.

The Vaisala weather transmitter WXT520 (Vaisala, Finland) was used to measure meteorological variables. The Vaisala weather transmitter WXT520 measures: air pressure, rainfall (duration and intensity), air temperature, relative humidity (RH), wind direction and wind speed. The Vaisala was installed by C van der Tol and was aligned to the North.

4.3. EDDY TOWER CONFIGURATION AND MEASURED VARIABLES.

The configuration of the instruments on the eddy tower and measured variables presented in Table 4-1.

Table 4-1: Eddy Tower Instruments

INSTRUMENT	HEIGHT*	THEMATIC CLASS	VARIABLES
3-D CSAT (Campbell Scientific)	10m	10 Hz Turbulence Data Sonic Temperature (Ts)	Ux, Uy, Uz, T_s
Licor 7500 Gas Analyzer (Licor Inc)	10m	Gas Concentrations	Conc H_2O
CNR 1 Net Radiometer (Kipp and Zonen).	10m	Net Radiation (R_n budget)	SW↓, SW↑, LW↑, LW↑ and R_{sensor}
Hukseflux Plates (2 plates).	- 0.01m	Soil Heat Flux - set up 1	SHF 1 and SHF 2
TCAV sensors (Campbell Scientific) 3 and 7 cm and a Hukseflux plate	TCAV -0.03m & -0.07m SHF 3 -0.10m	Soil Heat Flux - set up 2	T_{3cm}, T_{7cm} & $SHF3_{10cm}$
Vaisala	10m	Meteorological	Wind Direction, RH, Temp

- *Refers to the height at which the instrument was mounted.
- SHF: Soil Heat Flux
- R_{sensor} – refers to the temperature of the CNR 1 net radiometer which is used to correct long wave radiation data based on the Stefan Boltzmann law.

4.4. NET RADIATION

Net Radiation (R_n) [W m^{-2}] was determined as the balance of incoming and outgoing shortwave and long wave energy fluxes measured by the CNR 1 Net Radiometer (Kipp & Zonen, Delft). The calculation is expressed as:

$$R_n = (SW\downarrow - SW\uparrow) + (LW\uparrow - LW\downarrow) \quad \text{(Equation 28)}$$

Where ↑ indicates outgoing radiation and ↓ incoming radiation. SW and LW refer to shortwave and long wave radiation [W m^{-2}] respectively.

The measured long wave radiation needed to be corrected for the radiation related to the instrument. This was done by taking into account the temperature of the instrument, which was measured with a PT100 resistance (T_{pt_100}). As the radiometer emits radiation, the Stefan-Boltzmann law was used to determine a correcting flux based on the PT100 resistance based temperature. The correcting flux was added to the measured long wave radiation. The equation for the correcting long wave flux (LW_{corr}) [W m^{-2}] is:

$$LW_{corr} = \varepsilon_s \sigma_{SB} T^4_{pt\_100} \quad \text{(Equation 29)}$$

Where ε_s is emissivity [-], σ_{SB} is the Stefan-Boltzmann constant (= 5.67*10-8 W m^{-2} K^{-4}), T_{pt_100} is the measured PT100 temperature [K]. Net Radiation (R_n) [W m^{-2}] was therefore calculated by:

$$R_n = (SW\downarrow - SW\uparrow) + ([LW\uparrow_{meas} + LW_{corr}] - [LW\downarrow_{meas} + LW_{corr}]) \quad \text{(Equation 30)}$$

Where $LW\uparrow_{meas}$ is the measured outgoing long wave radiation [W m^{-2}] and $LW\downarrow_{meas}$ is the measured incoming long wave radiation [W m^{-2}].

4.5. SOIL SURFACE TEMPERATURE

The effective ground temperature or kinetic temperature was determined by back-calculation from outgoing long wave radiation. An emissivity value of 0.97 for bare soil was used (Brutsaert, 2005). A bare soil emissivity of 0.97 was used because eddy tower was situated over bare soil. The calculation was done as follows:

$$T_G = \left(\frac{LW\uparrow_{meas}}{\varepsilon_{bs} \cdot \sigma_{SB}} \right)^{\frac{1}{4}} \quad \text{(Equation 31)}$$

Where T_G is the effective ground temperature or kinetic temperature [K] and ε_{bs} is the dry bare soil emissivity of 0.97 (Brutsaert, 2005).

4.6. SOIL HEAT FLUX

The determination of the soil heat flux was done in two parts. Firstly, by simply taking the average of the readings of soil heat flux plate 1 and 2 that were at the same depth (1 cm), and secondly by using the set up with temperature probes and a soil heat flux plate at 10 cm depth (Equation 32) . The second soil heat flux set up was implemented because of the possibility of having unreliable results from using soil heat flux plates alone. Ochsner et al (2006) showed that commercially available soil heat flux plates underestimated soil heat flux by between 2 – 38% in dry sand and 13 – 73% in saturated soil.

As part of data processing, to determine the feasibility of averaging the data from the two plates at 1cm a correlation analysis was done after checking for outliers. The R^2 value was 0.98. The average of soil heat flux plate 1 was 7.7 W m^{-2} with a standard deviation of 72.17 and a standard mean error of 0.97. The mean of soil heat flux plate 2 was 13.92 W m^{-2}, with a standard deviation of 78.42 and a standard mean error of 1.059, n = 5 480). It was also important to determine if the means of soil heat flux plate 1 and 2 were significantly different before averaging. An independent t-test was applied and the results are as tabulated in Table 4-2 (N=5 480, 95% Confidence Interval).

Table 4-2: Correlation of Soil Flux Plates Data (Set Up 1)

	Levene's Test for Equality of Variances		t-test for Equality of Means				
	F	Sig.	t	df	Sig. (2-tailed)	Mean Difference	Std. Error Difference
Equal variances not assumed	50.443	.000	-4.295	10883.123	.000	-6.1833467	1.4396741

The significance of Levene's test was below 0.05 and therefore "equal variances not assumed" was used as presented in Table 4-2. The significance (2-tailed) being less than 0.05 as test was done at 95% confidence interval means that there is no significant difference in the means of the SHF plates 1 & 2. There being no statistically significant difference, the soil heat flux data of the two plates at 1cm was averaged.

Soil heat flux was also determined by a more reliable method that considers heat storage in the upper soil profile (Brutsaert, 1982; 2005). The soil heat flux calculation with heat storage was done according to the following equation:

$$Go_{storage} = Go_{10cm} + \int_{0cm}^{10cm} C_s \frac{\partial T}{\partial t} dz \quad \text{(Equation 32)}$$

Where $Go_{storage}$ is the soil heat flux that includes storage [W m^{-2}], Go_{10cm} is the soil heat flux measured at 10 cm depth [W m^{-2}], C_s is the volumetric heat capacity [J m^{-3} K^{-1}], T is soil temperature [K] and *dz* is the depth[m]. The volumetric heat capacity was determined based on a equation that simplifies the analytical solution of De Vries (1963) as follows:

$$C_s = (0.837\rho_b + 4.19\theta)10^6 \quad \text{(Equation 33)}$$

Where C_s is the volumetric heat capacity [J m^{-3} K^{-1}], ρ_b is the bulk density [g cm^{-3}] and θ is volume fraction of water [-] and the term 4.19 approximates the heat capacity of water [J g^{-1} K^{-1}]. The bulk density used was 1.48 and the calculated volumetric heat capacity ranged between 1.548 -1.563 [J m^{-3} K^{-1}].

The final soil heat flux calculation was done by discretizing the integral over two conceptual compartments, the 0-5 cm and 6-10 cm depth. The temperature measurements at 3 and 7cm were taken as the mid points of these compartments, such that the calculation was done as follows:

$$Go_{storage} = C_s \cdot \left(\frac{(\Delta T_{3cm} \cdot 0.05) + (\Delta T_{7cm} \cdot 0.05)}{t} \right) \quad \text{(Equation 34)}$$

Where t is the time interval in seconds, ΔT_{3cm} and ΔT_{7cm} are the temperature differences at each depth (3 and 7cm). 0.05 is the depth of each conceptual compartment in meters.

4.7. TURBULENT HEAT FLUXES (EDDY COVARIANCE).

The theoretical background and computations involved in eddy covariance have been reviewed in Chapter 3. Thus the processing procedures are outlined in this section. Data handling included downloading data from the CR 5000 logger (Campbell Scientific, USA). Upon downloading the data was converted from the binary version to TOA5 compatible file formats. A visual inspection of the data was done by plotting the data using Logger net (Campbell Scientific, USA). The datasets were visually inspected for missing data and NaN's (Not a Number). Records that contained NaN were removed. Most NaN's occurred after the removal of the removable data card for data downloading. A few records were affected.

Turbulent heat fluxes, friction velocity, mean wind speed, sonic temperature and wind variances were determined by using an eddy covariance processing software called AltEddy. AltEddy was developed by ALTERRA, Wagenigen University, The Netherlands. Data processing was done at 30 minute intervals and the settings used are outlined in this section.

Consistency limits ensure that the values used in the calculation do not exceed acceptable thresholds. Potentially erroneous data is thus excluded from the calculation thereby improving on data quality. The consistency limits applied are as tabulated in Table 4-3.

Table 4-3: Consistency Limits for eddy covariance processing.

Variable	Lower Limit	Upper Limit	Alteddy Code
Sonic U lower limit in m/s	-30		LILO(a)
Sonic U upper Limit in m/s		+30	LIHI(a)
Sonic V lower limit in m/s	-30		LILO(b)
Sonic V upper Limit in m/s		+30	LIHI(b)
Sonic W lower limit in m/s	-30		LILO(c)
Sonic W upper Limit in m/s		+30	LIHI(c)
Sonic T lower limit in Kelvin	263		LILO(d)
Sonic T upper Limit in Kelvin		313.15	LIHI(d)
LICOR 7500 H2O lower limit in mmol/m3	0		LILO(e)
LICOR 7500 H2O upper Limit in mmol/m3		CALIB	LIHI(e)

Spikes are encountered as result of random electronic spikes or the blockage of transducers. Spikes when unattended lead to random noise (Aubinet et al., 2000). Spikes were determined as the degree of deviation from the mean as a percentage (MSPI) that relates to the upper and lower limits set under the consistency limits. Thus a spike is detected when a sample deviates from the mean by more than $\left(\frac{MSPI}{100}\right) * \left(LIHI(\ ) - LILO(\ )\right)$. Thus a low percentage value is more restrictive than a high value. The MSPI used in this study is 8%. The basic output time interval of 30 minutes was used.

4.7.1. Corrections

The corrections applied in data processing are: frequency response (Moore, 1986), Burba (Burba et al., 2008), WPL (Webb et al., 1980) and double rotation. Planar fit rotation and double rotation were both tested and it was realised that planar-fit rotation tended to give more spiky fluxes. As plant-fit rotation is more suited to long-term studies, it was noted that the study period was too short to get consistent results with planar fit correction and hence double rotation was used.

For frequency response corrections, the LICOR 7500 (Licor Inc) open path time constant (TAUCO) was given as 0.10 (10Hz) and the optical path of the LICOR which is 12 centimetres long resulted in an open path length (PCO) of 0.12 m. Frequency response corrections also need to take into account the separation distance of the LICOR 7500 and the sonic anemometer. The spatial separation between the instruments was ~ 11 cm. Daily air pressure was determined from meteorological data measured by the Vaisala that was mounted at the same height as the sonic anemometer.

Based on an average canopy height of 6 metres the zero-plane displacement was determined by

$$d_0 = 0.67 * h \quad \text{(Equation 35)}$$

4.8. QUALITY ANALYSIS OF EDDY COVARIANCE DATA.

The AltEddy processing software used also has the eddy covariance data quality analysis scheme after Foken et al (2004). The scheme utilises the stationarity and the integral turbulence characteristics test. Stationarity can be simply defined as the time independence of the statistical moments of a random variable (Katul et al., 2004). The integral turbulence characteristics test assess the degree of turbulence development (Foken et al., 2004; Foken and Wichura, 1996).

The full class definition of the quality scheme is provided in appendix 2. The quality assessment is based on percentage deviations. For example, when doing 30 minute averages, stationarity is confirmed when the 5 minute interval covariance's of vertical velocity and a scalar do not differ by more than 30% with the 30 minute covariance of the same scalar and vertical velocity (Foken et al., 2004; Foken and Wichura, 1996).

4.9. ENERGY BALANCE CLOSURE

The energy balance analysis was based on the assessment of the surface energy balance equation using the independently measured net radiation, soil heat flux, and turbulent heat fluxes. The surface energy balance equation is expressed as:

$$R_n = H + \lambda E + G_0 \quad \text{(Equation 36)}$$

Where R_n is net radiation [W m^{-2}], H is sensible heat flux [W m^{-2}], λE is latent heat flux [W m^{-2}] and G_0 is soil heat flux [W m^{-2}].

The degree of energy balance closure was analysed by plotting the sum of turbulent heat fluxes ($H + \lambda E$) against the available energy ($R_n - G_o$). The plot was then forced through zero and the position of the 1:1 line was used to determine the degree of energy balance closure. Under conditions of total energy balance closure the fitted line should be perfectly aligned along the 1:1 position. This is an approach widely used in literature, (Aubinet et al., 2000; Foken, 2008b; Mauder et al., 2007; Twine et al., 2000; Wilson et al., 2002). The same plot was also done using daily averaged fluxes as in the work of Baldocchi et al (2004).

The unaccounted for energy, the energy balance residual, EB_{res} [W m^{-2}] was determined by:

$$EB_{res} = R_n - (H + \lambda E + G_0) \quad \text{(Equation 37)}$$

The energy balance ratio or closure fraction [-] was determined by:

$$EBR = \frac{H + \lambda E}{R_n - G_o} \quad \text{(Equation 38)}$$

4.10. EVAPOTRANSPIRATION

The total evapotranspiration was determined from the measured latent heat flux at 30 minute intervals. Firstly the latent heat of vaporization as a function of air temperature (T_a) was determined as follows:

$$\lambda = 2.501 - 0.002361 T_a \quad \text{(Equation 39)}$$

Where λ is the latent heat of vapourisation [J kg^{-1}] and T_a is the temperature [^{0}C]. The average λ that was determined is 2.46 MJ kg^{-1}, with the minimum being 2.43 MJ kg^{-1} and the maximum 2.5 MJ kg^{-1}. The range of calculated λ was within acceptable limits, such as the value of 2.45 MJ kg^{-1} used in FAO-56 (Allen et al., 1998). Evapotranspiration *(ET)* was then computed by:

$$ET = \left(\frac{\lambda E}{\lambda} \right) \quad \text{(Equation 40)}$$

The total ET is the total evapotranspiration [mm s^{-1}]. To get the total ET flux over a 30 minute interval the ET was multiplied by 1800s

4.11. METEOROLOGICAL DATA

Meteorological data was measured by the Vaisala instrument. Plotting to visually check for bad data and illogical values was done. Illogical values could include a relative humidity > 100% or wind direction greater than 360^0. All the data that was checked was within logical limits. The data was then averaged to 30 minutes so as to match the time interval of the eddy covariance data. The meteorological data includes: relative humidity (RH), wind direction, air pressure, air temperature and wind speed.

The saturation vapour pressure (e_s) was determined as a function of temperature as follows:

$$e_s = 0.6108 \exp\left(\frac{17.27 + T_a}{T_a + 237.3} \right) \quad \text{(Equation 41)}$$

Where e_s is the saturation vapour pressure [kPa] and T_a is the air temperature. The partial pressure of water vapour or in simple terms the water vapour in a volume of air, the actual vapour pressure (e_a) was the determined as a function of e_s and RH as follows:

$$e_a = e_s \cdot \left(\frac{RH}{100} \right) \quad \text{(Equation 42)}$$

Where e_a is the actual vapour pressure [kPa]. The vapour pressure deficit, VPD, [kPa] was then calculated as:

$$VPD = e_s - e_a \quad \text{(Equation 43)}$$

4.12. SOIL MOISTURE

Data from a soil moisture profile installed by Alain Frances and Leonardo Reyes as part of their PhD work was used. The profile measures soil moisture at four depths, namely 25cm, 50cm, 75cm and ~ 100cm. The profile is equipped with theta Hydra probes (Stevenswater, USA).

4.13. SAP FLOW

4.13.1. Set up of thermal dissipation probes

Three *Q. pyrenaica* trees were selected for the installation of Granier thermal dissipation probe (TDP) system (Umweltanalytische Produkte GmbH) based on their near circular trunk structure and distance from the eddy covariance tower. The trees installed with the Granier TDP system were approximately 65 metres from the tower. Pictures of the installation are in appendix one (1).

The Granier TDP system installed consisted of two thermocouples that were inserted into the tree trunk. Before the thermocouples were inserted, two small holes with a depth of ~ 2 cm were drilled. The two holes were 10 cm apart as recommended by Lu et al. (2004). The holes were then lined with 2 cm length aluminium tubes, into which the thermocouples were inserted. The insertion was facilitated with silicon grease to prevent condensation and improve thermal contact.

The Granier TDP sensors were installed at minimum height of 135 cm. However this could not be done for tree number 1 because of a slight irregularity of the stem at 135cm height. The irregularity could have significantly biased the results and hence the probe was installed at 98cm. The TDP probes were installed in the north and shielded with an insulating cover to avoid the direct effect of the sun as shown in the Figure 4-4

Figure 4-4: Set up of Sun Shielded Granier TDP *Q. pyrenaica* Trees - Trabadillo 2009

The biometric characteristics of the three *Q. pyrenaica* trees that were installed with the UP (Umgbh, Germany) TDP systems are tabulated in Table 4-4

Table 4-4 : Biometric details of sap flow sampled trees

Biometric Variable	*Q .pyrenaica*, 01 cm	*Q. pyrenaica*, 02 cm	*Q. pyrenaica*, 03 cm
Measured Xylem Length (A_l)	3.9	3.4	3.9
DBH	21	22.6	24

Height of 1st Branching	245	250	210
Height of Sensor	98	145	135
Tree Height	575	685	850
X Coordinate (m)	739572	739574	739571
Y Coordinate (m)	4555892	4555898	4555886

The TDP measurement system was powered by 2 x 12 Volts batteries connected in series. These batteries were able to last for a period of four days before being changed. The data was logged using a Skye data logger, sampling and storing at a time interval of 10 minutes.

4.13.2. Sap Flux Density and Sap Flow

The temperature difference (*dT*) data from the Granier TDP probes was first screened by plotting and visually checking for abnormally high values. Data from TDP system number two, showed abnormally high values for the first two days - *dT* of ~ 70. This problem occurred on the first two days and the data was rejected. The cause of the problem was diagnosed as a probe malfunction. The malfunctioning probe was thus replaced on the second day.

The data processing steps applied essentially follow after the work of Granier (1985; 1987) and Lu et al.(2004) . After checking the *dT* data for consistency, the flow index (K) was determined by using the following equation:

$$K = \frac{\Delta T_m - \Delta T}{\Delta T} \qquad \text{(Equation 44)}$$

Where K is the flow index [-], ΔT_m is the maximum temperature difference and ΔT is the measured temperature difference. The maximum temperature difference (ΔT_m) occurs usually at night as sap flow is low or nil. A daily ΔT_m was used in this study so as to capture the daily dynamics of sap flow variations. The flow index (*K)* was then used to determine the sap velocity using

$$v = 0.119 \cdot K^{1.231} \qquad \text{(Equation 45)}$$

Where v is the sap velocity [cm/s] and *K* is the flow index. The hourly sap flux density was determined by:

$$J_v = v \cdot 3600 \qquad \text{(Equation 46)}$$

Where J_v is the sap flux density [$cm^3 / cm^2 / h$] and v is the sap velocity [cm/s]. Sap flow was then obtained by:

$$Q_s = J_v \cdot A_x \qquad \text{(Equation 47)}$$

Where Q_s is the sap flow which is equivalent to tree transpiration (T_t) [cm^3 / h], J_v is the sap flux density [$cm^3 / cm^2 / h$] and A_x is the xylem or sapwood area[cm^2]

The "Clearwater" correction (Clearwater et al., 1999) whose need arises when the Granier TDP probes are in contact with the bark or the hardwood was not necessary. The xylem or sapwood lengths were all greater than 2.5 cm (Table 4-4) and the bark was stripped off on installation of the TDP system.

Sap flow data for the 1st to the of 6th of September used was measured and calculated by Agbakpe, (2010).

4.14. SAP FLOW UP-SCALING

4.14.1. Projected Canopy Area (A_c)

The canopy area (A_c) is the up-scaling scalar that is better retrieved from remote sensing imagery compared to the other up-scaling scalars such as DBH (Lubczynski, 2009). Hence ground measurements related to the projected canopy area were done. The projected canopy area calculation assumed that the canopy follows the shape of a "perfect ellipse". The measured north-south length of canopy was taken as minor axis and the measured east-west length was taken as the major axis. The projected canopy area was estimated by:

$$A_c = \left(\frac{a}{2} \cdot \frac{b}{2} \right) \cdot \pi \qquad \text{(Equation 48)}$$

Where a [m] is the major axis, b [m] is the minor axis and π is equal to 3.14.

4.14.2. Sapwood or Xylem Area (A_x)

The xylem area is a central variable in the calculation of sap flow and in the up-scaling of sap flux density (Cermak and Nadezhdina, 1998; Lubczynski, 2009). As the xylem is responsible for the transportation of water and minerals in a plant the calculation of its area is vital. The xylem area was determined by first measuring the xylem length (A_l) using a Pressler borer at a height of ~ 1.3m (Grissino-Mayer, 2003). The xylem core was then dyed with methyl orange and the xylem length was then measured using a calliper (see appendix 1 for pictures). A total of 23 *Q. ilex* and 20 *Q. pyeranica* trees were xylem cored and the data is in appendix (3). The data was co-collected with Agbakpe (2010).

The calculation of the xylem area follows after the tree stem schematic presented in Figure 4-5.

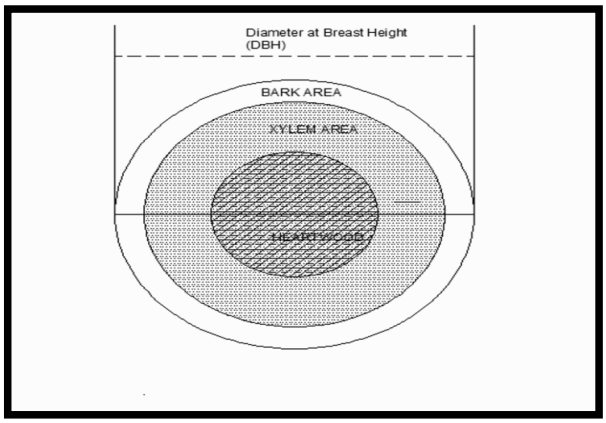

The sapwood or xylem area was estimated by subtracting the heartwood at the centre from the outlying bark area. The bark area was estimated based on an assumption of a species-specific average bark length (B_l). The cross-section bark length (B_l) assumed for the *Q. ilex* trees was 1 cm and 1.5 cm for the *Q. pyrenaica*. The bark length used for *Q. pyrenaica* was bigger than that of the *Q. ilex* because the *Q. pyrenaica* naturally has a bigger bark width.

Figure 4-5: Schematic of a tree stem

The formula derived, by definition, for estimating the xylem area is:

$$A_x = \underbrace{\left(\pi \cdot \left(\frac{DBH}{2} - B_l \right)^2 \right)}_{I} - \underbrace{\left(\pi \cdot \left(\frac{DBH}{2} - A_l - B_l \right)^2 \right)}_{II} \quad \text{(Equation 49)}$$

Where A_x is the xylem area [cm^2], DBH is the diameter at breast height [cm], B_l is the bark length [cm], A_l is the measured xylem length [cm] and π is equal to 3.14. Term I (one) represents the surface area of the heartwood and the xylem area. Term II (two) is the surface area the heartwood. The difference of term I and II resulted in the estimated xylem or sapwood area (A_x) [cm^2].

4.14.3. Tree Heights

Tree heights were measured using a PM 5 clinometer with range finder (Sunto). The measurement was made from a distance of 15 metres at eye level. The up-look height and the down-look heights were read off from the clinometer. To obtain the final tree height, when the one of the heights (up-look or down-look) was negative then two (absolute) values were added and when both measurements were positive they were subtracted. The subtraction was done because this implies that the eye level was below the base of the tree.

4.14.4. Diameter-at-breast height and height to first branching.

The diameter-at-breast height (DBH) was measured at a height of 1.3 metres above the ground. The diameter-at breast height was measured using a 100 cm calliper. In instances where the calliper was not big enough, the circumference was measured at ~1.3 metres. The DBH was then calculated from the circumference measurement. DBH was measured because it is a scalar also used sap flow up-scaling (Čermák et al., 2004). The height to first branching (H1B) was also measured. The height to first branching of the tree was measured from the ground level.

4.14.5. Sampling of Trees

The selection of trees that were sampled was generally guided by the following conditions:

- The need to obtain a high density of points within the fetch distance of the tower;
- The existence of some biometric data from research done in previous years.

The tree sampling focussed on areas that influenced the tower measurements but with no data available from previous studies. The areas that influenced the Tower measurements were determined by an analysis of a total of 3 593 wind direction records for the period 7 August 2009 to 2 September 2009. The analysis showed that the major source wind directions were in quadrant one (Q. I) and quadrant three (Q.III) shown in Figure 4-6. The North-East direction had a higher frequency but stronger wind speeds were observed in the South West and South-South West direction. On the basis of these dominant wind source directions the sampling of trees focussed on areas that correspond to Q. I and Q III and the West North West sector of Q. IV

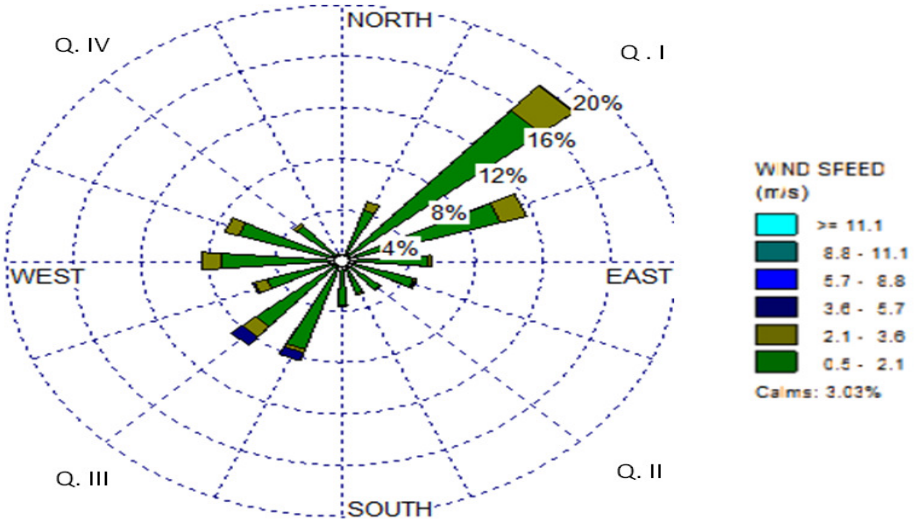

Figure 4-6: Analysis of Prevailing Wind Direction

Figure 4-7 shows the biometric data and the tree identification data used in this research. The points in red indicate the data that was collected during this research (n= 190 points).

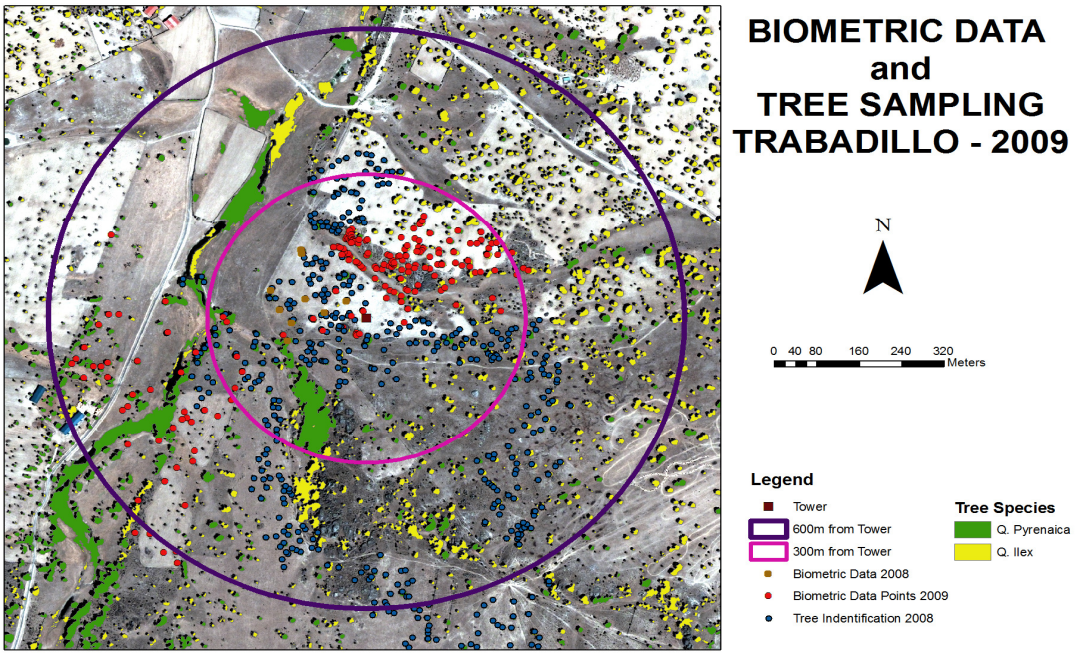

Figure 4-7: Map Biometric Data Points (Sampled trees)

The distribution of points in Figure 4-7 corresponds to Figure 4-6. These areas were also not sampled in previous studies (Ontiveros Enriquez, 2009). The difference with the 2008 data is that in 2009 all the data collected has biometric measurements, whereas in 2008 for most points (points in blue) the identification of tree species was done. In 2008, biometric measurements were done for the points in brown only.

In the field, a general guiding principle was to sample every third tree so to achieve a high density of biometric measurements. Hence a total of 190 trees were sampled.

4.15. BIOMETRIC DATA AND BIOMETRIC UPSCALING FUNCTIONS

The up-scaling approach applied in this research follows after the work of Kimani et al (2007), Chavarro-Rincon (2009) and Ontiveros Enriquez, (2009). The approach uses a scalar that can be effectively retrieved using remote sensing with the aid of object-oriented GIS classification packages. Such a scalar is the canopy area (Lubczynski, 2009). As in the work of Ontiveros Enriquez (2009), a biometric up-scaling function was defined by regression fitting between biometric variables. The variables that were assessed are: the height to first branching (H1B), the projected canopy area (A_c), the xylem or sapwood area (A_x) and the diameter at breast height (DBH)

4.16. REMOTE SENSING IMAGERY: QUICK BIRD IMAGE

A high resolution Quick Bird image (Digital Globe, USA) was used in this study. The Quick bird satellite has an orbital path of 450 km altitude and 98^0, sun-synchronous inclination. The multispectral image used has four spectral bands, namely: Blue (450-520nm), Green (520-600nm), Red (630-690nm) and the Near-Infrared (760-900nm). The spatial resolution is 2.4 metres at nadir.

Salinas (2010) retrieved canopies and classified the trees using an object-oriented methodology already used by Kimani (2005) for savannah ecosystems. Salinas (2010) used a Quick bird image and processed it using Definiens Developer (Definiens AG, Germany). The overall classification accuracy reported by Salinas (2010) is 80%. Since in transpiration mapping, the crown canopy size is critical and considering that the study area was relatively small, "spilt" canopies were corrected and a canopy size accuracy assessment was done based on the biometric data that was collected in the field. A regression analysis of the accuracy of the retrieved canopies was done.

4.17. FOOTPRINT DETERMINATION

The footprint model developed by Hsieh et al. (2000) (the footprint model here after is referred to as H2000) was chosen in this study because:

1. It is developed to work in an atmospheric surface layer (ASL) with thermally stratified flows.
2. The model is pragmatic, and hence it's use in research has continued to increase since it was first published, for example by Miller (2009), Detto et al. (2006) and Marcolla and Cescatti (2005).
3. The solution is validated against the data of Baldocchi and Rao (1995) and Marcolla and Cescatti (2005) showed that the solution works well for unstable conditions, which are times that this thesis focuses on.

The H2000 solution relates measurement height (z_m), surface roughness, the footprint, and atmospheric stability. The inputs used in the footprint solution are listed in Table 4-5.

Table 4-5: Inputs for the H2000 footprint model

Input	Symbol	Units	Comment
Friction Velocity	U^*	m s-1	Obtained from Eddy Covariance analysis

Mean Air Temperature	T	^{0}C	Eddy Covariance
Instrument Height	S	m	Measured
Momentum roughness height	Z_o	m	

Net radiation and sensible heat flux were also used in the computation script to determine the Monin-Obhukov Length, L [m], which was defined as:

$$L = \left(\frac{-\rho_a U_*^3}{kg\left(\frac{H}{C_p T}\right)} \right) \quad \text{(Equation 50)}$$

Where L is the Obhukov Length [m], k is the von Karman constant – 0.4, [-], g is the gravitational constant [m s^{-2}], H is the sensible heat flux, C_p is specific heat capacity of dry air at constant pressure, 1005 [J Kg^{-1} K^{-1}], U_* is the friction velocity [m s^{-1}] and T is the temperature [K].

The footprint solution was implemented using a Matlab script (Mathworks, USA) and the general implementation is as follows. Firstly canopy and roughness terms are determined using formulations of Brutsaert (1982):

$$z_0 = 0.1 * h \quad \text{(Equation 51)}$$

$$z_m = S_h - d_0 \quad \text{(Equation 52)}$$

Where z_0 is the roughness length [m] and h is the average tree height [m], z_m is the height above the zero plane displacement, d_o is the displacement height and S_h is the height of the measuring tower. A length scale (z_u) defined by Hsieh et al. (2000) was then calculated as:

$$z_u = z_m(\ln(z_m / z_o) - 1 + z_o / z_m) \quad \text{(Equation 53)}$$

Using similarity constants D and P that were defined by Hsieh et al. (2000) the cumulative source contribution with distance (F_c), the footprint (F_p), the peak distance (X_p) and the fetch to height ratio were then determined. The D and P constants used are in Table 4-6.

Table 4-6: D and P constants for H2000

D	P	Thermal Stratification
0.28	0.59	Unstable
0.97	1	Neutral and Near-neutral
2.44	1.33	Stable

The implementation in Matlab (MathWorks, USA) then determined the cumulative source contribution with distance (F_c) as:

$$Fc(x, z_m) = \exp\left(\frac{-1}{k^2 x} D z_u^P |L|^{1-P} \right) \quad \text{(Equation 54)}$$

The footprint was then determined as:

$$Fp(x, z_m) = \frac{1}{k^2 x^2} Dz_u^P |L|^{1-P} \cdot Fc \quad \text{(Equation 55)}$$

The location of the peak flux is obtained by:

$$X_p = \frac{Dz_u^p |L|^{1-P}}{2k^2} \quad \text{(Equation 56)}$$

The *Fc, Fp* and X_p (Equation 54) to (Equation 56) essentially define a 1-Dimensional footprint function. Fp is what is technically referred to as the crosswind integrated footprint 'function'. To enable a spatial analysis of the flux over the up-scaled sap flow map, the footprint function was then extended to 2-D using the formulation of Detto et al. (2006). By the 2-D expansion the footprint solution was thus able to determine the distribution function. Employing the reasonable assumption that vertical and crosswind direction diffusion process can be treated independently, the footprint function, Fp, was conceptually expanded to:

$$F_p(x, y, z_m) = D_Y(x, y) Fp(x, z_m) \quad \text{(Equation 57)}$$

Where $D_Y(x, y)$ is the x-y plane lateral spread [m] and $Fp(x, z_m)$ determined footprint function. Lateral spread was assumed to be Gaussian (Detto et al., 2006; Schmid, 1994) and hence $D_Y(x, y)$ was determined by:

$$D_y(x, y) = \frac{1}{\sqrt{2\pi\sigma_y}} e^{-\frac{1}{2}\left(\frac{y}{\sigma_y}\right)^2} \quad \text{(Equation 58)}$$

Where σ_y is related to the standard deviation of lateral fluctuations of wind, σ_v

This computation was discretized over a grid surface, defined in Matlab (MathWorks, USA), taking into account the pixel size of the Quick Bird image upon which the footprint was mapped. On the lateral spread axis, the point zero was taken as the eddy tower point. The determined footprint was then rotated into the wind direction at the specific time interval for which the footprint was determined.

4.18. FOOTPRINT MAPPING AND UP-SCALING

To map the footprint in GIS, the output footprint was discretized over a grid surface defined based on the Matlab (MathWorks, USA) output. The grid surface was defined rotated into the mean wind direction, by first changing the angle orientation in ArcGIS (ESRI, USA) to North azimuth and secondly defining the mean wind direction angle relative to the North. The output grids were then geo-referenced to the same reference system as the Quick bird image and the retrieved tree canopy maps.

In this study, 30 minute footprints were considered. The selection of the day for which the comparison with up-scaled sap flow was carried out, was based on the criteria of a clear sky and good sap flux data. The footprint determination could not be done over the whole day because at night time the Granier TDP approach used for sap flow measurement has problems resolving night-time fluxes. Doing a single footprint for a day was not done because that was almost similar to assuming the wind direction was the same through the day, which the data showed not to be the case. Given the time limitations of this study,

two footprints are analysed. In the future, the exercise can be repeated for a whole diurnal cycle. Thus the determination of the eddy flux footprint was done over 30 minutes at the time of peak net radiation (solar noon). The 30 minute time interval was also the averaging time of the eddy covariance data.

4.19. FOOTPRINT TRANSPIRATON

In most transpiration studies, the assessment of transpiration is based on an area average that is referred to as stand transpiration (Lubczynski, 2009). Without taking into account tree trunk water storage tree transpiration is equals sap flow, Q_s. As in this study eddy flux footprints are applied, the total footprint transpiration (equivalent to stand transpiration) was given by

(Equation 59)

$$T_t \frac{\sum_{i=1}^{n} Q_{s_i}}{A_{fp}}$$

Where T_t is the total transpiration over the footprint, and Q_s is the sapflow [m^3/h] and A_{fp} is the area of the footprint [m^2].The number n refers to the trees in the footprint. T_t over the footprint is thus expressed as depth to allow for comparison with eddy covariance.

5. THE SURFACE ENERGY BALANCE.

5.1. SURFACE ENERGY BALANCE FLUXES

This section presents results on the surface energy balance dynamics and responds to the following research questions:

- What are the diurnal dynamics of surface energy balance fluxes?
- What is the quality of the turbulent heat flux data?
- What is the degree of energy balance closure and what could have caused the lack of complete closure?

The net radiation budget analysis shows that up to 820 W m^2 of the sun's energy reached the study area. Over the study period the maximum shortwave incoming radiation was 914 W m^2. The shortwave radiation reflected by the surface reached a maximum of 238 W m^2 and a minimum of 0.5 W m^2. This flux minimum was observed at night-time. The minimum value of 0.5 W m^2 could be due to a calibration error as the expected minimum is zero. The diurnal variation of the net radiation budget components is presented in Figure 5-1 over DOY 253 – 256. The first two days show the energy dynamics or variation over days with clear skies and the other two, over partly cloudy days. It can be observed that the general trend and proportion of the fluxes do not change with cloudiness although the magnitude of the absolute values decreases as expected.

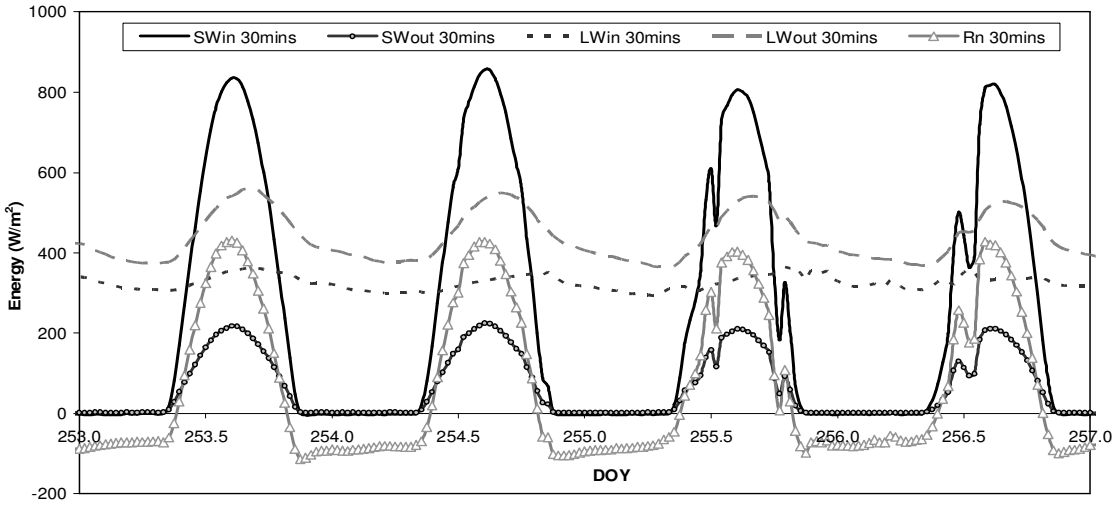

Figure 5-1: Net Radiation Budget Components for four example days.

Table 5-1 presents a mean, minimum and maximum of the radiation fluxes over the study period.

Table 5-1: Minimum, Maximum and Mean of Radiation Fluxes [W m-2]

	SW Incoming	SW Outgoing	LW Incoming	LW Outgoing	R_n
Average	233	63	317	421	66
Maximum	914	238	404	579	502
Minimum	-5	1	261	333	-113

Deducing from Table 5-1, average net radiation constituted about 28% of the average short wave incoming radiation with the rest being partitioned to the other net radiation budget terms. On the other hand the maximum net radiation constitutes about 55% of the observed maximum incoming energy from the sun.

The albedo of the surface ranged between 0.24-0.27. This value is comparable to albedo values published by Brutsaert (2005) of 0.20 – 0.35 for dry soils. The effective ground or kinetic temperature back calculated from long wave outgoing radiation averaged 22 °C and reached a maximum of 47 °C.

Soil heat flux was determined using two methods. Average soil heat flux from the plates at 1 cm depth and the method that accounts for heat storage in the first 10cm were used. This was done because soil heat flux is purposed to play a relatively bigger role in arid and semi-arid areas (Heusinkveld et al., 2004) compared to forests (Tanaka et al., 2008), crop fields and grass lands. Figure 5-2 compares the soil heat flux calculated with the two methods and shows that soil heat flux measured with soil heat flux plates at 1 cm depth underestimates the soil heat flux by ~ 21% compared to the soil heat flux with heat storage.

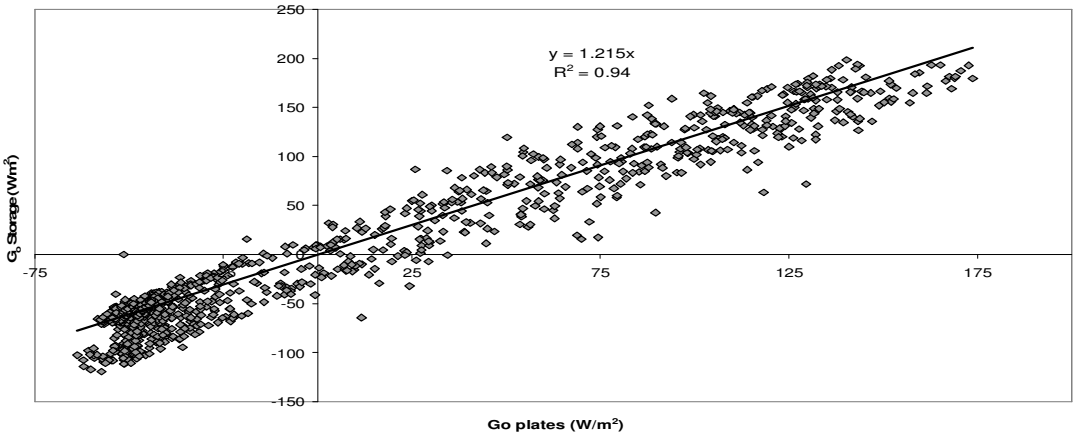

Figure 5-2: Soil heat flux measured with two heat flux plates at 1 cm depth (horizontal axis) versus soil heat flux calculated from the change in heat storage in the upper 10 cm of the soil plus soil heat flux measured at 10 cm depth (vertical axis).

The underestimation of the soil heat flux occurred mainly at night and at solar noon as shown in Figure 5-3. In Figure 5-3 soil heat flux measured with soil heat flux plates only underestimates the flux at peak noon and after sunset. In Figure 5-3, the black circles emphasize the time period of soil heat flux underestimation.

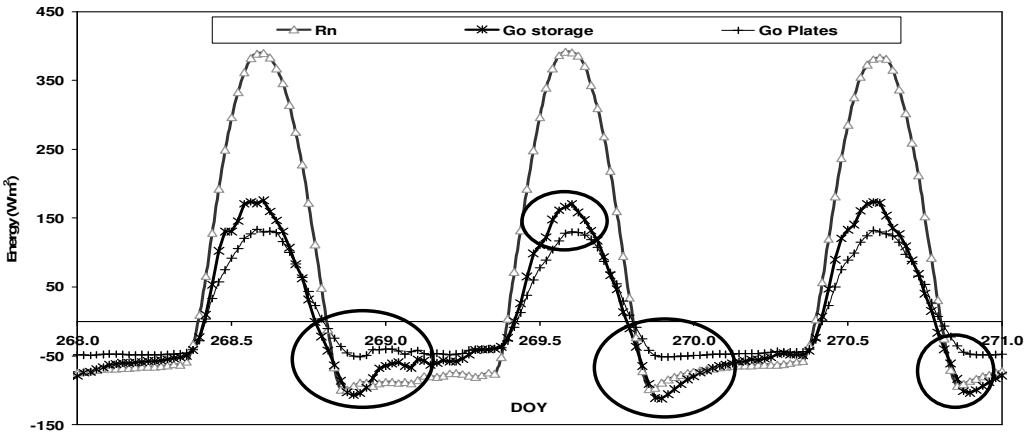

Figure 5-3: Underestimation of Soil Heat Flux by soil heat flux plates over time.

Over night time it is also noted that the soil heat flux (with heat storage) is strongly coupled with net radiation over the time period between sunset and sunrise. This is according to expectation, as soil heat flux responds to and compensates the radiative surface cooling (outgoing longwave radiation). The turbulent heat fluxes (latent and sensible heat flux) were negligible during the night.

The soil heat flux underestimation at night can be explained by the fact that the flux at 1 cm below the surface is not representative of the soil heat flux at the surface. The second method, which takes into account heat storage in the upper 10 centimetres of the soil, does not have this problem.

The tendency for soil heat flux plates to underestimate the flux has been observed by other researchers who have intensively studied soil heat flux measurement issues. Ochsner et al.(2006) from their study observed an under/over-estimation of fluxes by between 18 and 66% relative to the three needle pin method. Sauer et al. (2003) using laboratory tests with a known heat flux also observed an underestimation of between 2 – 38% in dry soils. The error associated with underestimation is associated to the design of plate in relation to heat flow dynamics that results in flow divergence due to thermal contact resistance. This issue was extensively discussed by Philip (1961), who even suggests a correction equation for the soil heat flux measurement. This is however not applied in this work, as there seems to be no consensus about the effectiveness of the method (Sauer et al., 2003; Weber, 2006).

The energy balance components measured over part of the study period are shown in Figure 5-4. The peak fluxes occurred at around solar noon i.e. around 14:20 – 14:30 local time as expected. In Figure 5-4, it can be noted that on DOY 253 and 254 there were clear skies and on DOY 255 and 256 it was cloudy. The effect of cloudiness is also depicted in the jagged soil heat flux trend. Sensible heat flux and soil heat flux alternate as the highest fluxes after net radiation during the whole the study period.

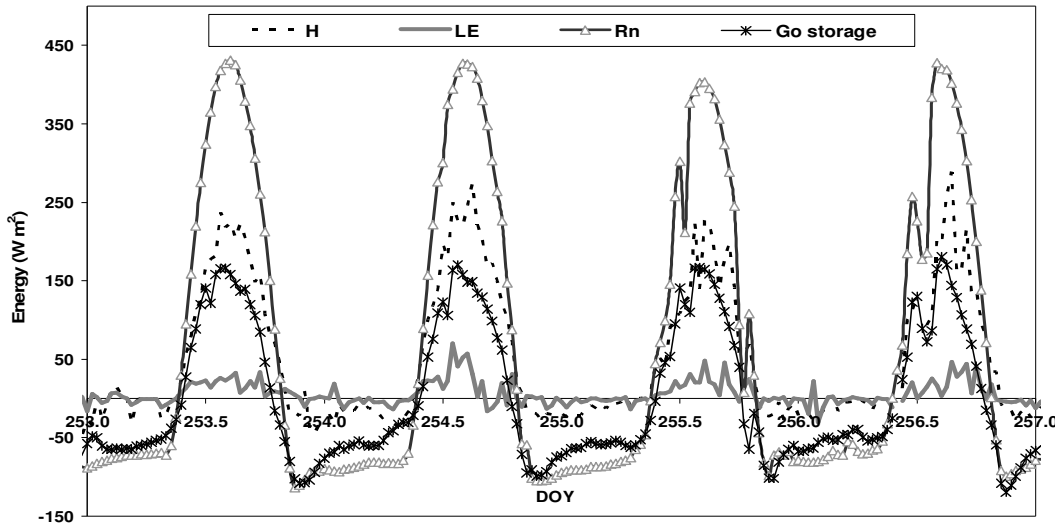

Figure 5-4: Surface Energy Balance Fluxes for DOY 253 – 257.

Figure 5-4 shows that sensible heat flux is consistently the dominant turbulent heat flux. A simple Bowen ratio H/λE shows on average throughout the study period sensible heat flux (H) is 43.7 times larger than the measured latent heat flux (λE). A low latent heat flux is not only visible on the days presented in Figure 5-4, but occurred throughout the study period. The high sensible heat flux and low latent heat flux confirms that evaporative cooling is limited.

5.1.1. What is the diurnal course of the energy balance component fluxes?

The diurnal course of the energy balance fluxes is presented in Figure 5-5 for a typical clear day and Figure 5-6 for a cloudy day. It can be observed that from morning until solar noon, soil heat flux and sensible heat follow a nearly similar trend and the absolute value of the flux is almost equal. Both soil heat flux and sensible heat flux show a strong dependence on or a relationship with net radiation. An analysis of this dependence or relationship is shown by the regression statistics in Table 5-2.

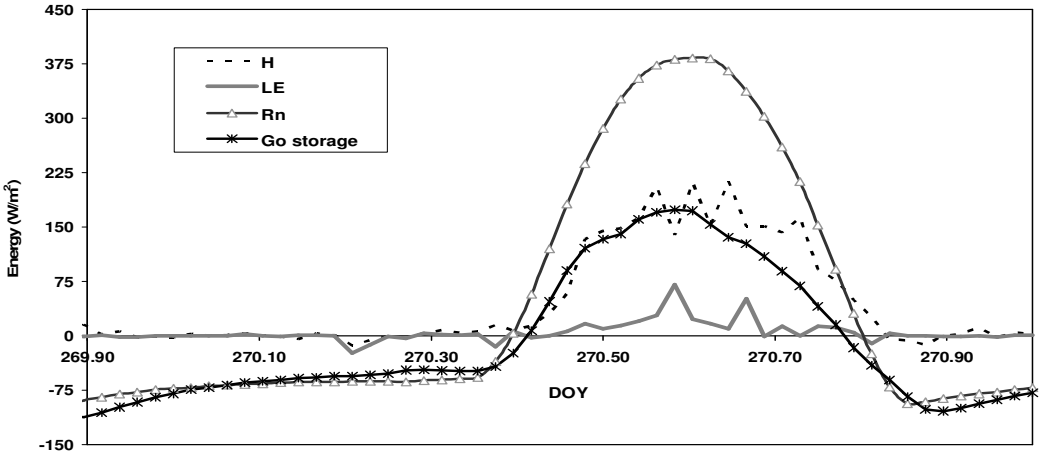

Figure 5-5: Diurnal Course of the Energy Balance Fluxes - DOY 269

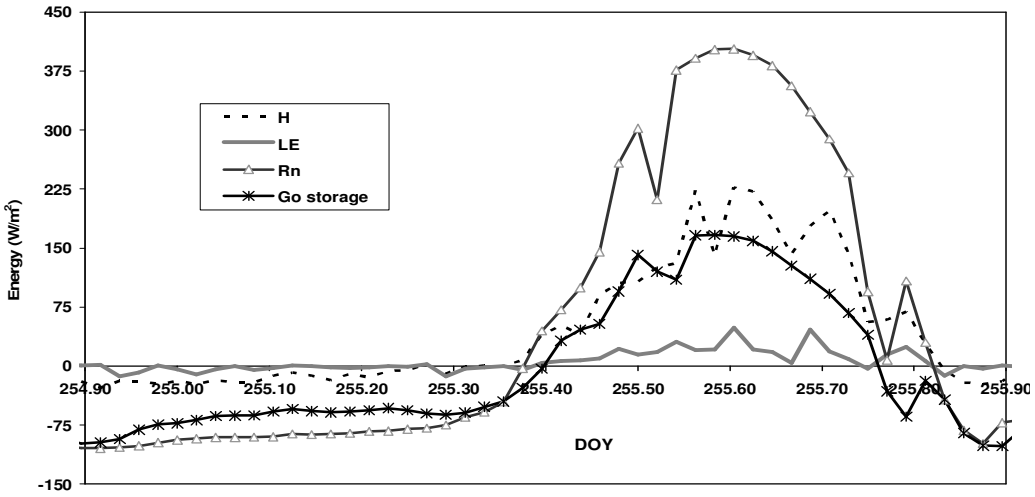

Figure 5-6: Diurnal Course of the Energy Balance Fluxes - DOY 255

To understand the diurnal dynamics the statistical relationships of the net radiation vs. latent, sensible heat flux were also analysed. Net radiation is the main forcing factor of the surface energy balance and hence the statistical relationships help infer the intensity of the diurnal coupling of fluxes. The regression statistics are presented in Table 5-2

Table 5-2: Statistical Regression(s) of Rn with Go storage, H & LE

	Net Radiation (R_n) vs.		
	Soil Heat Flux	Sensible Heat	Latent Heat Flux
Regression (with non zero intercept)	y = 0.45x - 30.12	y= 0.4626x+24.75	y = 0.0487x +2.59
R^2 (with non zero intercept)	0.93	0.93	0.389
Regression (with zero intercept)	y = 0.39977x	y = 0.5066x	y = 0.053x
R^2 (with zero intercept)	0.82	0.86	0.36

It can be noted from Table 5-2 that there is positive relationship between net radiation vs. soil heat flux and sensible heat flux. The higher slope and R^2 for sensible heat flux when the intercept is set as zero is reflective of the daytime coupling of H with R_n evident in Figure 5-5 and Figure 5-6. The relationship of $H = 0.51\ R_n$ is surprisingly in line with work of Tanaka et al. (2008) who also found a relation of $H = 0.51\ R_n$ over a larch forest in Siberia. This is surprising because this relationship is expected to be climate dependant. This suggests that there are other processes at play that influence such relationships.

The relationships of net radiation with soil heat flux and sensible heat flux are marked an almost similar slope in absolute value terms (non-zero intercept) and both have an R^2 of 0.93. The differences however arise after forcing the intercept through zero. Sensible heat flux stands out with a much stronger relationship to net radiation with a slope of 0.5 and an R^2 of 0.86. The diurnal energy balance dynamics are thus strongly coupled between net radiation and sensible heat flux followed by soil heat flux and then finally latent heat flux.

5.1.2. What is quality of turbulent heat flux data?

Since evapotranspiration is determined from turbulent heat flux data there is need to understand how good the turbulent heat flux data is. The derived values of evapotranspiration are used to draw conclusions of evapotranspiration and tree transpiration dynamics and hence such an assessment is vital. Göckede et al.(2004) in assessing complex FLUXNET sites (Baldocchi et al., 2001) applied an assessment scheme that combines the stationarity and the integral turbulence test (Foken and Wichura, 1996) test to assess flux data. A similar scheme is therefore applied. The quality assessment scheme can be divided into four groups. Group I consists of quality grades 1- 3 and the group is reflective of good data that can be used to even develop ABL parameterisations. Group II consists of quality grades 4- 6, which is indicative of reasonably good data that is suitable for flux for monitoring programmes. Group III consists of quality grades 7 and 8 for which the data is for orientation purposes. Group IV is made up of grade 9 data, which is bad data (Foken et al., 2004; Foken and Wichura, 1996).

Figure 5-7 presents the quality assessment results for sensible heat flux. It can be observed from Figure 5-7 that ~ 85% of the data (n=1 152 – 30 minute averages) falls into grades 1-3. 12.65% of the data falls into grade 4-6 and cumulatively total for Group I and II is 97.8%. No data was classified as being bad.

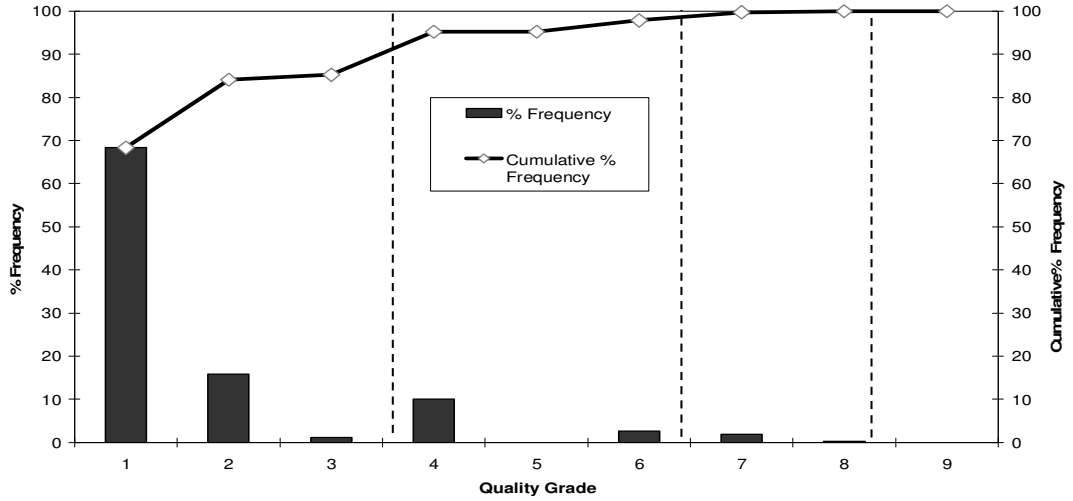

Figure 5-7: Sensible Heat Flux Data Quality Assessment Results

In Figure 5-8, the results for the latent heat flux quality assessment are presented (n=1 152 – 30 minutes averages). 67.8% of the data was classified as grade 1-3 data. 21.6% of the data was in Group II. Group I and II cumulatively consisted of 89.4% of all the data. 0.3% of the data of the data was classified as bad.

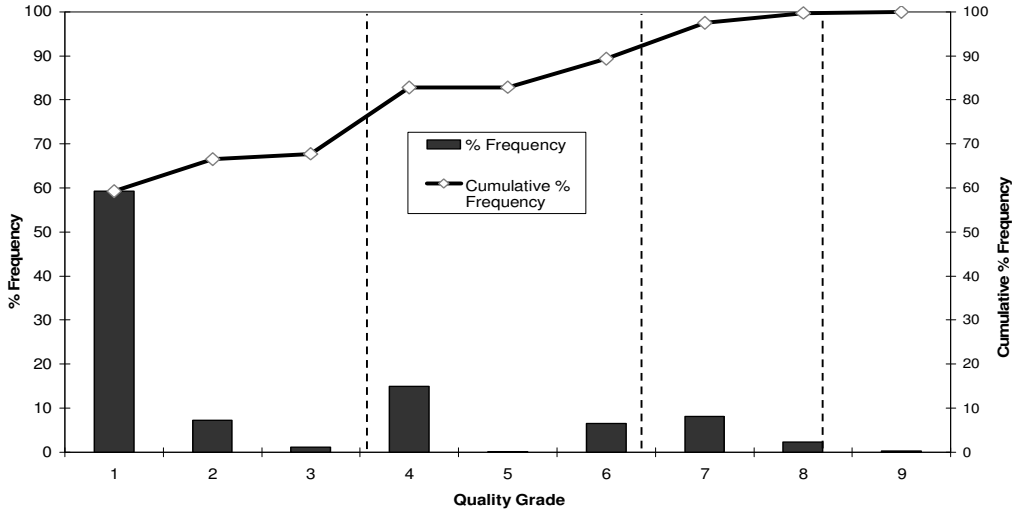

Figure 5-8: Latent Heat Flux Data Quality Assessment Results.

The differences in the quality of the turbulent heat data can be explained by the fact that the measuring approaches are slightly different. Sensible heat flux is essentially measured by a single instrument (CSAT-3), with temperature being determined from the speed of sound. Latent heat flux is determined by two instruments CSAT-3 (Campbell Scientific, USA) and a LICOR 7500 (Licor Inc, USA) that had a spatial separation of approximately 11 centimetres. In as much cross-correlations are done in the processing but a minor effect of the spatial separation results in latent heat flux data having slightly lower percentage statistics. This is compounded on already known uncertainty of turbulent heat flux measurement between 5 – 10% and 10-20 W m^2 (Foken et al., 2009). However, overall the quality of the data is good and acceptable.

5.1.3. What is the degree of energy balance closure and what could have caused the lack of complete closure?

A surface energy closure assessment assesses the conservation of energy principle. The independently measured energy balance components were analysed to verify whether the available energy (R_n-G_o) matches the sum of the turbulent heat fluxes ($H+\lambda E$). The energy balance closure analysis provides an in-depth understanding of the surface energy balance system and also evaluates the quality of the turbulent heat flux data (Barr et al., 2006; Wilson et al., 2002)

Having observed that the soil heat flux was underestimated by the use of soil flux plates alone (Figure 5-3), the energy balance closure analysis was done using the 30 minute data with soil heat flux that includes heat storage (G_o storage). Figure 5-9 shows the energy balance closure analysis done using the regression method (Foken, 2008a; Wilson et al., 2002).

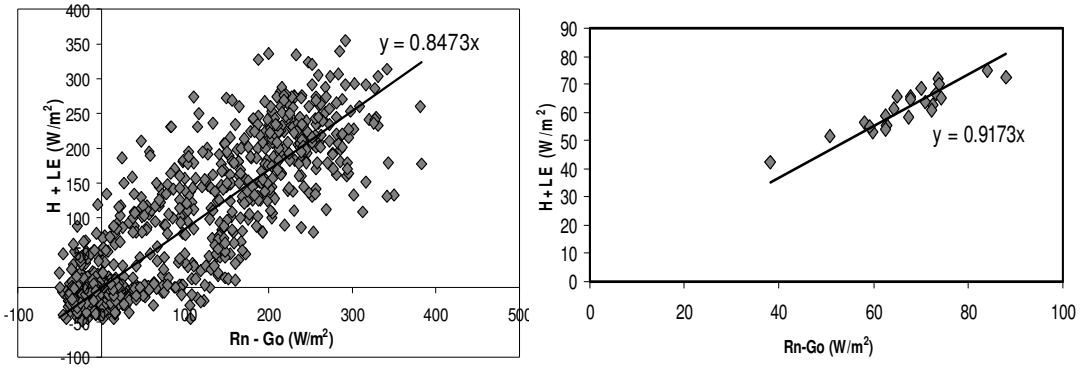

Figure 5-9: Energy Balance Closure Analysis. a) (Left) 30 minute Energy Balance Closure Analysis. b) (right) Daily Energy Balance Closure Analysis. On the x-axis is available energy (R_n - G_0 storage) and on the y-axis if the sum of the turbulent heat fluxes (H+LE).

Figure 5-9 a) shows that using 30 minute data, the energy balance closure is 85%. Figure 5-9 b) which is based on daily average data shows the balance closure is 92%. In comparison with other published energy balance closure results, these are relatively high closure percentages. The energy balance closure is expected to range between 70 – 90% (Foken, 2008a; Twine et al., 2000; Wilson et al., 2002). In terms of the expected range of closure, the energy balance closure of 85% and 92% are at and above the upper limit of expected closure (90%).

Taking the energy balance closure test as an objective measure of data quality (Barr et al., 2006), the data collected is good. This finding is vital for eventual computations of evapotranspiration. The difference of 85 and 92% can be explained by the fact that in averaging to daily values, the errors associated with 30 minute values are averaged out or minimised.

The high closure percentage could be dependant on having accounted for soil heat storage. Without accounting for soil heat storage, the soil heat flux could be 21% lower, and this could have led to a lower energy balance closure. Over bare soil and in dry areas, such as in WLE, soil heat flux can be as high as 30-50% of R_n and this strongly influences the degree of energy balance closure (Heusinkveld et al., 2004). The observation of soil heat flux of up to 40-50% of R_n in this research is thus consistent with other research work.

It is worth noting that the energy balance closure results are based on the simplified definition of the energy balance ($R_n = \lambda E + H + G_0$). The other heat storage terms are not included. Recently, researchers are considering the other energy storage terms in a bid to close the energy balance. Other heat storage terms that have been shown to lead to a high closure percentage are: the storage flux and advection terms between the sensor measuring height and the land surface (Heusinkveld et al., 2004), the photosynthesis process (Jacobs et al., 2008) and the vegetation or biomass storage terms (Twine et al., 2000). None of these terms are considered in this study but still a high energy balance closure is attained.

Figure 5-10 presents the energy budget residuals (EB Residual = $R_n - (\lambda E + H + G_0)$ on a day with clear skies (left) and a day that is cloudy (right).

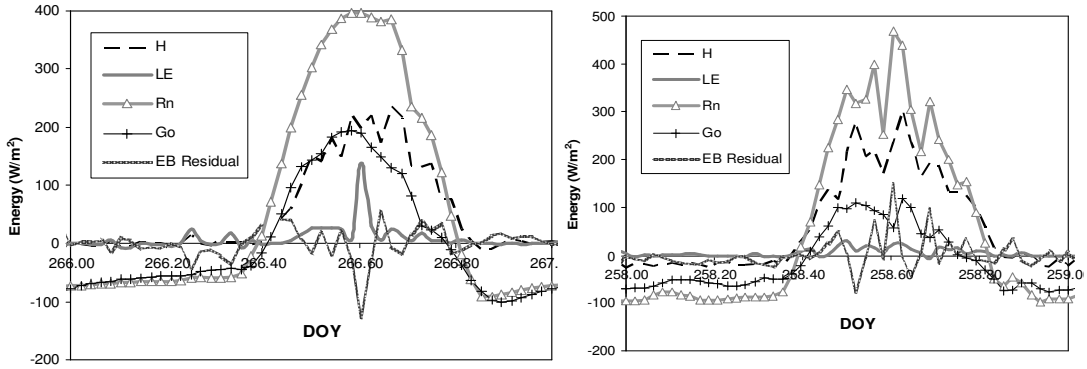

Figure 5-10: Energy Balance Residuals on a) (left) on a clear skies day, DOY 266 and b) (right) on a cloudy day, DOY 258.

It can be observed that on day with clear skies, the energy budget residuals follow a distinct trend, associated with continuous solar insolation over the land surface. As such the peak residual occurs at solar noon. On a day that is cloudy, the energy balance residuals do not have a distinctive pattern. This is associated with the effect of cloud cover. The distinctive trend on DOY 266, would suggest that the errors are more systematic. Therefore the lack of complete energy balance closure could thus be due to systematic errors. Being systematic, the lack of closure could, in part, be attributed to instrument error. The effect of systematic errors is well documented in research papers as a possible cause for the lack of complete closure (Foken, 2008a; Wilson et al., 2002). A more statistically rigorous approach would be to test for normality of the residuals. Testing for normality would show if the energy balance residuals follow a normal distribution, which could be indicative of systematic error. However, such a test would fail to show that the residuals are normally distributed because the systematic errors would be masked out by the effect of clouds as shown by the trend of energy balance residuals on DOY 258 in Figure 5-10. Hence the test is not applied.

An analysis of the energy balance ratio shows that another possible reason for the lack of closure is the effect of turbulent mixing related to thermal stratification. Eddy covariance being a turbulence based approach naturally demands that the atmosphere be turbulent enough. Figure 5-11 presents the relationship between friction velocity (U_*) and the Energy Balance Ratio (EBR) (also termed the Closure Fraction) according to thermal stratification. The EBR is defined as $((H + \lambda E)/(R_n\text{-}G_o))$. In the case of perfect closure, the EBR should be equal to one

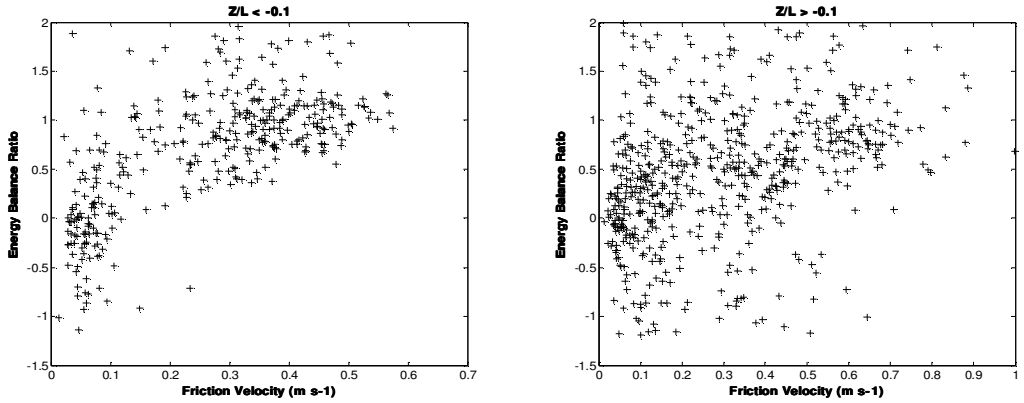

Figure 5-11: Effect of turbulent mixing on energy balance closure for thermal stratification conditions *z/L* <-0.1 (left) and *z/L* >0.1

In Figure 5-11, it can be observed that the scatter in the two plots is different. Under thermal instability ($z/L < -0.1$) the scatter follows a more distinctive shape ($R^2 = 0.46$). Negative EBR values occur largely over periods with U_* of less than 0.2 m s^{-1}. On the hand, during near neutral and stable conditions $z/L > -0.1$) there is no distinctive pattern (R^2=0.12). Under conditions of thermal instability ($z/L < -0.1$) there is more scatter around the ratio of perfect closure, one (1). Under $z/L > -0.1$ conditions the scatter does not cluster around 1. Hence better closure occurred under $z/L < -0.1$ conditions than $z/L > -0.1$.

A friction velocity of < 0.35 or 0.3 m s^{-1} has been shown in literature to be associated with the lack of energy balance closure. In some studies data with $U_* < 0.35$ or 0.3 m s^{-1} has been rejected (Herbst et al., 2002). The reason being that it is classified as being weak turbulence (Barr et al., 2006; Foken, 2008a; Herbst et al., 2002; Wilson et al., 2002). A careful examination of Figure 5-11, shows the concentration of points less than the critical threshold of 0.35 or 0.3 m s^{-1} is higher for the period $z/L > -0.1$. It is thus plausible to argue that the overall lack of closure could be associated with low turbulent mixing.

Another possible reason for the lack of closure, as shown earlier, is the effect of spatial separation of the water vapour concentration instrument and the sonic anemometer. This is also called a filtering effect (Wilson et al., 2002). However since an open-path sensor was used, low pass filtering effects associated with tube attenuation or water vapour effects within the tube cannot explain the lack of energy balance closure over the study period.

Statistical uncertainties that arise from eddy covariance sampling errors are also another possible factor. Finkelstein and Sims (2001) argue that there are uncertainties of between 10 – 20 % when using 30 minute interval eddy covariance data. This seems substantiated in this research by the fact that the energy balance closure for 30 minute interval data is 86% and for daily averaged data is 92%.

6. EVAPOTRANSPIRATION, TRANSPIRATION AND BIOMETRIC UP-SCALING

This section starts by presenting results on the environmental conditions for orientation purposes. The research question, what are the evapotranspiration and transpiration flux quantities is then addressed. Finally, the biometric up-scaling function developed is presented.

6.1. ENVIRONMENTAL CONDITIONS

In an up-scaling study it is important to understand the environment in which the up-scaling is being done. This section thus defines soil moisture and atmospheric conditions that prevailed during the study period.

6.1.1. Soil Moisture Trends

Soil moisture plays a key role in evapotranspiration processes. Figure 6-1 presents profile measurements of soil moisture (percentage) at four depths, viz; 25cm, 50, 75 and ~100cm. This profile was located ~ 8.10 meters away from the nearest *Q. ilex*. This profile was chosen because it was less affected by tree root water uptake when compared to other profiles located 3.1, 1.65 and 1 m away from the same *Q. ilex* tree.

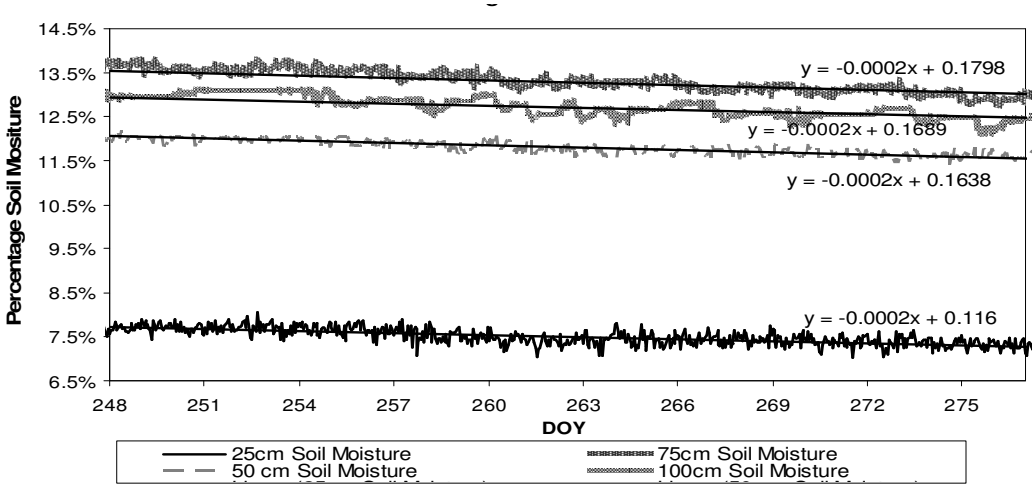

Figure 6-1: Soil Moisture Profile Measurements for Trabadillo (DOY 248 -277, 2009)

It can be noted from Figure 6-1 that the lowest soil moisture content was recorded nearer to the soil surface (25cm). The average percentage soil moisture at 25 cm is 7.63 %. The largest average soil

moisture is at 75cm depth. Table 6-1 presents the descriptive statistics (average, maximum and minimum) of the soil moisture measurements with depth.

Table 6-1: Statistics of Soil Moisture at four depths (25, 50, 75 and ~ 100cm)

Soil Depth	Average		Maximum		Minimum	
	(m^3/m^3)	%	(m^3/m^3)	%	(m^3/m^3)	%
25cm	0.076	7.63%	0.083	8.30%	0.070	7.00%
50cm	0.119	11.93%	0.125	12.50%	0.114	11.40%
75cm	0.134	13.41%	0.138	13.82%	0.127	12.71%
~ 100cm	0.128	12.83%	0.132	13.21%	0.121	12.11%

Regression analysis of the soil moisture trends presented in Figure 6-1 reveals that all the profile depth measurements showed a decreasing soil moisture trend. The regression slope co-efficient for all depths is -0.0002. The negative trend is typical of the summer dry season in the study area and water-limited environments in general (Hernández-Santana et al., 2009; Lubczynski and Gurwin, 2005)

6.1.2. Meteorological Conditions

Relative humidity defines the degree of moisture in air as a ratio of the water vapour density to the saturation density (of vapour). The relative humidity at the study site before, during and after the study period is presented in Figure 6-2.

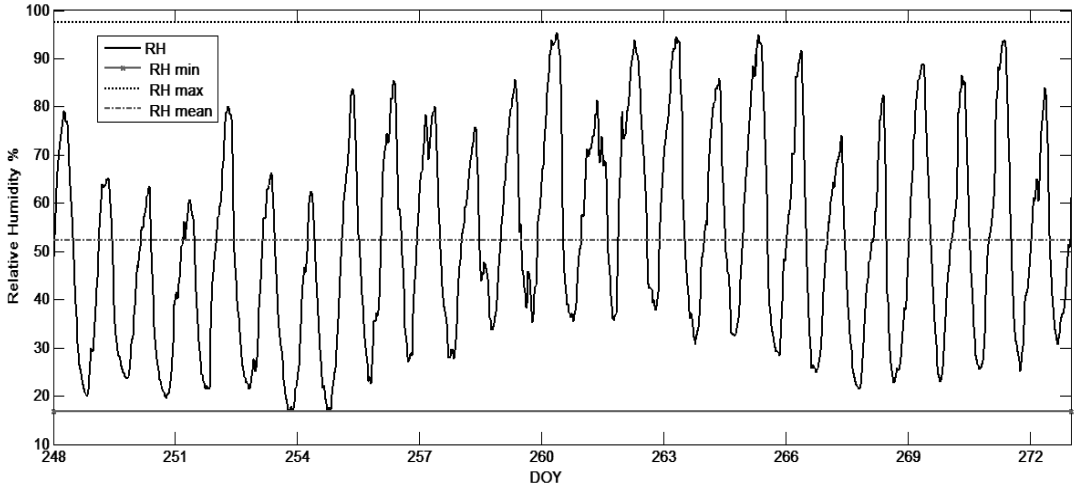

Figure 6-2: Relative Humidity measured at Trabadillo - 2009

Shown in Figure 6-2 is also the minimum relative humidity (RH) of 16.8 percent, a mean relative humidity (RH) of 52.3% and a maximum RH of 97.5%.

Temperature plays a central role in evapotranspiration and in the surface energy balance. The temperature dynamics over the study period are shown in Figure 6-3. The ground temperature was back-calculated from outgoing long wave radiation (Kipp & Zonen, 2002) using a bare soil emissivity value from Brutsaert (2005) of 0.97. In Figure 6-3, it can be observed that the period DOY 247 – 259 had higher peak ground temperatures, which decrease from DOY253.

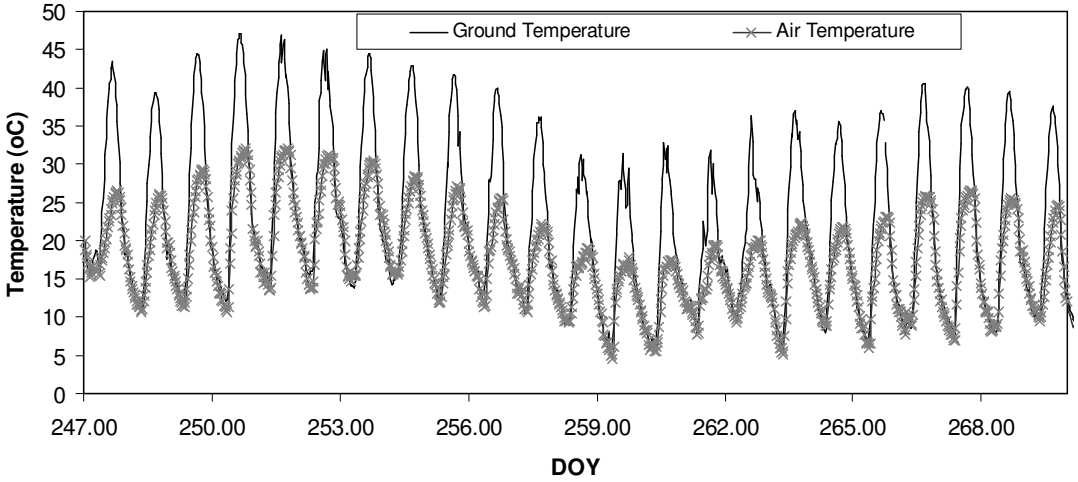

Figure 6-3: Temperature variation over the study period, Trabadillo - 2009

The average, maximum and minimum temperatures are presented in Table 6-2. Also shown is the temperature gradient, calculated as the difference between air temperature and ground temperature.

Table 6-2: Average, Maximum and Minimum Temperatures, Trabadillo - 2009

Temperature	Average °C	Maximum °C	Minimum °C
Ground (Kinetic)	22.1	47	5.89
Air	17.6	32.1	4.61
ΔT (air –ground)	-4.70	-18.7	2.68

The temperature differences shown in Figure 6-3 and Table 6-2 are related to the high sensible heat flux measurement already observed in the section on the surface energy balance system. A negative temperature difference is indicative of an upward sensible heat flux.

Water exchange processes in the land-atmosphere continuum also depend on the degree of water vapour saturation and deficit. The saturation and actual vapour pressure over the study period are shown in Figure 6-4, the vapour pressure deficit is shown in the same figure.

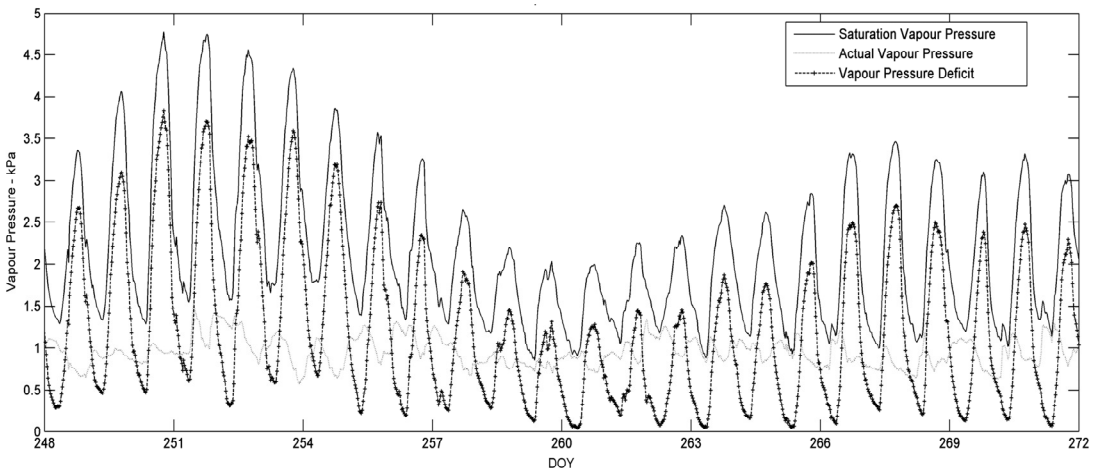

Figure 6-4: Trend of Vapour Pressure (Saturation, Actual and Deficit) over the study period, Trabadillo 2009

A peak saturation vapour pressure of up to 4.5 kPa was recorded over DOY 250 – 254 and the lowest peak saturation vapour pressure was observed over the period DOY 260 – 263. The actual vapour pressure does not vary significantly over the study period.

6.2. EVAPORATIVE FLUXES

This section addresses the research question on the quantitative determination of the evapotranspiration and tree transpiration fluxes.

6.2.1. Eddy Covariance Evapotranspiration

Eddy covariance evapotranspiration is technically a lumped flux of bare soil evaporation and transpiration. Though the eddy covariance tower was mounted over a long time, the data presented here relates to the time period when sap flux data is available. This is the month of September, which is one of the driest months of the Mediterranean summer (David et al., 2007; Lubczynski and Gurwin, 2005; Santana, 2008). This time period is characterised by slightly declining soil moisture trend as shown in Figure 6-1. The declining soil moisture trends are characterised by a negative regression slope of -0.0002. In such conditions Figure 6-5, shows the measured eddy covariance evapotranspiration over the period DOY 247 – 270.

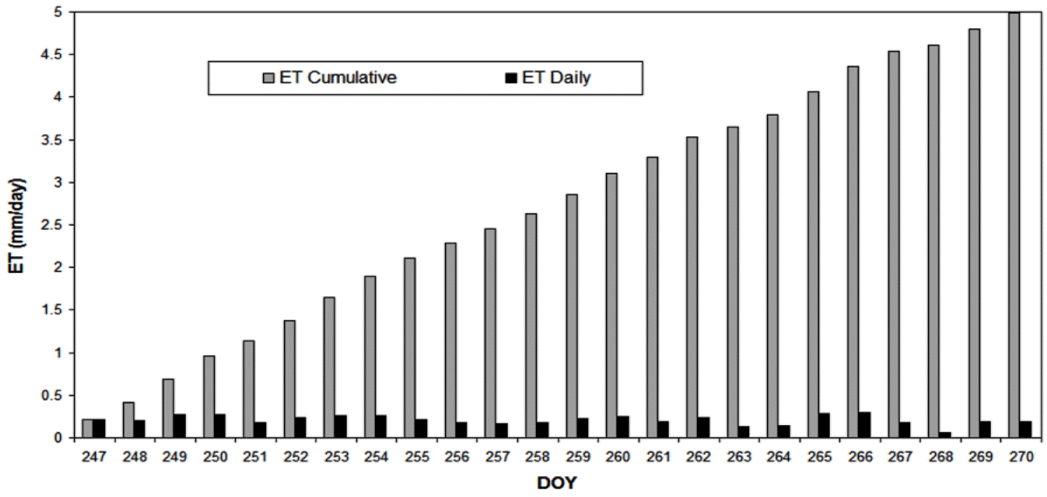

Figure 6-5: Daily and Cumulative Evapotranspiration (Eddy Covariance)

Figure 6-5 shows that daily evapotranspiration is low. The measured average daily evapotranspiration for the time period shown in Figure 6-5 is 0.21 mm d^{-1}. The minimum and maximum daily evapotranspiration is 0.06 and 0.29 mm d^{-1} respectively. The cumulative total evapotranspiration over the days shown in Figure 6-5 is 5 mm.

The diurnal dynamics of eddy covariance evapotranspiration are shown in Figure 6-6

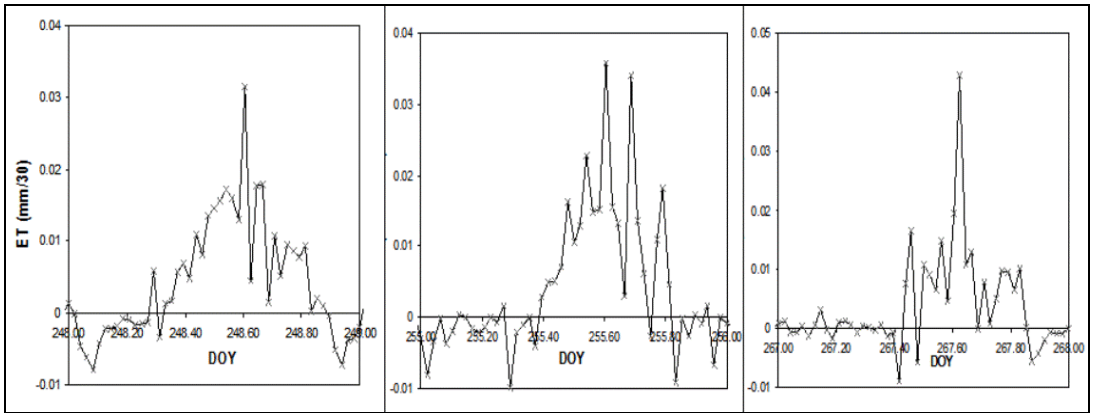

Figure 6-6: Diurnal Dynamics of Evapotranspiration - Trabadillo 2009.

In Figure 6-6, eddy covariance evapotranspiration is shown for tree days representing the beginning, the middle and the end of the study period. The days are: DOY 248, 255 and 267. Over the days with clear skies (248 and 267) the diurnal nature of evapotranspiration (*ET*) is characterised by a single distinct peak in the loss flux at solar noon. The inverse is true for DOY 255.

The peak fluxes of evapotranspiration occur at around solar noon, thereby suggesting the existence of significant coupling between R_n and *ET*. Theoretically also, strong coupling between soil moisture and ET is expected. To investigate this coupling daily soil moisture in the upper profile depth (25cm) was analysed. Figure 6-7, presents the trends of daily soil moisture and ET over the study period.

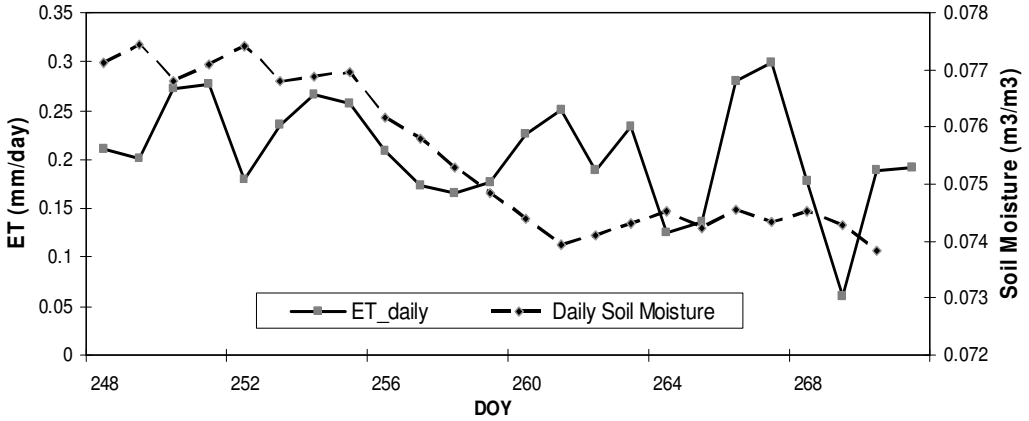

Figure 6-7: Soil Moisture and Evapotranspiration - Trabadillo 2009

The ET trend in Figure 6-7 does not show a relationship with the soil moisture measured at 25 cm depth. The R^2 value is 0.08. Around DOY 258-260 a significant decoupling effect is observed. Soil moisture decreases from about 7.7% to about 7.4% and yet the trend in the ET does not respond to this decrease in soil moisture. In actual fact, the highest peak in the ET flux of ~ 0.3 mm d^{-1} is observed around DOY 268. This is after the decrease in soil moisture over DOY 258-260.

This decoupling effect, the R^2 value of 0.08 and the general trend in Figure 6-7 suggests that the contribution of bare soil evaporation to the total ET flux is not major.

6.3. SAP FLUX DENSITY AND SAP FLOW

Sap flux density defines the volume mass flow in a tree and sap flow is the integrated sap flux density over an area. Sap flow thus defines the total amount of flow over a given area (Lemeur et al., 2009) thus it has more hydrologic relevance.

The calculated sap flux density for the two *Quercus* species over the study period is shown in Figure 6-8. The sap flux density of *Q. ilex* was observed higher than that of *Q. pyrenaica.* The average sap flux density observed over the period DOY 251 – 264 is 4.15 $cm^3/cm^2/hr$ for *Q. ilex* and 2.3 $cm^3/cm^2/hr$ for *Q. pyrenaica.*

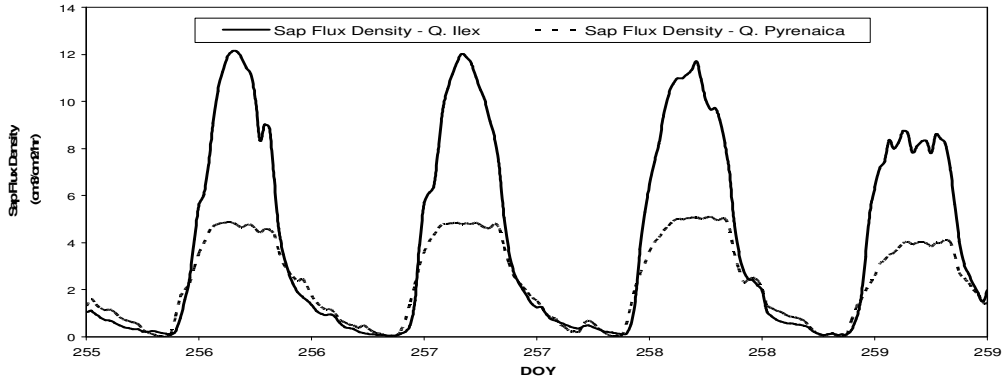

Figure 6-8: Sap Flux Density for *Q. ilex* and *Q. pyrenaica* - Trabadillo, 2009

The descriptive central tendency statistics for sap flux density and sap flow are presented in Table 6-3. However, the other data collected by Agbakpe (2010), shows *Q. pyrenaica* sap flux density of up to 6-8 $cm^3/cm^2/hr$ and this is integrated in the footprint analysis.

Table 6-3: Mean, Maximum and Minimum Sap Flux Density and Sap Flow for Q. Ilex and Q. Pyrenaica.

Statistic	Q. ilex		Q. pyrenaica	
	Sap Flux density $cm^3/cm^2/hr$	Sap flow l/hr	Sap Flux density $cm^3/cm^2/hr$	Sap flow l/hr
Mean	4.15	2.77	2.30	0.40
Maximum	13.03	9.09	5.59	0.007
Minimum	0.05	0.00	0.0037	0.98

The mean sap flow is 2.77 l/hr and 0.40 l/hr for *Q. ilex* and *Q. pyrenaica* respectively. Sap flow (Q_s) is assumed to be equal to tree transpiration (T_t) if tree water storage is not considered (Lubczynski, 2009). Therefore the maximum transpiration rate for *Q. ilex* was 9.09 l/day and 5.59 l/hr for *Q. pyrenaica* species.

For up-scaling and comparison of fluxes, it is important to establish to which energy related variable sap flow is better related with. The diurnal relationship of sap flow to net radiation and available energy was therefore assessed. Net radiation and available energy were chosen based on largely based on literature evidence (David et al., 2004; Hernández-Santana et al., 2009). The assessment of the up-scaled sap flux and the measured eddy covariance ET have to be done at a time when the response of both fluxes to an environmental forcing factor is nearly the same or not 'lagged'. The analysis was done over days with clear skies and DOY 253 and 254 as shown in Figure 6-9 and Figure 6-10

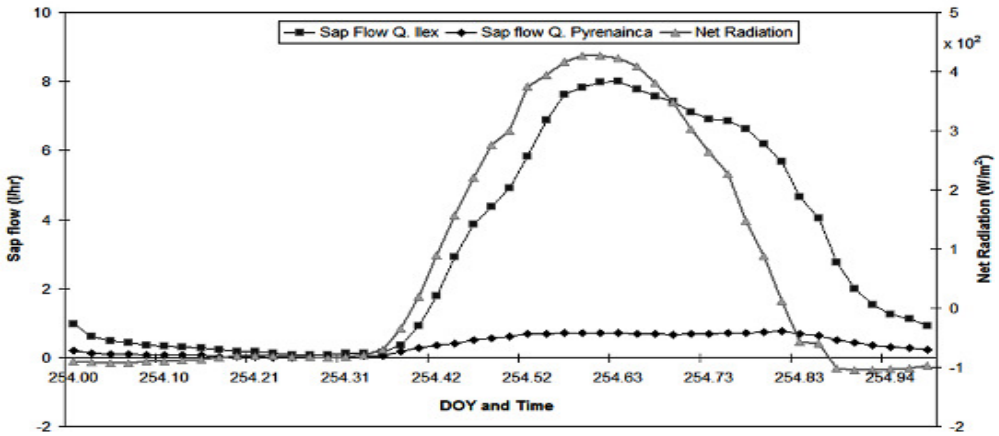

Figure 6-9: Response of Q. Ilex and Pyrenaica Sap flow (l/hr) to Net Radiation

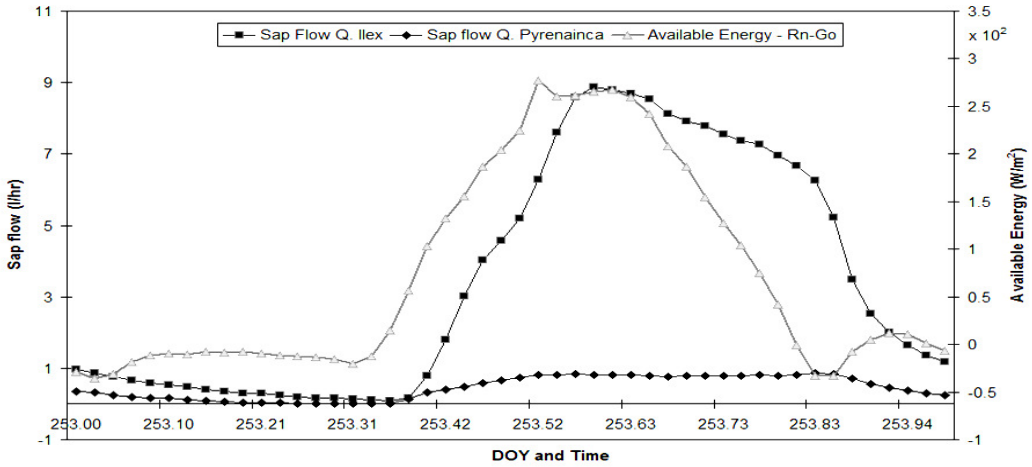

Figure 6-10: Response of Q. Ilex and Pyrenaica Sap flow (l/hr) to the available energy (Rn-Go)

Figure 6-9 and Figure 6-10 depict the diurnal response of tree transpiration (sap flow) in l/hr to net radiation and available energy. In both Figures, tree transpiration (sap flow) behaviour over night is similar, with the rising peak in the flux observed around 0830 hours (253.35/254.35). In Figure 6-9 the peak *Q. ilex* transpiration (sap flow) flux occurs at nearly the same time as that of net radiation. Whilst in Figure 6-10 the peak in the available energy occurs earlier than that of tree transpiration for Q. Ilex. On the basis of the better response to net radiation, the footprint up-scaling is done at the time of peak net radiation.

Hernández-Santana et al (2009) in an evaluation of the effect of drier and warmer conditions on water use by *Q. pyrenaica* in Spain also observed a better correlation between solar radiation and sap flow. Hernández-Santana et al (2009) apply a statistical test and observe an R^2 of 0.61 for solar radiation and sap flow. David et al. (2004) also use the statistical approach as they analyse approximately two years of data and they arrive at an R^2 of 0.61. However, this statistical approach is not applied in this research as the diurnal dynamics are more important so to avoid comparing fluxes with a lag. The lack of a bell shape observed in the *Q. ilex* transpiration, is consistent with the observation of *Q. ilex* transpiration published by Infante et al (2003) .

6.4. BIOMETRIC DATA

The distribution of the measured DBH and projected canopy area are shown in Figure 6-11 and Figure 6-12.

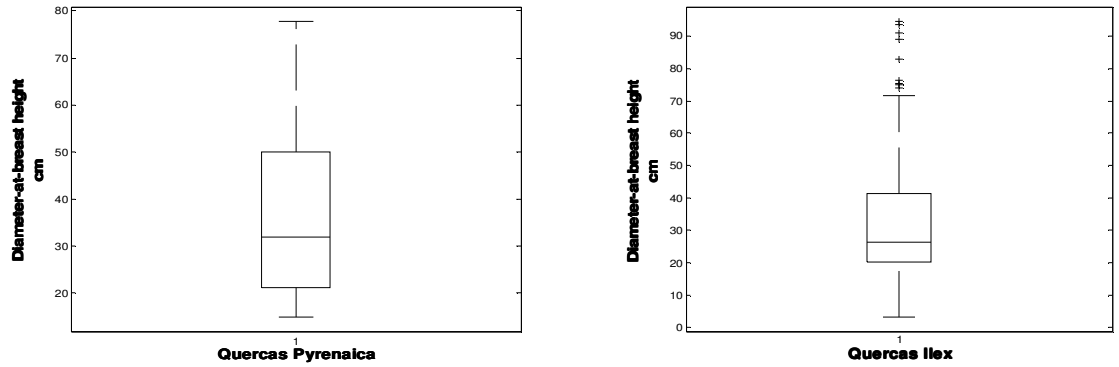

Figure 6-11: Box Plots of Field Measured Diameter-at-breast height for *Q. pyrenaica* and *ilex* - Trabadillo 2009

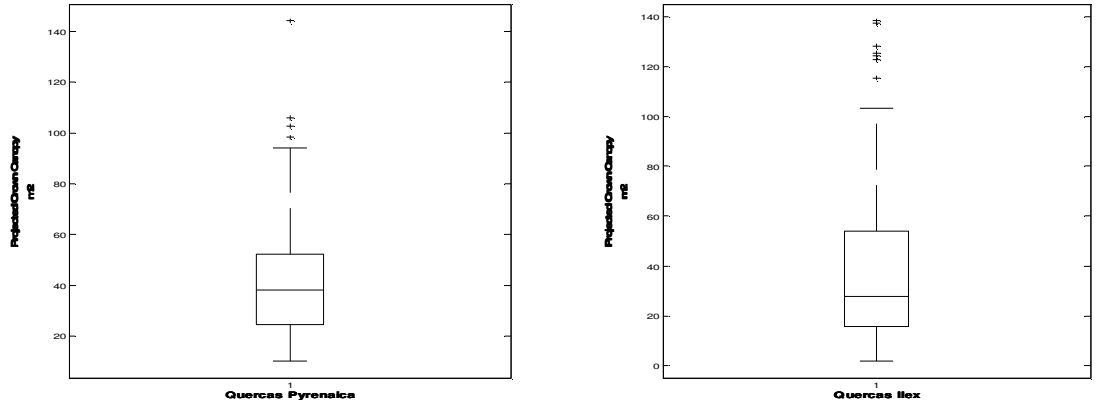

Figure 6-12: Box Plots of Field Measured Projected Crown Canopy Area for *Q. pyrenaica* and *ilex* - Trabadillo 2009

Figure 6-11 shows that the median for *Q. pyrenaica* is higher than that of the *Q. ilex* data. The whiskers show that for the *Q. pyrenaica* fewer data points are considered outliers. The minimum and maximum measured DBH for *Q. pyrenaica* is 14.9 and 94.5cm. The mean DBH is 34.9 and 37.1 for *Q. pyrenaica* and *Q. ilex* respectively. Symmetry analysis of the data shows that *Q. pyrenaica* has a skewness 1.18 compared to 0.84 for *Q. ilex*. This means that both datasets are spread more to the right of the mean. A normally distributed data would have a skewness of zero. The presence of outliers for *Q. ilex* is related to the kurtosis value of 3.6 compared to 2.33 for *Q. pyrenaica.* A kurtosis value greater than 3 shows the susceptibility of the dataset to outliers. The kurtosis calculation here does not subtract 3 from the computed value as other calculations of kurtosis do.

Figure 6-12, shows *Q. pyrenaica* with a higher median and 75 percentile values compared to *Q. ilex*. The minimum and maximum measured projected crown canopy (A_c) for *Q. pyrenaica* is 10.1 and 144 m^2 and for *Q. ilex* the minimum was 1.8 m^2 and a maximum of 138.3 m^2. The mean A_c is 44.3 and 39.6 m^2 for *Q. pyrenaica* and *Q. ilex* respectively. Skewness, a measure of asymmetry, shows that both data sets are skewed to the right side of the mean. Both datasets also have kurtosis values greater than 3 with 4.9 for *Q. pyrenaica* and 3.98 for *Q. ilex*

Having sampled trees for biometric data measurement, 22 *Q. ilex* and 20 *Q. pyrenaica* were the xylem cored with the Pressler borer to measure the xylem length or sapwood length (A_l). Figure 6-13 shows box and whisker analysis of the xylem or sapwood area data used in this research.

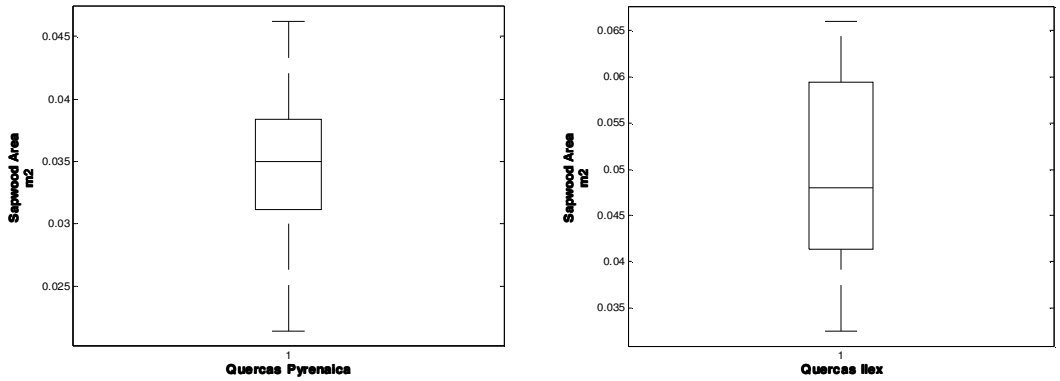

Figure 6-13: Box Plots of Field Measured Sapwood Area for *Q. pyrenaica* and i*lex* - Trabadillo 2009

Figure 6-13 shows that for the xylem area data used in this research there were no outliers with kurtosis values of 1.69 (*Q. ilex*) and 2.6 (*Q. pyrenaica*). The whiskers show that all the data is within +/- 2.7 standard deviations or 1.5 times the 25 and 75 percentile. The mean sapwood area for *Q. pyrenaica* and *Q. ilex* is 0.035 and 0.049 m^2 respectively. The minimum and maximum sapwood area is 0.033 and 0.066 for *Q. ilex* and 0.0214 and 0.0462 for *Q. pyrenaica*. Both datasets are almost symmetric about the mean with skewness values of 0.007 (*Q. ilex*) and -0.13 (*Q. pyrenaica*).

6.5. BIOMETRIC UPSCALING FUNCTIONS

In developing the biometric up-scaling function as in the work of Kimani et al (2007), Chavarro-Rincon (2009) and Ontiveros Enriquez, (2009) the relations between biometric variables was tested. The R^2 values for the relationships amongst the up-scaling scalars are tabulated in Table 6-4 and Table 6-5. The biometric variables assessed are: the height to first branching (H1B), the projected canopy area (A_c), the xylem or sapwood area (A_x) and the diameter at breast height.

Table 6-4: R-square for *Q. ilex* Biometric Data

	DBH	A_c	A_x	H1B
DBH				
Ac	0.82			
A_x	0.86	0.90		
H1B	0.40	0.43	0.32	

Table 6-5: R-Square for *Q. pyrenaica* Biometric Data

	DBH	A_c	A_x	H1B
DBH				
A_c	0.86			
A_x	0.95	0.91		
H1B	0.02	0.01	0.02	

It can be noted from Table 6-4 that a strong positive relationship exists between the projected crown canopy area (A_c) and the xylem or sapwood area – R^2 = 0.90. The second highest correlation was between DBH and xylem or sapwood area - R^2 = 0.86. In Table 6-5, the highest R^2 is observed between DBH and xylem or sapwood area - R^2 = 0.95 and the second highest R^2 was between projected crown canopy area (A_c) and the xylem or sapwood area – R^2 = 0.91. These results confirm the existence of reasonable allometric relationships between the different tree properties. Although the coefficient of determination for *Q. pyrenaica* was stronger between DBH and Xylem or Sapwood area, the use of remote sensing necessitated the use of the second highest coefficient of determination in developing the biometric up-scaling function. The reason being that the crown canopy is the most effective scalar that can be retrieved from remote sensing imagery (Lubczynski, 2009).

Biometric up-scaling functions (BUF) developed in this research are shown in Figure 6-14 and Figure 6-15.

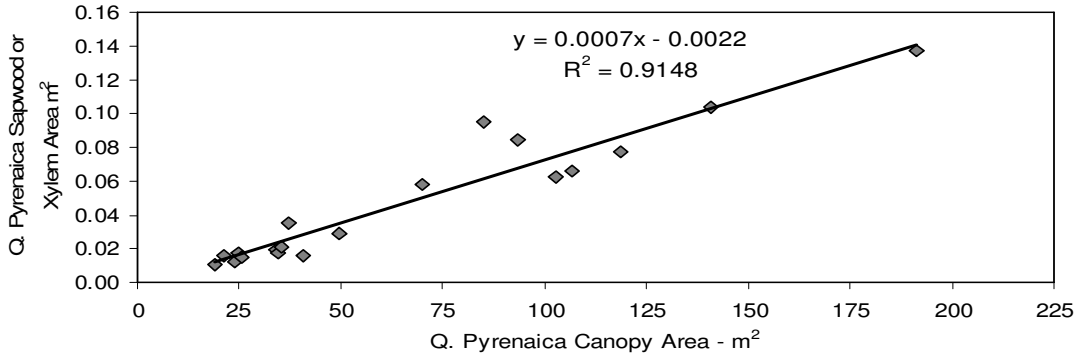

Figure 6-14: Biometric Up-scaling Function for *Q. pyrenaica* - Trabadillo 2009

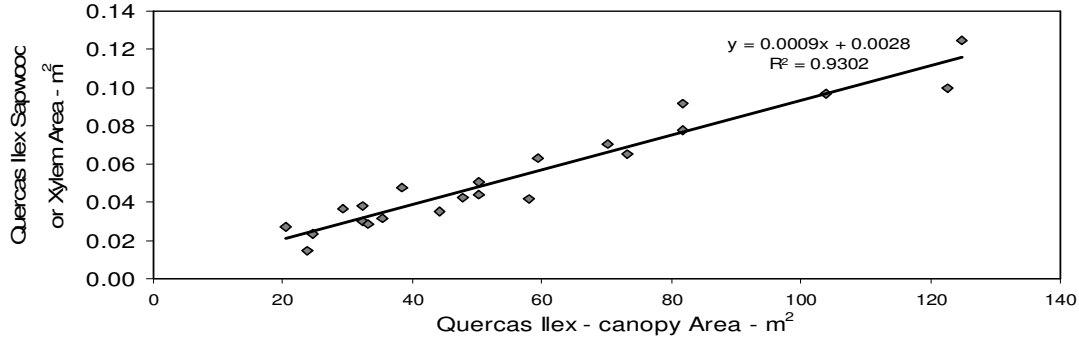

Figure 6-15: Biometric Up-scaling Function for *Q. ilex* - Trabadillo 2009

The biometric up-scaling functions (BUF) highlighted in Figure 6-14 and Figure 6-15 when compared to other BUF developed for the study area, they have a higher R^2 value. Lubczynski and Gurwin (2005) published biometric up-scaling functions that cover the study area with R^2 values of 0.62 for both *Q. pyrenaica* and *Q. ilex*. Ontiveros Enriquez (2009) produced R^2 values of 0.93 and 0.75 for *Q. pyrenaica* and *Q. ilex* respectively but the range of canopy area sizes was up to 65 m^2. In this study the range of canopy sizes reaches up to 194 m^2, and therefore the BUF in this study are more encompassing.

6.6. REMOTE SENSING IMAGERY: QUICK BIRD IMAGE

Regression analysis of the accuracy of the retrieved canopies was done and the result is shown in Figure 6-16

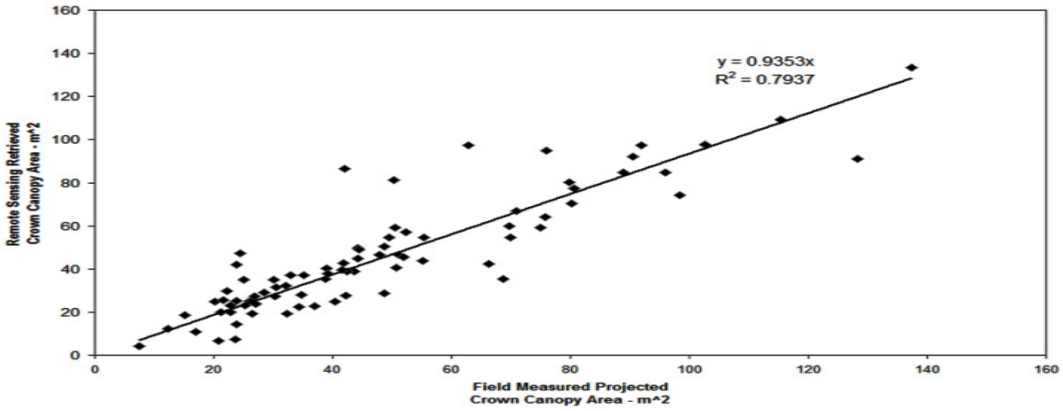

Figure 6-16: Comparison of field measured crown canopy sizes and remote sensing retrieved canopy areas

Figure 6-16 shows a comparison of canopy sizes in square metres. A coefficient of determination (R^2) of 0.79 was observed. The regression line was forced through zero so as to determine the degree of under or estimation. An underestimation of the canopy sizes by remote sensing based retrieval is about 7%. The mean canopy size of the data sets used for this validation (n = 81) were: 45.81 and 48.06 m^2 for remote sensing retrieved canopies and field measured projected crown canopy areas.

7. INTEGRATION OF EDDY FOOTPRINTS, EVAPOTRANSPIRATION,TRANSPIRATION, BIOMETRIC UP-SCALING AND REMOTE SENSING

This section focuses on the integration of data and knowledge generated in the preceding chapters. The focus is on answering the following research questions:

- How does the transpiration and evapotranspiration fluxes compare in the footprint at finer temporal scales?
- What is the significance of the research results with regards to evapotranspiration processes and the role of tree transpiration processes in WLE?

The results presented here are based on the study of the footprint on DOY 253 and DOY 247. This is mainly due to two reasons. Firstly, the criteria of selecting days with a clear sky reduced the number possible days to 6. Of which DOY 253 and 247 are included. Secondly, reasonable sap flow data was available for these days. The peak net radiation time is used in order to avoid comparing the fluxes at times with 'time-lags'. The spatial location of eddy flux footprints vary with wind direction. At each average wind direction a different footprint can be determined. In this study the 30 minute temporal time scale is used due to the fact that evapotranspiration was determined at 30 minute intervals and so was the wind direction.

7.1. EDDY FLUX FOOTPRINTS

7.1.1. EDDY FLUX FOOTPRINT DOY 253

The characteristics of the eddy flux footprint determined on DOY 253 at peak R_n are presented in Figure 7-1.

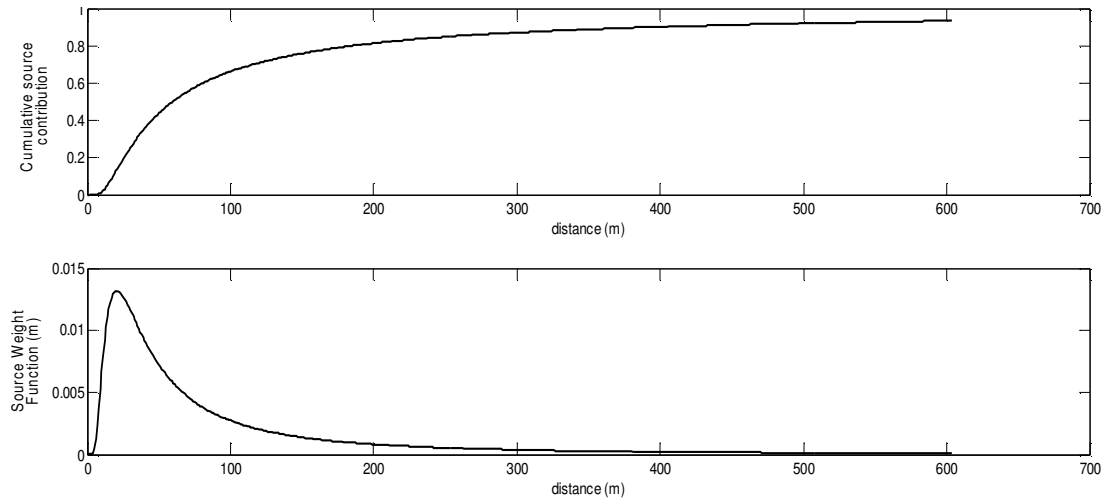

Figure 7-1: The characteristics of the eddy flux footprint on DOY 253 at peak R_n. Top - Cumulative Source Contribution of the measured flux. Bottom - the cross-wind integrated footprint 'function' at peak R_n. The location of the eddy Tower is the origin (coordinate x,y = [0,0]).

The cumulative source contribution, in Figure 7-1, (top) shows the cumulative elemental land surface contribution to the total measured flux. It can be noted at the start of the curve that there is a small distance from which there is no flux contribution (~ 5 metres). This corresponds to the area around the measuring tower that is too close to contribute a measurable flux. At a distance of 100 meters there is a contribution of ~ 60%. The contribution continues to increase until the curves plateaus at around 90%. The bottom graph (Figure 7-1) characterises the strength of the elemental surfaces with distance. The is also referred to as the cross-wind integrated footprint function (F^y). It can be noted that the land surface sources within a distance of 200 meters from the eddy tower contribute the most of the flux

The 2-D discretization of the characteristics shown in Figure 7-1 over a grid surface is shown Figure 7-2.

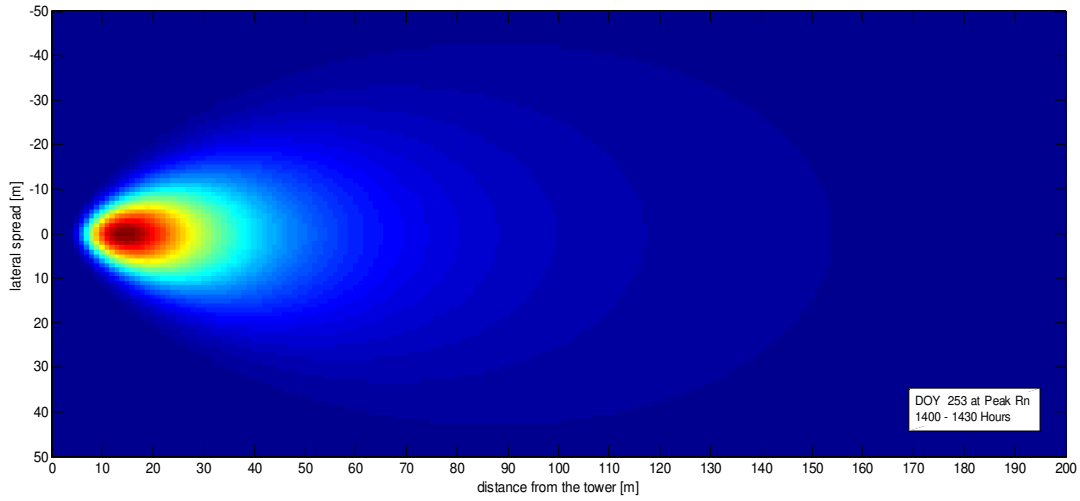

Figure 7-2: 2-D Main Source Area for the Fluxes Measured on DOY 253 at 1400 – 1430 Hours.

The implementation and integration of Figure 7-1 and Figure 7-2 is shown in Figure 7-3.

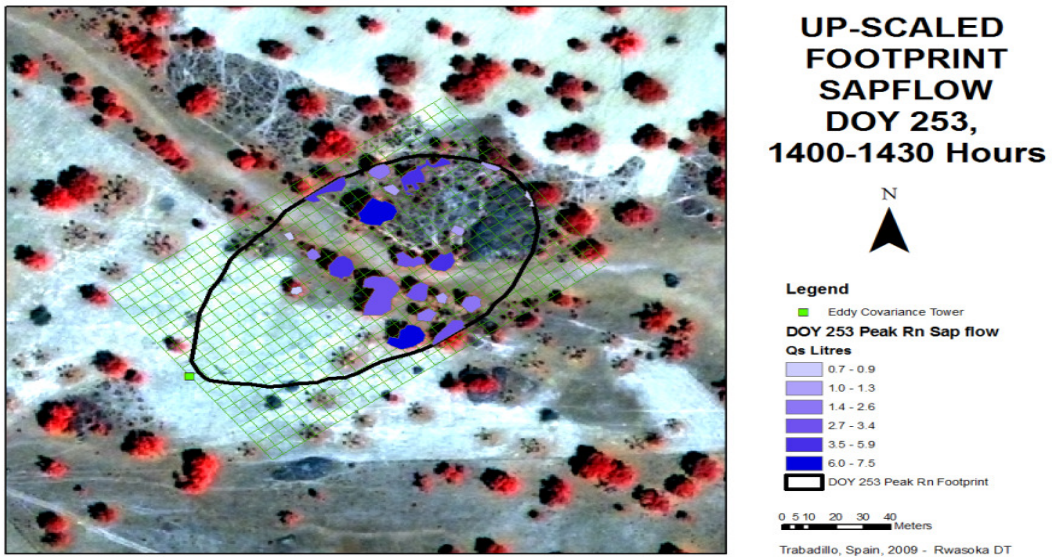

Figure 7-3: Up-scaled Footprint Sap Flow for DOY 253, 1400-1430 Hours.

Figure 7-3 shows the up-scaled transpiration flux within the eddy flux footprint depicted in Figure 7-2 and Figure 7-3. The footprint in Figure 7-3 is rotated into the mean wind direction of 54.38^0. It can be noted that the up-scaled transpiration flux over the time period ranged from, 0.69 l to 7.4 l. The relatively high transpiration flux ranging from of 5.9 - 7.4 l, is due to the retrieval of canopies over trees that are clustered together as one canopy. The retrieved canopy is thus bigger and so is the up-scaled transpiration flux.

7.1.2. EDDY FLUX FOOTPRINT DOY 247

The flux footprint at peak R_n on DOY 247 is also chosen because its mean wind direction is different from DOY 253 and the species composition is different. 66% of the canopy area is *Q. pyrenaica* and 34 % for *Q. Ilex*. This 2-D discretization of the footprint is shown in Figure 7-4.

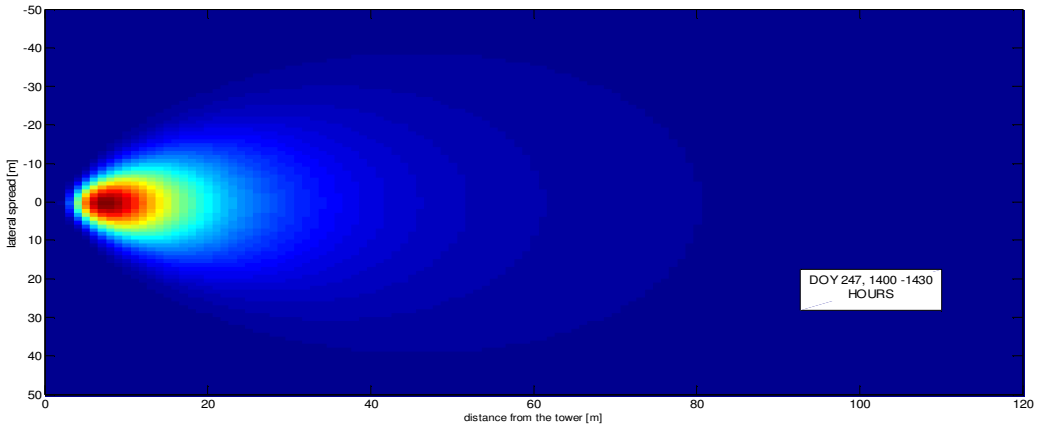

Figure 7-4: 2-D Main Source Area for the Fluxes Measured on DOY 247, 1400-1430 Hours

Figure 7-4 shows the lateral spread of the flux of 38 m from the Tower on either side. The limited lateral spread is related to the magnitude of σ_v of 1.24 m/s. The footprint up-scaling is shown in Figure 7-5

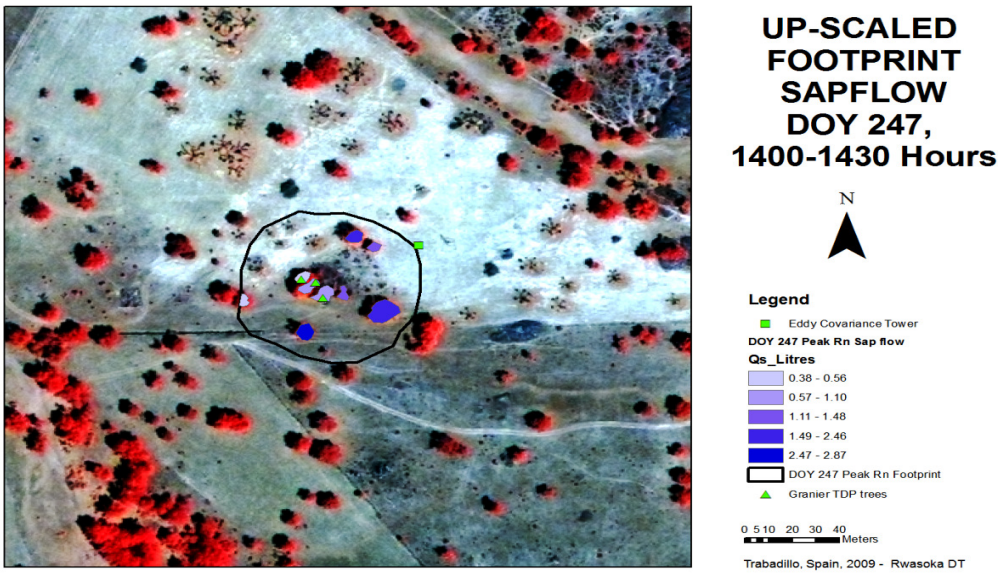

Figure 7-5: Up-scaled Footprint Sap Flow for DOY 247, 1400-1430 Hours

Figure 7-5 shows the footprint up-scaling for DOY 247 at peak R_n. The up-scaled transpiration flux for the 30 minute interval ranges from 0.38 l to 2.87 l.

The cumulative source contribution and source weight function are shown in Figure 7-6 for the footprint at peak R_n on DOY 247.

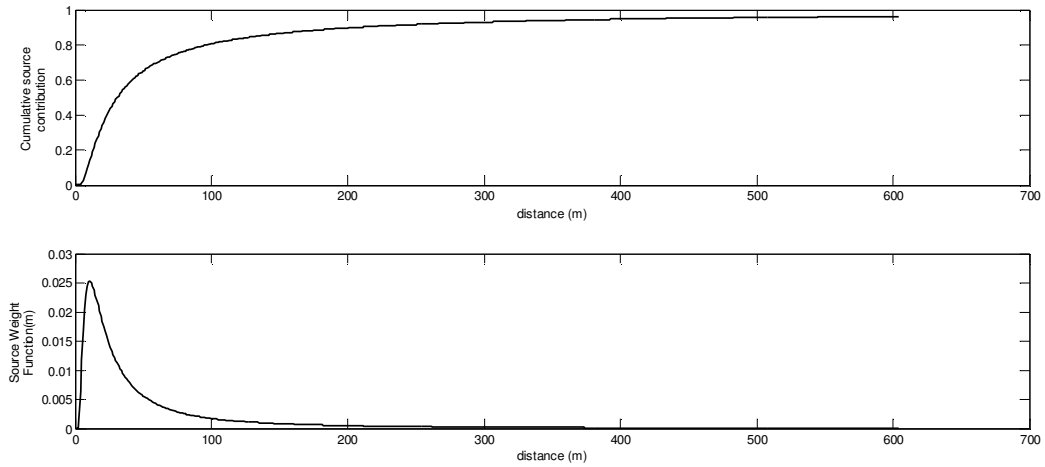

Figure 7-6: The characteristics of the flux footprint on DOY 247 at peak R_n. Top - Cumulative Source Contribution of the measured flux. Bottom - the cross-wind integrated 'function' at peak R_n. The Tower is the origin (coordinate x,y = [0,0]).

The elemental surface contribution for the first hundred metres in Figure 7-6 (top) is ~ 80% of the flux measured. The elemental contribution plateaus at 0.9 because a 90% footprint is determined. The source weight strength (Figure 7-6 – bottom) shows that major influencing land surface areas are within the first 100 meters from the eddy tower.

7.2. HOW DOES TRANSPIRATION AND EVAPOTRANSPIRATION FLUX COMPARE IN THE FOOTPRINT?

A comparison of the transpiration and evapotranspiration done based on the data of DOY 253 at peak R_n or solar noon is shown in Table 7-1.

Table 7-1: Comparison of up-scaled tree transpiration and eddy covariance ET on DOY 253 at solar noon

	m^3	m^3	m^2	mm	%
Up-scaled Sap flow					
Total *Q. pyrenaica*	0.0026				
Total *Q. ilex*	0.0546				
Total Tree Transpiration flux		0.0572			
Total crown area			1072.95		
Transpiration (per m^2 of canopy crown area)				0.053	
Footprint Area			9571		
Transpiration (per footprint area m^2)				0.0060	
Eddy Covariance ET (30mins) - m^2				0.020	
T (footprint area)/ET (%)					30.2
Implemented footprint percentage					75
Anticipated Eddy ET for the implemented footprint				0.015	
Total Transpiration Contribution for the implemented footprint					40.3

Table 7-1 presents a comparison of eddy covariance evapotranspiration and up-scaled tree transpiration on DOY 253 at 1400 to 1430 hours, local time. The total up-scaled transpiration flux over the time period amounted to 0.0572 m^3. This translates to a transpiration flux of 0.053 mm per m^2 of canopy area. The total footprint area for the DOY 253 solar noon footprint presented in Table 7-1 is 9 571 m^2 and therefore the transpiration flux amounts to 0.0060 mm m^{-2} of the footprint area. The contribution of tree transpiration to the measured flux over the time period is therefore determined as 30.2 %. However, an analysis of Figure 7-1 shows that at a cross-wind integrated footprint distance of 150 meters the cumulative source contribution is about 75%. Therefore, in simple terms, the footprint implemented accounts for ~ 75% of the flux. The tree transpiration is then related to a flux of 75% of what the eddy tower measured over the same time period. The results show that the contribution of tree transpiration in the studied footprint amounted to ~ 40.3 percent.

Table 7-2 presents a comparison of up-scaled tree transpiration and eddy covariance ET at solar noon on DOY 247 (4 September 2009).

Table 7-2: Comparison of up-scaled tree transpiration and eddy covariance ET on DOY 247 at solar noon

	m^3	m^3	m^2	mm	%
Up-scaled Sap flow					
Total *Q. pyrenaica*	0.0078				
Total *Q. ilex*	0.0053				

Total Tree Transpiration flux	0.0131		
Total crown area	369.15		
Transpiration (per m2 of crown area)		0.0355	
Footprint Area	4796		
Sapflow (per footprint area m2)		0.0027	
Eddy Covariance ET (30mins) - m2		0.0283	
T (footprint area)/ET (%)			9.7
Implemented footprint percentage			73
Anticipated Eddy ET for the implemented footprint		0.0207	
Total Transpiration Contribution for the implemented footprint			13.2

The total tree transpiration flux, in Table 7-2, is 0.0131 m^3. The total crown area for both *Q. ilex* and *pyrenaica* is 369.15 m^2. Thus the transpiration flux per m^2 of canopy is 0.0355 mm and 0.0027 mm per m^2 of footprint area for the 30 minute interval. The footprint area that was implemented in GIS accounted for a contribution of ~ 73% of the total flux and therefore considering the 73% the contribution of tree transpiration amounted to 13.2%.

The contributions of ~13.2% and ~40.3% are within the ranges the can be deduced from the work of Lubczynski and Gurwin (2005). In a modelling based paper, in the same catchment as this research, Lubczynski and Gurwin (2005) noted that dry season transpiration for Sardon catchment was approximately 0.16 mm d^{-1}. The total groundwater evapotranspiration (ET_g) was reported to be around 0.55 – 0.8 mm d^{-1}. Based on the definition, $ET_g = E_g + T_g$, Lubczynski and Gurwin (2005) present and assuming that tree transpiration is equal to T_g, the contribution of tree transpiration thus ranges from ~ 29% - 0.2% for the years 1997 – 1999 that they publish.

The reason for the percentage differences for the two footprints presented is explained by the species composition and the canopy area coverage ratios for each footprint. The footprint on DOY 253 consisted of canopy area that amounted to 1072.95 m^2 and that represents ~ 11.2% of the footprint. On the other hand, the footprint on DOY 247 had a 369.15 m^2 and this represents 7.7% of the footprint area. The other reason for the difference is that in the footprint on DOY 253, 84 % of the canopy area consisted of *Q. ilex* species that have a higher sap flux density and is more stable. In the footprint on DOY 247, *Q. ilex* only constituted 34% of the total canopy.

The key parameters such as net radiation at solar noon on DOY 253 is 426.91 W m^2 with a U_* of 0.63 and σ_v of 1.29 m/s. On DOY 247, the solar noon net radiation is 449.35 W m^2 with a U_* of 0.34 and σ_v of 1.24 m/s. When related to the measured fluxes, higher a tree transpiration contribution is found on a day with lower R_n. This supports the above mentioned reasons of species composition and the canopy area coverage ratios for each footprint as better explanations for the observations. U_* and σ_v influenced the length of the crosswind integrated footprint function and the degree of lateral spread respectively. A higher U_* is associated with a longer cross-wind integrated footprint function.

Paço et al. (2009) published a paper in which they conclude that tree transpiration constituted about 50 % of the measured ET. Their research focussed on the *Q. ilex* species, which are also studied in this research. Interestingly, in the footprint that is dominated by *Q. ilex* trees, tree transpiration is ~ 40 %. The percentage of ~ 40% is not far off, from their conclusions. However, Paço et al. (2009) do not clearly show clearly how they matched the spatial scales of eddy covariance and sap flow. They refer to Pereira et al (2007) for an explanation of their methodology but still some issues remain unclear.

7.3. WHAT IS THE SIGNIFICANCE OF THE RESEARCH RESULTS WITH REGARDS TO EVAPOTRANSPIRATION PROCESSES AND THE ROLE OF TREE TRANSPIRATION IN WLE?

The results of this study have vital implications and significance for understanding evapotranspiration processes in the study area and Water Limited Environments in general. The significance of the results is both methodological and results oriented.

From a methodological perspective, the research managed to explore an approach that combines remote sensing based up-scaling with eddy covariance through the use of the eddy flux footprint as the spatial domain for up-scaling. The gains made in this work serve as a fundamental building block to analyse evapotranspiration and transpiration links and dynamics. Such a conceptually promising approach, allows for the checking of up-scaled transpiration with physical turbulence measurements. With the availability of more footprint comparisons, it should therefore be possible to evaluate the effectiveness of the remote-sensing based approach to up-scaling tree transpiration.

It is worth noting that the approach implemented in this research has universal applicability. The same integrated approach can be applied over different land surface types as long the footprint determined is two-dimensional. However, the results are relevant for WLE and Sardon catchment in particular.

Finer temporal scale analysis of tree transpiration presented in this work showed that contribution of tree transpiration in a *Q. ilex* dominated footprint was ~ 40%. The contribution of tree transpiration in a footprint that was not dominated by *Q.* ilex had a much lower contribution percentage of ~ 13.2%.

The significance of these findings is better understood by considering the canopy area coverage statistics per footprint. The tree transpiration contribution of ~ 40% is from a footprint that represents only ~ 11.2% of the total footprint area. In the footprint of DOY 247, the up-scaled tree transpiration of 13.2% is attributed to tree canopies that cover ~7.7 % of the footprint land surface. This observation underscores the role and significance of tree transpiration in the study area and WLE in general. However, these results are still indicative, as two footprints are applied.

The role of total transpiration however should be bigger, because trees with smaller canopies could not be not be retrieved by remote sensing. In the footprint that gave a contribution ~ 40%, there were trees at the far end of the footprint, where it is rocky that could not be retrieved.

At the same time, the results also highlight the key issue of species heterogeneity as it relates to understanding the role of tree transpiration. The footprint with a much larger percentage of the *Q. ilex* had a much higher tree transpiration contribution percentage. This can be related to the generally unstable and at times lower sap flux density of *Q. pyrenaica* compared to that of *Q. ilex.*

The findings also open up thinking on evapotranspiration processes. If the tree transpiration constitutes ~ 40% or 13% of the flux then where is the other 60% or 87%? By the simple conceptual definition of evapotranspiration of $ET = E + T$, it would suffice to allocate the unaccounted for 60% of the transpiration flux to soil evaporation processes. In humid environments, this argument would hold but in Water Limited Environments and in the study area this argument is not firmly founded. The analysis of soil moisture and the total ET presented in chapter 6 indicates that there is no relation between soil moisture at 25cm and the ET. With soil moisture being as low as 0.07 [-] at 25cm and it being considered as a flux whose 'concentration, increases down the soil profile, soil moisture at the land surface can be argued to be almost nil. The lack of soil moisture at the surface or near-surface can also be inferred from the high ground (kinetic) temperatures of up 45 ^{o}C. The assumption of soil evaporation being almost nil thus holds. It is evident therefore that the definition of $ET = E + T$ thus masks out several evapotranspiration process dynamics because by taking the argument of bare soil evaporation being close to zero, this leaves ~ 60% of the flux unaccounted for on DOY 253.

The conceptual definition of evapotranspiration processes in Water Limited Environments presented by Lubczynski (2009) - (Equation 2) – thus provides a better conceptual framework. Finding the other ~ 60% of the flux thus requires evaluation of the unsaturated zone evapotranspiration. Studies in other arid areas have shown the occurrence of vapour flux loss (Obakeng, 2007; Ross, 1984; Scanlon et al., 2003). Obakeng (2007) showed that in the fringe of the Kalahari, the upward transport of liquid and water vapour occurred from as deep as ~ 25 metres. In this study, the vapour component could have gone undetected as soil moisture recording seemingly focussed on the 'liquid' component.

The unaccounted for evapotranspiration flux could also be due to limitations arising from the use of object oriented retrieval of tree canopies. At finer spatial and temporal scales, as done in this research this is critical for accurately determining the transpiration flux. A simple regression analysis that was done showed that, overall, remote sensing based retrieval underestimated the tree canopies by 7%. What also emerged as being critical is not just the accurate retrieval of canopy sizes, but also their spatial location. A minor displacement of the position or extreme irregularity of the polygon could be critical in determining whether or not the canopy is inside or outside of the footprint. This therefore determines whether or not the canopy is included in the up-scaling. However, over relatively larger spatial areas, this challenge would be different as there might be compensation of canopy under and overestimation.

The results from the energy balance assessment are also important. The results show the dynamics and importance of soil heat flux in accounting for the surface energy balance fluxes (Figure 5-3). It is observed that the use of soil flux plates alone results in diurnal underestimation of soil heat flux at peak solar noon and from sunset to sunrise of the following day. This confirms the observations of Ochsner et al (2006) who also noted the same problem. The magnitude of soil heat flux is observed to go up to 45 - 50% of net radiation. This observation is significant upon consideration of efforts in evapotranspiration

modelling using remote sensing. Some of the empirical or semi-empirical methods for quantification of soil heat flux that are used to solve the energy balance might need to be reassessed.

The high energy balance closure achieved in this study without the consideration other heat storage terms such as biomass. This high energy balance closure can be attributed to the calculation of soil heat flux that considers the storage term. This finding reiterates the conclusions of Heusinkveld et al (2004) that soil heat flux in dry areas plays a crucial role.

8. CONCLUSIONS AND RECOMMENDATIONS

8.1. CONCLUSIONS

This research presents the surface energy balance and the evapotranspiration in a Water Limited Environment in Trabadillo, Spain. The study made use of a unique array of the evapotranspiration and transpiration methods. For the first time, this study integrated remote-sensing based tree transpiration, up-scaling with eddy covariance. The conclusions that can be drawn from this study are:

1 Diurnally, soil heat flux can reach up to 40-50% of net radiation and that at times soil heat flux is the second largest flux of the surface energy balance.

2 The accurate determination of soil flux in dry areas plays a crucial role in attaining a high energy balance closure. In this study a closure percentage of 85% using 30 minute data and 92% when daily averaged data was achieved. The surface energy balance closure analysis was based on the basic definition ($R_n = H + LE + Go$) without considering heat storage terms such as biomass.

3 This study presents Biometric Up-scaling Functions with a higher coefficient of determination compared to previously published work for the same study area (Lubczynski and Gurwin, 2005). When the BUFs are compared to those of Ontiveros Enriquez (2009)

the Biometric Up-scaling Functions in this study are based on a much broader range of field canopy measurements.

4 The footprint based approach applied in this research is conceptually promising. It allowed for the combination of remote sensing up-scaled tree transpiration with physical turbulence measurements for the first time.

5 The integration of eddy flux footprint and the remote-sensing up-scaled sap flow in this study, at 75% cumulative source contribution, showed that ~ 40 % of the flux measured by eddy covariance on DOY 253 was in the form of tree transpiration. This is in near-agreement with earlier studies of Paço et al (2009) who conclude that tree transpiration constituted 50% of the total evapotranspiration.

6 The ~ 40% contribution, at 75% cumulative source contribution, emphasizes the important role of tree transpiration in Water Limited Environments. The tree canopy area constitutes ~ 11% of the studied eddy flux footprint. The relationship of the ~11% of the footprint contributing ~ 40% of the flux has major implications on our quantitative understanding and modelling of evapotranspiration in Water limited Environments and in particular the study area. However, it should be noted that these results are more indicative of dry season evapotranspiration and in particular, of the driest time of the dry season. September constitutes one of the driest months of the dry season in the study area.

7 In WLE, the contribution of vapour flux needs to be understood. If ~40% or 13 % of the flux can be attributed to tree transpiration and the measured soil moisture indicates that the land surface is dry, then the question that needs to be answered is, where does the remaining 60% or 87% come from?

8.2. RECOMMENDATIONS

The recommendations from this research are:

1 To gain more understanding on the effectiveness of the remote-sensing based up-scaling, there is need to have a more intensive sap flow measuring campaign in the areas that influence the tower. These measurements to be complemented with intensive measuring of tree biometric properties. Such that up-scaling within the footprint can also be done based on field biometric data. The output is then compared to outputs of the remote-sensing approach within the footprint.

2 Applying higher order, eddy flux footprints methods (large eddy simulation and Lagrangian stochastic dispersion) in also vital to improve our understanding of the footprint based approach to up-scaling combined with remote-sensing.

3 More research on understanding the evapotranspiration budget in WLE is needed. In addition to the method or approach used in this research, a quantification of vapour flux is crucial so as to close the evapotranspiration budget.

REFERENCES

Abrahams, A.D. and Parsons, A.J. (Editors), 1994. Geomorphology of Desert Environments. Chapman & Hall, London etc., 674 pp.

Agbakpe, B., 2010. Estimating tree groundwater transpiration in La Mata Catchment, Spain. MSc Thesis, ITC, Enschede.

Allen, R.G., Pereira, L.S., Raes, D. and Smith, M., 1998. Crop evapotranspiration : guidelines for computing crop water requirements. FAO irrigation and drainage paper;56. FAO, Rome, 300 pp.

Aranda, I., Gil, L. and Pardos, J.A., 2004. Osmotic adjustment in two temperate oak species [Quercus pyrenaica Willd and Quercus petraea (Matt.) Liebl] of the Iberian Peninsula in response to drought. Investigación Agraria, Sistemas y Recursos Forestales, 13(2): 339-345.

Arya, S.P., 1988. Introduction to Micrometeorology. Academic Press, California/London.

Aubinet, M., Grelle, A., Ibrom, A., Rannik, Ü., Moncrieff, J., Foken, T., Kowalski, A.S., Martin, P.H., Berbigier, P., Bernhofer, C., Clement, R., Elbers, J.A., Granier, A., Grünwald, T., Morgenstern, K., Pilegaard, K., Rebmann, C., Snijders, W., Valentini, R. and Vesala, T., 2000. Estimates of the Annual Net Carbon and Water Exchange of Forests: the EUROFLUX Methodology. Adv. Ecol. Research, 30: 113-175.

Baldocchi, D., Falge, E., Gu, L., Olson, R., Hollinger, D., Running, S., Anthoni, P., Bernhofer, C., Davis, K., Evans, R., Fuentes, J., Goldstein, A., Katul, G., Law, B., Lee, X., Malhi, Y., Meyers, T., Munger, W., Oechel, W., Paw, K.T., Pilegaard, K., Schmid, H.P., Valentini, R., Verma, S., Vesala, T., Wilson, K. and Wofsy, S., 2001. FLUXNET: A New Tool to Study the Temporal and Spatial Variability of Ecosystem-Scale Carbon Dioxide, Water Vapor, and Energy Flux Densities. Bulletin of the American Meteorological Society, 82(11): 2415-2434.

Baldocchi, D.D. and Rao, K.S., 1995. Intra-field variability of scalar flux densities across a transition between a desert and an irrigated potato field. Boundary-Layer Meteorology, 76(1): 109-136.

Baldocchi, D.D., Xu, L. and Kiang, N., 2004. How plant functional-type, weather, seasonal drought, and soil physical properties alter water and energy fluxes of an oak-grass savanna and an annual grassland. Agricultural and Forest Meteorology, 123(1-2): 13-39.

Barr, A.G., Morgenstern, K., Black, T.A., McCaughey, J.H. and Nesic, Z., 2006. Surface energy balance closure by the eddy-covariance method above three boreal forest stands and implications for the measurement of the CO2 flux. Agricultural and Forest Meteorology, 140(1-4): 322-337.

Brutsaert, W., 1982. Evaporation into the atmosphere: theory, history, and applications. Reidel Publishing, Dordrecht etc., 299 pp.

Brutsaert, W., 2005. Hydrology: An Introduction. Cambridge University Press, Cambridge, 605 pp.

Burba, G.G., McDermitt, D.K., Grelle, A., Anderson, D.J. and Xu, L., 2008. Addressing the influence of instrument surface heat exchange on the measurements of CO2 flux from open-path gas analyzers. Global Change Biology, 14: 1854-1876.

Campbell Scientific, 1996. CSAT 3 3-D Sonic Anemometers.http://www.campbellsci.com/documents/product-brochures/b_csat3.pdf, Oct 26

Čermák, J., Kučera, J. and Nadezhdina, N., 2004. Sap flow measurements with some thermodynamic methods, flow integration within trees and scaling up from sample trees to entire forest stands. Trees - Structure and Function, 18(5): 529-546.

Cermak, J. and Nadezhdina, N., 1998. Sapwood as the scaling parameter- defining according to xylem water content or radial pattern of sap flow? Ann. For. Sci., 55(5): 509-521.

Chavarro-Rincon, D.C., 2009. Tree transpiration mapping from upscaled sap flow in the Botswana Kalahari. PhD Thesis, ITC University of Twente, Enschede, 141 pp.

Chen, Q., Baldocchi, D., Gong, P. and Kelly, M., 2006. Isolating Individual Trees in a Savanna Woodland Using Small Footprint Lidar Data. Photogrammetric Engineering & Remote Sensing, Vol. 72(No. 8): 923-932.

Clearwater, M.J., Meinzer, F.C., Andrade, J.L., Goldstein, G. and Holbrook, N.M., 1999. Potential errors in measurement of nonuniform sap flow using heat dissipation probes. Tree Physiol, 19(10): 681-687.

David, T.S., Ferreira, M.I., Cohen, S., Pereira, J.S. and David, J.S., 2004. Constraints on transpiration from an evergreen oak tree in southern Portugal. Agricultural and Forest Meteorology, 122(3-4): 193-205.

David, T.S., Henriques, M.O., Kurz-Besson, C., Nunes, J., Valente, F., Vaz, M., Pereira, J.S., Siegwolf, R., Chaves, M.M., Gazarini, L.C. and David, J.S., 2007. Water-use strategies in two co-occurring Mediterranean evergreen oaks: surviving the summer drought. Tree Physiol, 27(6): 793-803.

De Vries, D.A., 1963. Thermal Properties of Soils. In: W.R. van Wijk (Editor), Physics of Plant Environment. North-Holland Co, Amsterdam, pp. 210-235.

Detto, M., Montaldo, N., Albertson, J.D., Mancini, M. and Katul, G., 2006. Soil moisture and vegetation controls on evapotranspiration in a heterogeneous Mediterranean ecosystem on Sardinia, Italy. Water Resour. Res., 42.

Finkelstein, P.L. and Sims, P.F., 2001. Sampling error in eddy correlation flux measurements. J. Geophys. Res., 106(D4): 3503-3509.

Finnigan, J., 2004. The footprint concept in complex terrain. Agricultural and Forest Meteorology, 127(3-4): 117-129.

Foken, T., 2008a. The Energy Balnace Closure Problem: An Overview. Ecological Applications, 18(6): 1351-1367.

Foken, T., 2008b. Micrometeorology. Springer-verlag, Berlin, 306 pp.

Foken, T., Goeckede, M., Mauder, M., Mahart, L., Amiro, B. and Munger, W., 2004. Post-field Data Quality Control. In: X. Lee, W. Massman and B. Law (Editors), Handbook of micrometeorology : a guide for surface flux measurements and analysis. Kluwer Academic Publishers, Dordrecht, pp. 181-208.

Foken, T., Mauder, M., Liebethal, C., Wimmer, F., Beyrich, F., Leps, J.-P., Raasch, S., DeBruin, H., Meijninger, W. and Bange, J., 2009. Energy balance closure for the LITFASS-2003 experiment. Theoretical and Applied Climatology.

Foken, T. and Wichura, B., 1996. Tools for quality assessment of surface - based flux measurements. In: Agricultural and Forest Meteorology, 78(1996), pp. 83-105.

Fuehrer, P.L. and Friehe, C.A., 2002. Flux Corrections Revisited. Boundary-Layer Meteorology, 102(3): 415-458.
Garratt, J.R., 1994. The Atmospheric Boundary Layer. Cambridge University Press, Cambridge, 316 pp.
Gash, J.H.C.e. and Shuttleworth, J.e., 2007. Evaporation. Benchmark papers in hydrology;. International Association of Hydrological Sciences (IAHS), Wallingford, 131 pp.
Göckede, M., Rebmann, C. and Foken, T., 2004. A combination of quality assessment tools for eddy covariance measurements with footprint modelling for the characterisation of complex sites. Agricultural and Forest Meteorology, 127(3-4): 175-188.
Granier, A., 1985. nouvelle methode pour la mesure du flux de seve brute dans le tronc des arbres. In: Ann. Sci. for., 42(1985)2, pp. 193-200.
Granier, A., 1987. Evaluation of transpiration in a douglas - fir stand by means of sap flow measurements. In: Tree Physiology, 3(1987), pp. 309-320.
Grissino-Mayer, H.D., 2003. A Manual and tutorial for the proper use of an increment borer. Tree-Ring Research, 59(2): 63-79.
Gryning, S.E., Holtslag, A.A.M., Irwin, J.S. and Sivertsen, B., 1987. Applied dispersion modelling based on meteorological scaling parameters. Atmospheric Environment (1967), 21(1): 79-89.
Herbst, M., Kutsch, W.L., Hummelshøj, P., Jensen, N.O. and Kappen, L., 2002. Canopy physiology: interpreting the variations in eddy fluxes of water vapour and carbon dioxide observed over a beech forest. Basic and Applied Ecology, 3(2): 157-169.
Hernández-Santana, V., Martínez-Vilalta, J., Martínez-Fernández, J. and Williams, M., 2009. Evaluating the effect of drier and warmer conditions on water use by Quercus pyrenaica. Forest Ecology and Management, 258(7): 1719-1730.
Heusinkveld, B.G., Jacobs, A.F.G., Holtslag, A.A.M. and Berkowicz, S.M., 2004. Surface energy balance closure in an arid region: role of soil heat flux. Agricultural and Forest Meteorology, 122(1-2): 21-37.
Holton, J.R., 2004. An Introduction to Dynamic Meteorology. Elsevier Academic Press, California/London, 553 pp.
Horst, T.W., 1997. A Simple Formula for Attenuation of Eddy Fluxes Measured With First-Order-Response Scalar Sensors
Boundary-Layer Meteorology, 82(2): 219-233.
Horst, T.W. and Weil, J.C., 1992. Footprint estimation for scalar flux measurements in the atmospheric surface layer. Boundary-Layer Meteorology, 59(3): 279-296.
Horst, T.W. and Weil, J.C., 1994. How Far is Far Enough?: The Fetch Requirements for Micrometeorological Measurement of Surface Fluxes. Journal of Atmospheric and Oceanic Technology, 11(4): 1018-1025.
Hsieh, C.-I., Katul, G. and Chi, T.-w., 2000. An approximate analytical model for footprint estimation of scalar fluxes in thermally stratified atmospheric flows. Advances in Water Resources, 23(7): 765-772.
Infante, J.M., Domingo, F., Fernández Alés, R., Joffre, R. and Rambal, S., 2003. Quercus ilex Transpiration as Affected by a Prolonged Drought Period. Biologia Plantarum, 46(1): 49-55.
Jacobs, A., Heusinkveld, B. and Holtslag, A., 2008. Towards Closing the Surface Energy Budget of a Mid-latitude Grassland. Boundary-Layer Meteorology, 126(1): 125-136.
Kaimal, J.C. and Finnigan, J.J., 1994. Atmospheric boundary layer flows : their structure and measurement. Oxford University Press, Oxford, 289 pp.
Katul, G., Cava, D., Poggi, D., Albertson, J. and Mahart, L., 2004. Stationarity, Homegeneity, and Ergodicity in Canopy Turbulence. In: X. Lee, W.J. Massman and B. Law (Editors), Handbook of micrometeorology: a guide for surface flux measurements and analysis. Kluwer Academic Publishers, Dordrecht, pp. 161-180.
Kim, J., Guo, Q., Baldocchi, D.D., Leclerc, M.Y., Xu, L. and Schmid, H.P., 2006. Upscaling fluxes from tower to landscape: Overlaying flux footprints on high-resolution (IKONOS) images of vegetation cover. Agricultural and Forest Meteorology, 136(3-4): 132-146.

Kimani, J., Hussin, Y.A., Lubczynski, M.W., Chavarro Rincon, D.C. and Obakeng, O.T., 2006. High - resolution remote sensing and object - oriented classification of savannah vegetation for mapping transpiration. In: AARSE 2006 : Proceeding of the 6th AARSE international conference on earth observation and geoinformation sciences in support of Africa's development, 30 October - 2 November 2006, Cairo, Egypt. Cairo : The National Authority for Remote Sensing and Space Science (NARSS), 2006. ISBN 1-920-01710-0. 9 p.

Kimani, J.N., 2005. Mapping of dry savannah tree species using object oriented classification and high resolution imagery in Serowe, Botswana, ITC, Enschede, 79 pp.

Kimani, J.N., Hussin, Y.A., Lubczynski, M.W., Chavarro Rincon, D.C. and Obakeng, O.T., 2007. Mapping savannah trees in Kalahari using high resolution remotely sensed images and object - oriented classification. International journal of geoinformatics, 3(2).

Kipp & Zonen, 2002. CNR 1 Net radiometer Instruction Manual, Delft, the Netherlands, pp. 46.

Kljun, N., Rotach, M.W. and Schmid, H.P., 2002. A Three-Dimensional Backward Lagrangian Footprint Model For A Wide Range Of Boundary-Layer Stratifications. Boundary-Layer Meteorology, 103(2): 205-226.

Kormann, R. and Meixner, F., 2001. An Analytical Footprint Model For Non-Neutral Stratification. Boundary-Layer Meteorology, 99(2): 207-224.

Kowalski, A., 2006. Further Comment on "Reply to the Comment by Kowalski on 'An Alternative Approach for CO2 Flux Correction Caused by Heat and Water Vapour Transfer' by Liu". Boundary-Layer Meteorology, 120(2): 365-366.

Kumagai, T.o., Nagasawa, H., Mabuchi, T., Ohsaki, S., Kubota, K., Kogi, K., Utsumi, Y., Koga, S. and Otsuki, K., 2005. Sources of error in estimating stand transpiration using allometric relationships between stem diameter and sapwood area for Cryptomeria japonica and Chamaecyparis obtusa. Forest Ecology and Management, 206(1-3): 191-195.

Kurbanmuradov, O. and Sabelfeld, K., 2000. Lagrangian Stochastic Models For Turbulent Dispersion In The Atmospheric Boundary Layer. Boundary-Layer Meteorology, 97(2): 191-218.

Lee, X., Finnigan, J. and Paw U, K.T., 2004. Coordinate Systems and Flux Bias Error. In: X. Lee, W.J. Massman and B. Law (Editors), Handbook of micrometeorology: a guide for surface flux measurements and analysis. Kluwer Academic, Dordrecht etc., pp. 33-66.

Lemeur, R., Fernández, J.E. and Steppe, K., 2009. Symbols, SI Units and Physical Quantities Within the Scope of Sap Flow Studies. Acta Horticulture(846): 21-32.

Leuning, R., 2005. Measurements of Trace Gas Fluxes in the Atmosphere Using Eddy Covariance: WPL Corrections Revisited. In: X. Lee, W.J. Massman and B. Law (Editors), Handbook of Micrometeorology, pp. 119-132.

Leuning, R., 2007. The correct form of the Webb, Pearman and Leuning equation for eddy fluxes of trace gases in steady and non-steady state, horizontally homogeneous flows. Boundary-Layer Meteorology, 123(2): 263-267.

Liebethal, C. and Foken, T., 2003. On the Significance of the Webb Correction to Fluxes. Boundary-Layer Meteorology, 109(1): 99-106.

Liu, H., 2005. An Alternative Approach for CO2 Flux Correction Caused by Heat and Water Vapour Transfer. Boundary-Layer Meteorology, 115(1): 151-168.

Liu, H., Peters, G. and Foken, T., 2001. New Equations For Sonic Temperature Variance And Buoyancy Heat Flux With An Omnidirectional Sonic Anemometer. Boundary-Layer Meteorology, 100(3): 459-468.

Lu, P., Urban, L. and Zhao, P., 2004. Granier's Thermal Dissipation Probe (TDP) Method for Measuring Sap Flow in Trees: Theory and Practice. Acta botanica sinica 46(6).

Lubczynski, M., 2009. The hydrogeological role of trees in water-limited environments. Hydrogeology Journal, 17(1): 247-259.

Lubczynski, M.W. and Gurwin, J., 2005. Integration of various data sources for transient groundwater modeling with spatio-temporally variable fluxes--Sardon study case, Spain. Journal of Hydrology, 306(1-4): 71-96.

Marcolla, B. and Cescatti, A., 2005. Experimental analysis of flux footprint for varying stability conditions in an alpine meadow. Agricultural and Forest Meteorology, 135(1-4): 291-301.

Massman, W.J., 2000. A simple method for estimating frequency response corrections for eddy covariance systems. Agricultural and Forest Meteorology, 104(3): 185-198.

Massman, W.J. and Lee, X., 2002. Eddy covariance flux corrections and uncertainties in long-term studies of carbon and energy exchanges. Agricultural and Forest Meteorology, 113(1-4): 121-144.

Matson, P. and Goldstein, A., 2000. Biogenic Trace Gas Exchanges. In: O.E. Sala, R.B. Jackson, H.A. Mooney and R.W. Howarth (Editors), Methods in Ecosystem Science. Springer, New York.

Mauder, M. and Foken, T., 2004. Documentation and Instruction Manual of the Eddy Covariance Software Package TK2 www.geo.uni-bayreuth.de/mikrometeorologie/ARBERG/ARBERG26.pdf, 27-May-2009

Mauder, M., Jegede, O.O., Okogbue, E.C., Wimmer, F. and Foken, T., 2007. Surface energy balance measurements at a tropical site in West Africa during the transition from dry to wet season. Theoretical and Applied Climatology, 89(3): 171-183.

Meinzer, F.C., Goldstein, G. and Andrade, J.L., 2001. Regulation of water flux through tropical forest canopy trees: Do universal rules apply? Tree Physiol, 21(1): 19-26.

Miller, G.R., 2009. Measuring and Modeling Interactions Between Groundwater, Soil Moisture, and Plant Transpiration in Natural and Agricultural Ecosystems. PhD Thesis, UNIVERSITY OF CALIFORNIA, BERKELEY.

Moncrieff, J., Clement, R., Finnigan, J. and Meyers, T., 2005. Averaging, Detrending, and Filtering of Eddy Covariance Time Series. In: X. Lee, W.J. Massman and B. Law (Editors), Handbook of Micrometeorology. Kluwer Academic Publishers, Dordrecht, pp. 7-31.

Moncrieff, J.B., Jarvis, P.G. and Valentini, R., 2000. Canopy Fluxes. In: O.E. Sala, R.B. Jackson, H.A. Mooney and H. R.W (Editors), Methods in ecosystem science. Springer, New York, pp. 421.

Moore, C.J., 1986. Frequency response corrections for eddy correlation systems. Boundary-Layer Meteorology, 37(1): 17-35.

Newman, B.D., Wilcox, B.P., Archer, S.R., Breshears, D.D., Dahm, C.N., Duffy, C.J., McDowell, N.G., Phillips, F.M., Scanlon, B.R. and Vivoni, E.R., 2006. Ecohydrology of water-limited environments: A scientific vision. Water Resour. Res., 42.

Obakeng, O.T., 2007. Soil moisture dynamics and evapotranspiration at the fringe of the Botswana Kalahari. PhD Thesis, Vrije Universiteit, Amsterdam.

Ochsner, T.E., Sauer, T.J. and Horton, R., 2006. Field Tests of the Soil Heat Flux Plate Method and Some Alternatives. Agronomy J, 98(4): 1005-1014.

Oishi, A.C., Oren, R. and Stoy, P.C., 2008. Estimating components of forest evapotranspiration: A footprint approach for scaling sap flux measurements. Agricultural and Forest Meteorology, 148(11): 1719-1732.

Ontiveros Enriquez, R., 2009. Tree transportation : a spatio - temporal approach in water limited environments, Sardon study case. MSc Thesis Thesis, ITC, Enschede, 65 pp.

Paço, T.A., David, T.S., Henriques, M.O., Pereira, J.S., Valente, F., Banza, J., Pereira, F.L., Pinto, C. and David, J.S., 2009. Evapotranspiration from a Mediterranean evergreen oak savannah: The role of trees and pasture. Journal of Hydrology, 369(1-2): 98-106.

Paw U, K.T., Baldocchi, D.D., Meyers, T.P. and Wilson, K.B., 2000. Correction Of Eddy-Covariance Measurements Incorporating Both Advective Effects And Density Fluxes. Boundary-Layer Meteorology, 97(3): 487-511.

Pereira, J.S., Mateus, J.A., Aires, L.M., Pita, G., Pio, C., David, J.S., Andrade, V., Banza, J., David, T.S., Paco, T.A. and Rodrigues, A., 2007. Net ecosystem carbon exchange in three contrasting Mediterranean ecosystems – the effect of drought. Biogeosciences, 4(5): 791-802.

Philip, J.R., 1961. The Theory of Heat Flux Meters. J. Geophys. Res., 66.

Rannik, Ü., Markkanen, T., Raittila, J., Hari, P. and Vesala, T., 2003. Turbulence Statistics Inside and Over Forest: Influence on Footprint Prediction. Boundary-Layer Meteorology, 109(2): 163-189.

Raupach, M.R., 1989. Applying Lagrangian fluid mechanics to infer scalar source distributions from concentration profiles in plant canopies. Agricultural and Forest Meteorology, 47(2-4): 85-108.

Ross, B., 1984. A Conceptual Model of Deep Unsaturated Zones With Negligible Recharge. Water Resour. Res., 20(11): 1627-1629.

Ruwan Rajapakse, R.R.G., 2009. Numerical groundwater flow and solute transport modelling : a case study of Sardon catchment in Spain, ITC, Enschede, 92 pp.

Salinas, A.I., 2010. A case study on the upscaling of tree transpiration in Water Limited Environments. MSc Thesis, University of Southampton(UK), Lund University (Sweden), University of Warsaw (Poland), International Institute of Geo-information Science and Earth Observation-University of Twente (The Netherlads), Enschede.

Santana, H.V., 2008. Respvesta Del Roble Melojo (Quercas pyrenaica Willd.) Frente al Deficit Hidro Bajo Condiciones Ambientales Mediterraneas Subhumedas en el Sistema Central. PhD Thesis, Unviversidad de Salamanca, Salamanca, 225 pp.

Sauer, T.J., Meek, D.W., Ochsner, T.E., Harris, A.R. and Horton, R., 2003. Errors in Heat Flux Measurement by Flux Plates of Contrasting Design and Thermal Conductivity. Vadose Zone J, 2(4): 580-588.

Scanlon, B.R., Keese, K., Reedy, R.C., Simunek, J. and Andraski, B.J., 2003. Variations in flow and transport in thick desert vadose zones in response to paleoclimatic forcing (0-90 kyr): Field measurements, modeling, and uncertainties. Water Resour. Res., 39.

Schaeffer, S.M., Williams, D.G. and Goodrich, D.C., 2000. Transpiration of cottonwood/willow forest estimated from sap flux. Agricultural and Forest Meteorology, 105(1-3): 257-270.

Schmid, H.P., 1994. Source areas for scalars and scalar fluxes. Boundary-Layer Meteorology, 67(3): 293-318.

Schmid, H.P., 1997. Experimental design for flux measurements: matching scales of observations and fluxes. Agricultural and Forest Meteorology, 87(2-3): 179-200.

Schotanus, P., Nieuwstadt, F.T.M. and Bruin, H.A.R., 1983. Temperature measurement with a sonic anemometer and its application to heat and moisture fluxes. Boundary-Layer Meteorology, 26(1): 81-93.

Schuepp, P.H., Leclerc, M.Y., MacPherson, J.I. and Desjardins, R.L., 1990. Footprint prediction of scalar fluxes from analytical solutions of the diffusion equation. In: Boundary-Layer Meteorology, 50(1990), pp. 355-373.

Simmers, I.e. (Editor), 2003. Understanding water in a dry environment : hydrological processes in arid and semi - arid zones. International Contributions to Hydrogeology : IAH International Association of Hydrogeologists;23. Balkema, Lisse etc., 341 pp.

Sogachev, A., Rannik, Ü. and Vesala, T., 2004. Flux footprints over complex terrain covered by heterogeneous forest. Agricultural and Forest Meteorology, 127(3-4): 143-158.

Stull, R.B., 1998. Introduction to Boundary Layer Meteorology. Kluwer Academic Publishers, Dordrecht/Boston/London, 666 pp.

Stull, R.B., 2000. Meteorology for scientists and engineers. Brooks Cole, Pacific Grove etc., 501 pp.

Swinbank, W.C., 1951. The measurement of vertical transfer of heat and water vapor by eddies in the lowe atmosphere. Journal of the Atmospheric Sciences, 8(3): 135-145.

Tanaka, H., Hiyama, T., Kobayashi, N., Yabuki, H., Ishii, Y., Desyatkin, R.V., Maximov, T.C. and Ohta, T., 2008. Energy balance and its closure over a young larch forest in eastern Siberia. Agricultural and Forest Meteorology, 148(12): 1954-1967.

Thomson, D.J., 1987. Criteria for the selection of stochastic models of particle trajectories in turbulent flows. Journal of Fluid Mechanics Digital Archive, 180(-1): 529-556.

Twine, T.E., Kustas, W.P., Norman, J.M., Cook, D.R., Houser, P.R., Meyers, T.P., Prueger, J.H., Starks, P.J. and Wesely, M.L., 2000. Correcting eddy-covariance flux underestimates over a grassland. Agricultural and Forest Meteorology, 103(3): 279-300.

Vesala, T., Kljun, N., Rannik, Ü., Rinne, J., Sogachev, A., Markkanen, T., Sabelfeld, K., Foken, T. and Leclerc, M.Y., 2008. Flux and concentration footprint modelling: State of the art. Environmental Pollution, 152(3): 653-666.

Webb, E.K., Pearman, G.I. and Leuning, R., 1980. Correction of flux measurements for density effects due to heat and water vapour transfer. Quarterly Journal of the Royal Meteorological Society, 106(447): 85-100.

Weber, S., 2006. Comparison of in-situ measured ground heat fluxes within a heteorogeneous urban ballast layer. Theoretical and Applied Climatology, 83(1): 169-179.

Wilcox, B.P., Seyfried, M.S. and Breshears, D.D., 2003. The water balance on rangelands. In: B.A. Stewart and T.A. Howell (Editors), Encyclopedia of Water Science. Marcel Dekker, New York, pp. 791- 794.

Wilczak, J.M., Oncley, S.P. and Stage, S.A., 2001. Sonic Anemometer Tilt Correction Algorithms. Boundary-Layer Meteorology, 99: 127-150.

Williams, D.G., Cable, W., Hultine, K., Hoedjes, J.C.B., Yepez, E.A., Simonneaux, V., Er-Raki, S., Boulet, G., de Bruin, H.A.R., Chehbouni, A., Hartogensis, O.K. and Timouk, F., 2004. Evapotranspiration components determined by stable isotope, sap flow and eddy covariance techniques. Agricultural and Forest Meteorology, 125(3-4): 241-258.

Wilson, J.D. and Sawford, B.L., 1996. Review of Lagrangian stochastic models for trajectories in the turbulent atmosphere. Boundary-Layer Meteorology, 78(1): 191-210.

Wilson, K., Goldstein, A., Falge, E., Aubinet, M., Baldocchi, D., Berbigier, P., Bernhofer, C., Ceulemans, R., Dolman, H., Field, C., Grelle, A., Ibrom, A., Law, B.E., Kowalski, A., Meyers, T., Moncrieff, J., Monson, R., Oechel, W., Tenhunen, J., Valentini, R. and Verma, S., 2002. Energy balance closure at FLUXNET sites. Agricultural and Forest Meteorology, 113(1-4): 223-243.

Wullschleger, S.D., Meinzer, F.C. and Vertessy, R.A., 1998. A review of whole-plant water use studies in tree. Tree Physiol, 18(8-9): 499-512.

APPENDICES

APPENDIX 1: **THE MSC THESIS IN PICTURES.**
APPENDIX 2: **EDDY COVARIANCE DATA QUALITY SCHEME**
APPENDIX 3: **BIOMETRIC DATA.**

APPENDIX 1: THE MSC THESIS IN PICTURES.

Q. ilex

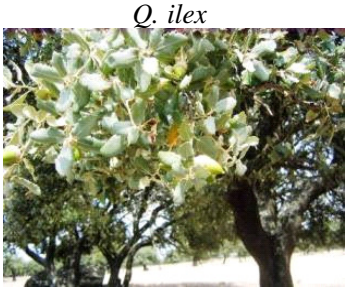

Q. pyrenaica

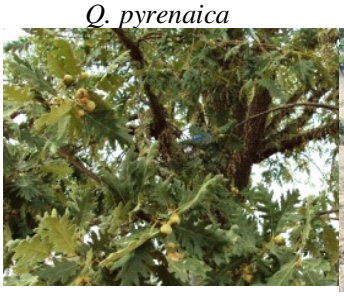

B.A xylem coring

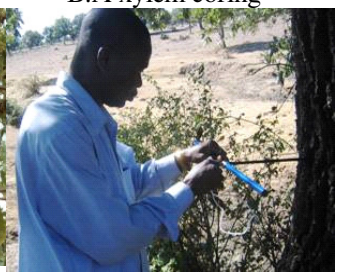

'Healing ' the tree

'raw' xylem core

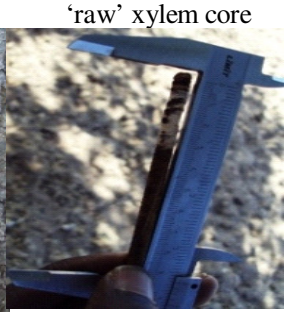

Methyl-'oranged' core

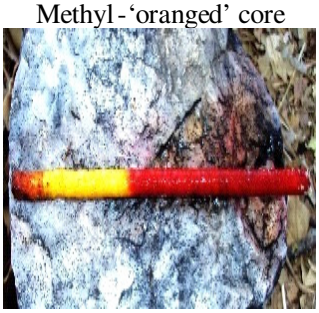

DTR drilling for TDP

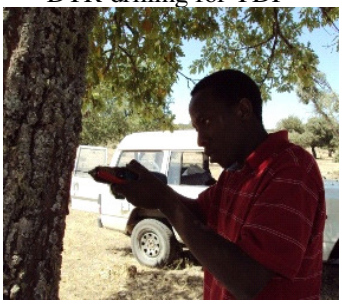

10 cm apart for TDP

LR silicon greasing for TDP

Complete TDP

DT & CVT installing

Eddy Tower Instruments

BA = Benjamin Agbakpe, LR = Leonardo Reyes (Advisor), CVT = Dr Christiaan van der Tol (1st Supervisor) and DTR = – myself – Donald Tendayi Rwasoka

APPENDIX 2: EDDY COVARIANCE DATA QUALITY SCHEME

The eddy covariance data quality assessment scheme after Foken et al. (2004) is based on the definitions tabulated below.

Stationarity Class	Stationarity - % Deviation	Integral Turbulence Characteristics Class	Integral Turbulence Characteristics - % Deviation
1	0-15	1	0-15
2	16-30	2	16-30
3	31-50	3	31-50
4	51-75	4	51-75
5	76-100	5	76-100
6	101-250	6	101-250
7	251-500	7	251-500
8	501-1000	8	501-1000
9	> 1000	9	> 1000

Overall Class	Stationarity Class	Integral Turbulence Characteristics Class
1	1	1-2
2	2	1-2
3	1-2	3-4
4	3-4	1-2
5	1-4	3-5
6	5	<5
7	≤ 6	≤ 6
8	≤ 8	≤ 8
9	9	9

APPENDIX 3: BIOMETRIC DATA.

Tree ID	X	Y	DBH (m)	A_l (m)	H1B (m)	Ax (m^2)	Ac (m^2)
B&D1p	739396.17	4555957.567	1.050	0.033	2.100	0.104	141.026
B&D2p	739397.509	4555988.119	0.929	0.035	2.100	0.095	84.949
B&D3p	739409.372	4556002.91	0.751	0.039	2.050	0.084	93.313
B&D4p	739435.526	4556066.748	1.019	0.046	1.800	0.137	191.134
B&D6p	739219.228	4555710.959	0.309	0.024	1.800	0.019	34.212
B&D7p	739432.02	4556011.321	0.223	0.031	1.800	0.016	21.237
B&D8p	739457.245	4555989.685	0.764	0.035	2.000	0.078	118.823
B&D9p	739505.955	4556031.028	0.201	0.023	1.900	0.011	18.857
B&D10p	739484.471	4555940.016	0.232	0.034	1.600	0.018	24.630
B&D11p	739580.000	4556043.000	0.234	0.021	2.500	0.012	23.758
B&D12p	739708.000	4556080.000	0.232	0.033	1.880	0.017	34.472
B&D13p	739741.000	4556035.000	0.662	0.031	2.600	0.058	70.138
B&D14p	739703.000	4556004.000	0.237	0.041	2.400	0.021	35.257
B&D15p	739396.000	4555800.000	0.325	0.045	2.400	0.035	37.176
B&D17p	739690.000	4556076.000	0.212	0.035	1.930	0.016	40.602
B&D18p	739702.000	4555929.000	0.621	0.036	2.400	0.063	102.608
B&D19p	739696.000	4555898.000	0.180	0.044	1.870	0.015	25.518
B&D20p	739692.000	4555952.000	0.660	0.035	2.200	0.066	106.596
B&D21p	739542.000	4555880.000	0.342	0.034	2.150	0.029	49.639
B&D1i	740224.298	4555773.289	0.796	0.042	2.000	0.097	103.869
B&D2i	740253.061	4555900.893	0.732	0.037	2.000	0.077	81.713
B&D3i	740263.771	4555798.438	0.159	0.058	1.400	0.015	23.758
B&D4i	740303.936	4555742.886	0.777	0.044	1.800	0.099	122.718
B&D5i	740328.151	4555724.559	0.668	0.033	2.100	0.063	59.447
B&D6i	740230.289	4555857.230	0.264	0.066	1.100	0.037	29.225
B&D7i	740244.354	4555880.877	0.350	0.060	1.800	0.051	50.265
B&D8i	740255.070	4555889.107	0.318	0.055	1.750	0.042	58.088
B&D9i	740255.742	4555881.011	0.350	0.048	1.600	0.043	47.784
B&D11i	740028.853	4555943.982	0.366	0.052	1.500	0.048	38.485
B&D12i	740029.369	4555955.178	0.283	0.033	1.650	0.024	24.630
B&D13i	740006.847	4555945.293	0.290	0.043	1.750	0.030	32.170
B&D14i	739981.454	4555920.694	0.293	0.039	1.600	0.029	33.183
B&D15i	739973.940	4555918.975	0.302	0.041	2.100	0.031	35.257
B&D64i	739667.000	4556022.000	0.312	0.060	1.900	0.044	50.265
B&D73i	739679.000	4556037.000	0.321	0.044	1.880	0.035	44.179
B&D92i	739742.000	4556032.000	0.220	0.062	1.720	0.027	20.308
B&D93i	739764.000	4556052.000	0.462	0.054	1.960	0.065	73.290
B&D107i	739687.000	4555991.000	0.716	0.063	2.100	0.125	124.690
B&D115i	739800.000	4556013.000	0.280	0.062	1.670	0.038	32.422
B&D116i	739789.000	4556027.000	0.754	0.042	2.000	0.092	81.713
B&D189i	739384.800	4555831.400	0.472	0.057	1.940	0.071	70.138